Soviet Physics

CRYSTALLOGRAPHY

Vol. 1, No. 4, pp. 299-387

July-August, 1956

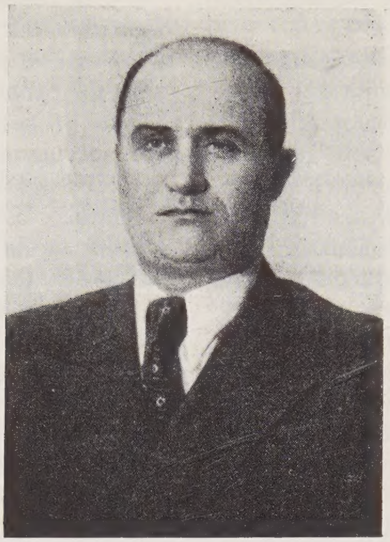

GERMAN STEPANOVICH ZHDANOV
(On His Fiftieth Birthday)

G. S. Zhdanov was born in Leningrad in 1906 into the family of a journalist. In 1930 he finished at Moscow University, having specialized in x-ray studies.

The first period of Zhdanov's scientific work was connected with a study of the statistical anisotropy of polycrystalline metals and alloys. He developed a method of studying textures with the aid of pole figures, and in 1929 set up a texture goniometer which enabled a single Debye line to be separated out from the x-ray diffraction picture of a polycrystalline specimen and to be developed into a pole figure. In the Tsgintsvetmet Laboratory, Zhdanov used this apparatus to study rolling texture and recrystallization in aluminum, copper, and a number of their alloys. For convenience in studying the unusual x-ray photographs obtained in the texture goniometer, he developed a special net enabling the x-ray picture to be transformed into the ordinary stereographic projection. In the monograph "Study of crystal orientations in metals and alloys by means of pole figures" (1934), Zhdanov gave a detailed review of the characteristics and experimental precision of the method of pole figures and its application. The principle of a texture goniometer analogous to that of Zhdanov was independently proposed at the same time by Kratky in Austria and in 1948 the same apparatus was constructed by Wooster in England.

As well as studying deformation texture, Zhdanov made x-ray diffraction studies of working recrystallization and selective recrystallization in metals and alloys, which demanded the development of a method of determining the number and size of crystallites with sizes from a few microns to a tenth of a millimeter. This method, developed together with V.I. Iveronova, was based on counting the number of interference points on the Debye line. This number, equal (to a first approximation) to the number of crystallites per unit volume, is proportional to the cube of the mean linear dimension of the crystallites; thus, a change in the crystallite dimensions of ten times should produce a change in the number of points on the Debye ring by a thousand times. This method has found wide application in Soviet and foreign investigations.

From 1938 began a new period in the scientific activities of G.S. Zhdanov; this was associated with his work in the L. Ya. Karpov Physicochemical Institute and was devoted to the atomic structure of

crystals. The work embraced various types of compound: inorganic (carbides, cyanides, rhodanides, borides, oxides), organic (nitrogen and halide derivatives of naphthalene and benzene, organic dyes), metallo-organic, intermetallic, etc.

The work of Zhdanov and his colleagues on the structure of crystalline substances was, in the majority of cases, completed by an exact determination of the positions of atoms and the establishment of the atomic structure of compounds which were sometimes completely new and synthesized for the first time (ozonides and superoxides of alkali metals). They also solved such complex structures as that of boron carbide, a large number of different rhodanides, cyanides, metallo-organic compounds such as tetra-aryl and tetraphenyl compounds of silicon, tin, lead, etc., and discovered the superperiodicity and polytypy in the structures of silicon carbide and potassium ferrocyanide. In a number of cases the structural investigations resulted in the refinement or modification of proposed chemical formulas and the detailed structure of individual structural elements.

German Stepanovich employed structural and crystal-chemical methods to elucidate the structure of individual radicals and atomic configurations associated with the directional properties of the bonds. He made a detailed study of the directional characteristics and multiplicity of bonds and their dependence on various states of the atoms. A leading place in Zhdanov's work is taken by analysis of the intermolecular interaction of atoms based on the theory of the chemical structure of molecules. The concept of the intermolecular radii of atoms of nonspherical form developed by Zhdanov and other Soviet scientists introduced a correction to the data of x-ray analysis in the part based on the analysis of intermolecular distances. Systematic studies of compounds containing polyatomic groups led to the establishment of laws significant in the crystal chemistry of both simple and complex inorganic compounds. The structural studies of Zhdanov are usually associated with departments of chemical institutes (IREA, NIUIF, GIAP, etc.), and with the demands of the chemical industry.

The requirements of practical applications (namely, the metallurgy of titanium-containing ores) also led to his work on the synthetic mineral anosovite and certain other titanium compounds, resulting in the assignment of the formula Ti_3O_5 to anosovite and confirmation of the existence of this intermediate oxide, the search for which had lasted a hundred years. Complete solution of the structure of anosovite showed that its peculiarity lay in the variable valence of titanium. The existence of an isomorphic group of oxides with the structure of anosovite was also established.

In recent years, Zhdanov has given great attention to the study of the structure of substances with special physical characteristics, in connection with the problem of synthesizing materials with assigned properties. Studies on the structure of ferroelectrics and piezoelectrics have been carried on in close association with the Institute of Silicate Chemistry of the Academy of Sciences of the USSR, and institutes and laboratories of the Ministry of the Radiotechnical Industry, and work on the structure of superconductors with the Institute of Physical Problems.

In recent years, the existence of superconducting alloys obtained from nonsuperconducting elements has been revealed. A particularly large number of such compounds has been found in alloys of bismuth. Zhdanov and a number of colleagues (Moscow Engineering-Physical Institute, Physics Faculty of Moscow State University), in contact with the Institute of Physical Problems, investigated the phase diagrams, phase composition, and structures of compounds of bismuth with nickel, rhodium, palladium, etc. The crystal chemistry of compounds of the transitional metals with elements of the B subgroup was considered, the laws of isomorphism and morphotropy in this group of compounds elucidated, and a diagram constructed to illustrate the crystal-chemical laws of morphotropy, polymorphism, and homology as functions of thermodynamic parameters (concentration, temperature, etc.). X-ray data have explained a number of questions important in superconductivity: the separation of superconducting and nonsuperconducting compounds, possible reasons for shifts in the temperature of the transformation into the superconducting state in compounds of variable composition, etc.

Zhdanov has carried out a number of investigations of the methods used in structural studies. He introduced the concept of the F^2 field and x-ray group, and (together with V.A. Pospelov) set up rational tables for determining such groups; these have been widely used.

The study of silicon–carbide modifications showed that they were all constructed on the close-packed law and consisted of stacks containing two or three layers of tetrahedra. For the description of this kind of structure, Zhdanov introduced the concept of a numerical symbol which made it easy to solve the structure of a number of forms of SiC and show that they all developed as a result of the superposition of a regular growth fault on the main perio-

dicity, this consisting of the missing or adding of an extra layer of tetrahedra. The existence of new types of silicon carbide was also prediced. The numerical symbol was accepted by many workers and entered into Soviet and foreign x-ray literature.

In 1947, Zhdanov received the Bach prize for the best work in physical chemistry. In 1952, he received the Mendeleev prize for work on the crystal chemistry of metal rhodanides.

Zhdanov's scientific work continually goes hand in hand with teaching, which began in 1930, when, with his participation, Moscow State University acquired a Faculty of X-Ray Structural Analysis headed by S. T. Konobeevskii. Zhdanov read lectures on a general course of physics in the Military Academy and the Physics Faculty of Moscow State University, on x-ray diffraction, metal physics, and solid-state physics in Moscow Engineering-Physical Institute, where he set up a Faculty of Metal Physics, and in the Physics Faculty of Moscow State University, where at the present time he occupies the Chair of Solid-State Physics.

Zhdanov has written a university course on The Fundamentals of X-Ray Structural Analysis (1940), and the two-volume X-Ray Diffraction of Metals, created together with Ya. S. Umanskii for metallurgical high schools; this has had two editions (1937 and 1941). These courses formed handbooks for students, graduates, engineers, and scientific workers in the field of x-ray analysis, and have not lost their value to the present day. Zhdanov taught a large number of x-ray diffraction workers, students, graduates, and those from the scientific-technical sphere working at the universities and scientific-research institutes of many cities in our country.

G.S. Zhdanov has taken part in all the All-Union Congresses on the use of x rays in the USSR. At the present time, he is the President of the X-Ray Commission of the Academy of Sciences of the USSR, which is occupied with coordinating work on x-ray diffraction being carried on in the Soviet Union.

ATOMIC AND IONIC DIMENSIONS OF THE TRANSURANIUM ELEMENTS IN CRYSTALS

A. F. Kapustinskii

Kurnakov Institute of General and Inorganic Chemistry

Translated from Kristallografiya, Vol. 1, No. 4,
pp. 382-392, July-August, 1956
Original article submitted May 12, 1956

The product of ionic volume and charge is shown to be constant, and this is used to deduce the ionic radii of the transuranium elements in various oxidation states. It is shown that the metallic and covalent radii for these elements can be deduced similarly.

Introduction

Zachariasen [1] has considered the chemical crystallography of the transuranium elements; data have also been published [2] on the sizes of the atoms in various oxidation states for protoactinium, uranium, neptunium, plutonium, and americium. No lattice-parameter measurements on other actinides (5 *f* elements) are known, and a theoretical means of deducing them is thus desirable.

An ideal ion [3] is a particle with electron shells of inert-gas type subject to a simple "equation of state" analogous to the isotherm for an ideal gas [4]; this can be used as the basis for such estimates. This equation has been verified mainly on isoelectronic series, but there are many different states of oxidation in the transuranium elements, which also have very large numbers of electrons, so these elements individually form a good test. A verification for ions not of the inert-gas type would enable one to use the equation for approximate evaluation of radii in the ionic, metallic, and covalent states, and for various degrees of oxidation.

Here we have to make some major restrictions and reservations. Ionic radii may be ascribed only to compounds dominated by heteropolar bonds and having strictly defined coordination numbers, but even in these cases the deviations from additivity are such that the errors cannot be less than ± 0.03 Å. In particular, an ion of charge +4 and above "pseudo-ions" cannot properly be treated as an effective sphere with a charge equal to the valence. We have discussed these features in some detail previously [4], but they must be stressed here because they are of considerable importance, especially in view of recent progress in theoretical chemistry.

In spite of this, there have recently been several formal treatments of radii, including those of ions with high charges, and the results have been quoted with limits of error quite incompatible with the observed deviations from additivity. Van Arkel [5], followed by Moeller [6] and Bokii and Belov [7] have used sizes for cations of charges +1 to +7, while Ormot [8] has calculated ionic radii for +4 and above, including +6. Moeller and Kramers give radii to a few thousandths of an angstrom [6], while Templeton and Dauben [9] give systems of radii for Me^{3+} to 0.001 Å in the rare-earth elements on the basis of 1.380 Å for the ionic radius of oxygen. The latter do point out that even the second decimal place is somewhat doubtful, but claim that the third is of value in comparisons; they consider the main application of radii to lie in the correlation of thermodynamic parameters. It would seem that all this is justified by the fact that such estimates are of great practical value, although the quantities have no proper physical significance. Good examples of the applications are provided by the work of Zachariasen [1] and Seaborg [2], in which the chemical crystallography of the transuranium elements has been explored.

This also forms the basis for the present extension of these calculations to the atoms and ions of the elements from americium to mendelevium, inclusive; but great care must be taken with respect to the accuracy and applicability in particular instances.

Cation Radii for the 5*f* Elements

(a) Relation of Ionic Volume to Charge. The ionic volume v is inversely proportional to the ionic charge η for eight-electron cations of inert-gas type. We have a simple relation analogous to Boyle's law

$$v \times \eta = \text{const} \qquad (1)$$

which agrees satisfactorily with the known experimental evidence. The constant in (1) may be found empirically or from

$$\text{const} = \frac{4}{3}\pi(\lg m)^3, \qquad (2)$$

in which m is the total number of electrons in the cation.

This has previously been verified for isoelectronic particles; here we apply (1) to the ions of each actinide element separately and examine the relation of volume to charge.

The following are some possible criticisms of the calculations given below:

1. Equation (1) is of simple form and cannot be supposed to give exact results even for the ideal ions for which it was proposed; it is even less exact for the transuranium cations, because only a few of these (e.g., Ac^{3+}) are of the inert-gas type, while most of them (e.g., Am^{3+}, Cm^{3+}) are particles of irregular configuration (Forster and Moeller [6]). We cannot foresee how far deviations from ideal structure will affect the calculation of particle size.

2. Equations (1) and (2) imply that this relation of volume to charge should apply if the number of electrons is constant, i.e., for isoelectronic systems; but the different ions of a single element are not isoelectronic. This feature is clearly important for elements at the beginning or middle of the periodic table, but it is of no practical significance for those at the upper end (transuranium elements), because any change in the number of valence electrons is small relative to the total number. The following example illustrates this. The variation in the number of electrons around the mean value has very little effect on $v\eta$ for americium, because (2) shows that this product is proportional to the logarithm of that number, not to the number itself. The variation in the number associated with the states of oxidation is

$$Am^{2+} \leftarrow Am^{4+} \rightarrow Am^{6+}$$
$$93 \leftarrow 91 \rightarrow 89$$

i.e., ±2; Eq. (2) gives us the possible variation in the constant as

$$\text{const} = 31.5 \pm 0.5, \text{ i.e.,} \quad \pm 1.5\%.$$

But (see below) we cannot expect an error less than about 4% from this relation, so the deviations from isoelectronic configuration have no effect for the transuranium elements.

The calculations are thus of some interest, but they are still based on (2), which is correct only for 8-electron cations; any final judgment must thus be based on empirical evidence.

The above discussion suffices to show that experiment alone can give a final answer on the possible practical use of (1) for the transuranium cations; similarly, only experiment can decide whether Boyle's law applies to a real gas in a particular pressure range.

The experimental evidence is derived from x-ray examination of the fluorides of the elements from protoactinium to americium (Zachariasen). His scheme for the ionic radii differs from Goldschmidt's system [10], which we have used in pre-

TABLE 1. Product of Charge and Volume for the Cations of Some Transuranium Elements

Element	Protoactinium					Uranium					Neptunium				
Valence (η)	2	3	4	5	6	2	3	4	5	6	2	3	4	5	6
Volume (v)	(7.44)	4.85	3.71	3.05	–	(6.92)	4.58	3.37	2.76	2.40	(6.76)	4.31	3.26	2.85	2.31
Product ($v\eta$)	(14.88)	14.55	14.84	15.25	–	(13.85)	13.74	13.48	13.80	14.40	(13.52)	12.93	13.04	14.25	13.86
Mean ($v\eta$)	14.88 ± 3%					13.85 ± 4%					13.52 ± 5%				

Element	Plutonium					Americium				
Valence (η)	2	3	4	5	6	2	3	4	5	6
Volume (v)	(6.49)	4.19	3.05	2.76	2.22	(6.27)	4.06	2.95	2.66	2.14
Product ($v\eta$)	(12.97)	12.57	12.20	13.80	13.32	(12.54)	12.18	11.80	13.30	12.84
Mean ($v\eta$)	12.97 ± 6%					12.53 ± 6%				

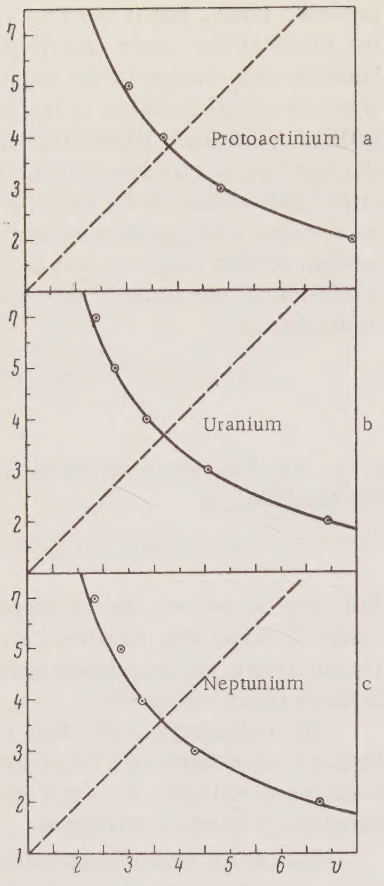

Fig. 1

vious papers [3,4], and which has a constant increment. The conversion is a simple matter, but we have not carried it through, because it is of no great importance and because our interest is in the extrapolation of Zachariasen's evidence, which appears adequate for the purposes of comparisons.

Table 1 gives the ionic volumes calculated from the usual formula

$$v = \frac{4}{3}\pi r^3 \qquad (3)$$

with Zachariasen's [1] ionic radii, together with the product of this by the charge and the mean of this product. The means have been used to deduce the closest extrapolated values for the volumes of doubly charged ions, and hence the radii of these (quantities in parentheses).

Figure 1, parts a-e, shows that all points fit satisfactorily on rectangular hyperbolas, whose diameters are represented by the broken lines. The data of Table 1 show that there is no systematic trend in the deviations from the mean of $v\eta$ within each hyperbola, and the largest deviations (±6%) do not exceed those found for ideal ions [4]. These ions thus obey the simple relation previously established.

(b) Calculation of Ionic Radii from Americium to Mendelevium. There is no reason to suppose that $v\eta$ = const ceases to apply above americium, so it could be used to find the ionic radii of these elements in their various states of oxidation if we had a reliable means of extrapolation for the radii (i.e., volume) for some one state. This is actually so, because the trivalent state has been examined in great detail, and here the ionic radii differ from those of the lanthanides by a constant amount, except for the first members, uranium and neodymium, the radius of the former being 1.03 Å and of the latter 0.99 Å, with difference 0.04 Å. The difference for all the others is exactly 0.03 Å (Fig. 2), and this increment[1] may be used

[1]Haissinsky [13] pointed out that the elements from curium onward are analogous to the rare-earth elements (gadolinium onward); this has been confirmed [14], and the elements have been called transcurium ones. This also confirms that it is correct to draw the line in Fig. 2.

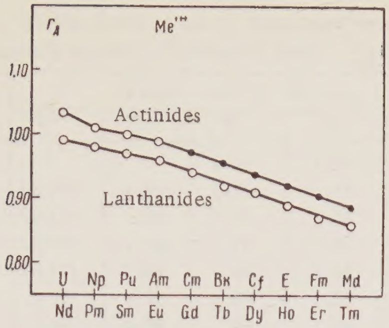

Fig. 2

TABLE 2. Ionic Radii of the 5*f* Elements in Their Various Valence States

Radius (A) for ions of charge	Element	Radius (A) for ions of charge 2+	3+	4+	5+	6+
91	Pa	(1.21)	(1.05)	0.96	0.90	–
92	U	(1.18)	1.03	0.93	0.89	0.83
93	Np	(1.17)	1.01	0.92	0.88	0.82
94	Pu	(1.16)	1.00	0.90	0.87	0.81
95	Am	(1.14)	0.99	0.89	0.86	0.80
96	Cm	1.11	0.97	0.88	0.82	0.77
97	Bk	1.09	0.95	0.86	0.80	0.75
98	Cf	1.08	0.94	0.85	0.79	0.74
99	E	1.05	0.92	0.84	0.78	0.73
100	Fm	1.03	0.90	0.82	0.76	0.72
101	Md	1.02	0.89	0.81	0.75	0.71

to find r for Me^{3+} for the elements from americium to mendelevium by reference to the precisely known radii of the lanthanides, in accordance with the concept of the "curides" (Haissinsky, 1953).

The calculation is, of course, based on the acceptance of the transuranium elements as actinides, which resemble the lanthanides. This might subsequently be found to be untrue, in which case this method of evaluating the ionic radii would become valueless.

From r (i.e., v) for the Me^{3+} we find the constant in (1), which may then be used to find r and v for all the other 5*f* elements (Table 2). The upper part of this table (and of the following ones) gives Zachariasen's results, except for the values in parentheses (for the +2 state), which are ours; the lower part gives our results.

Atomic Radii Corresponding to Metallic Bonds for the 5*f* Elements

(a) Constancy of $v\eta$ for the Metallic State. We have previously [4] considered the applicability of (1) to metals on the basis of data for temperatures near absolute zero, the number of free electrons being taken as equal to the maximal stable valence of the element. The number of electrons may vary with the conditions, so it is of interest to examine the constancy of $v\eta$ for a given element in the metallic state for various η, i.e., for various numbers of free electrons in the lattice. Zachariasen gives the relevant data (for uranium to americium) in [2]. Table 3 gives the volumes calculated from (2), the valences (or charges), and the product of these.

This product is seen to be constant for the elements from uranium to americium, and (most important) it is more closely constant than for ionic lattices, for the deviations from the mean do not exceed 4%. Parts a-d of Fig. 3 show that the points fit the hyperbolas closely, so (1) may be considered justified for the transuranium elements in the metallic state.

(b) Calculation of Atomic Radii from Americium to Mendelevium. These radii may be found by a method analogous to that used above for the ionic radii; the data (Table 4) show that the radius of the atom or ion decreases by 0.01 Å as Z increases by one unit in the 5*f* ele-

TABLE 3. Product of Charge and Volume for the Atoms of Some Transuranium Elements

Element	Uranium					Neptunium				
Valence (η)	(2)	3	4	5	6	(2)	3	4	5	6
Volume (v)	(44.55)	29.65	22.07	17.48	15.49	(43.015)	28.28	21.31	17.16	14.71
Product ($v\eta$)	(89.10)	88.94	88.27	87.40	91.78	(86.03)	84.84	85.25	85.79	88.27
Mean ($v\eta$)	89.10 ± 3%					86.03 ± 3%				

Element	Plutonium					Americium				
Valence (η)	(2)	3	4	5	6	(2)	3	4	5	6
Volume (v)	(41.73)	26.95	20.58	16.84	14.42	(40.82)	26.10	20.22	16.52	14.14
Product ($v\eta$)	(83.47)	80.86	82.32	84.20	86.52	(81.65)	78.29	80.88	82.61	84.82
Mean ($v\eta$)	83.47 ± 4%					81.65 ± 4%				

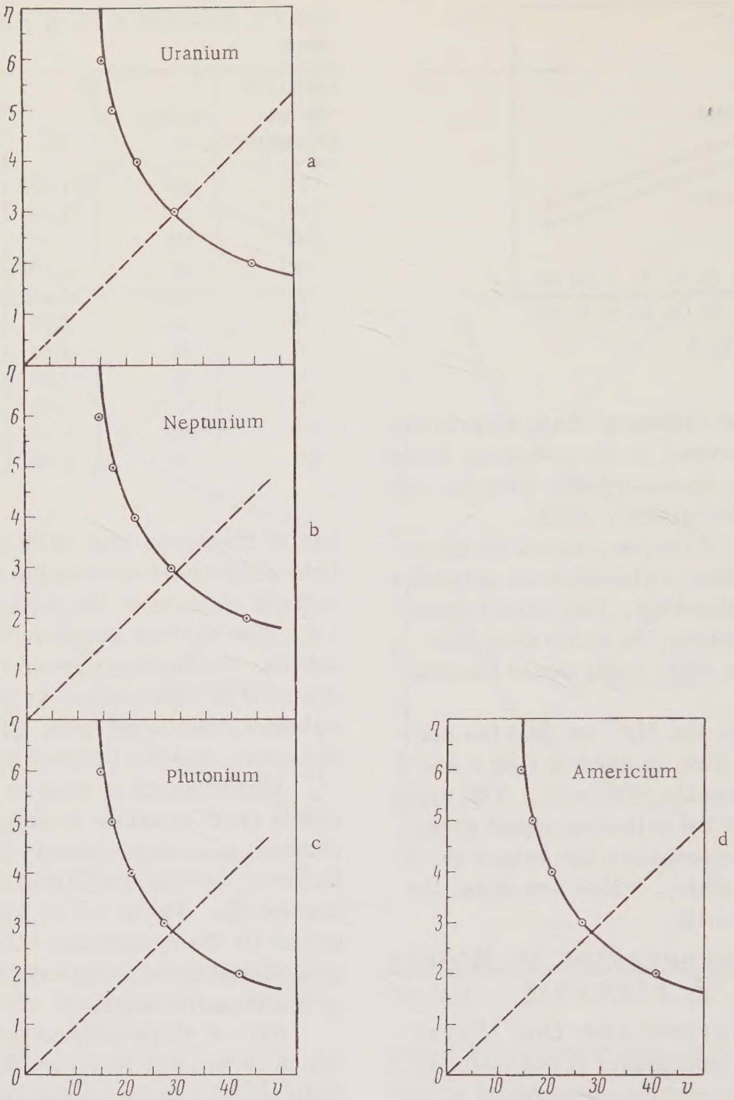

Fig. 3

ments, except for neptunium, where the reduction is 0.02 Å. We assume that this relation applies to the elements from curium to mendelevium, inclusive, which gives us the atomic radii for the trivalent transuranium elements for which data are lacking.

The volumes are found from (3), and from these the constant value of $v\eta$; this gives v, and hence r, for the various valence states, as for the ionic radii (Table 5).

Covalent Radii for the Transuranium 5*f* Elements

The covalent radii are less than the atomic radii by 0.11 Å (to 0.01 Å) for all known degrees of oxidation; this simple rule applies without exception

TABLE 4. Radii of Me^{3+} for theTransuranium Elements, Coordination Number 12, with Radii for the Metals from Uranium to Curium from Seaborg [2] and Ionic Radii for Table 2

Element	U	Np	Pu	Am	Cm	Bk	Cf	E	Fm	Md
$\Delta = r_{atom} - r_{ion}$	0.89	0.88	0.86	0.85	0.84	0.83	0.82	0.81	0.80	0.79
Radius of atom,A	1.92	1.89	1.86	1.84	1.81	1.78	1.76	1.73	1.70	1.68

TABLE 5. Atomic Radii of the 5*f* Elements Corresponding to Coordination Number 12 (Metallic Bond)

Element	Atomic radii (A) for state				
	2+	3+	4+	5+	6+
Pa	–	–	1.76	1.63	–
U	(2.20)	1.92	1.74	1.61	1.54
Np	(2.17)	1.89	1.72	1.60	1.52
Pu	(2.15)	1.86	1.70	1.59	1.51
Am	(2.12)	1.84	1.69	1.58	1.50
Cm	2.07	1.81	1.64	1.53	1.44
Bk	2.04	1.78	1.62	1.50	1.41
Cf	2.01	1.76	1.60	1.48	1.40
E	1.98	1.73	1.57	1.46	1.37
Fm	1.95	1.70	1.54	1.43	1.35
Md	1.92	1.68	1.53	1.42	1.33

TABLE 6. Covalent Radii for Single Bonds in the 5*f* Elements

Element	Covalent radius (A) for state		
	4+	5+	6+
Th	1.67	–	–
Pa	1.64	1.52	–
U	1.62	1.50	1.42
Np	1.60	1.49	1.41
Pu	1.58	1.48	1.40
Am	1.57	1.47	1.39
Cm	1.53	1.42	1.33
Bk	1.51	1.39	1.30
Cf	1.49	1.37	1.29
E	1.46	1.35	1.26
Fm	1.43	1.32	1.24
Md	1.42	1.31	1.22

to the transuranium elements, as Zachariasen's data show (Tables 5 and 6). The fixed increment of 0.11 Å gives the covalent radii listed in Table 6. Only the +4, +5, and +6 states have been considered, because there is no proof that the increment applicable to these remains the same for larger or smaller charges. An exception to this is our calculated point for U^{3+} in Fig. 4.

The data on the covalent radii are too limited to give an extensive test of (1); the known range in charge (+4 to +6) is narrow, but (1) is followed very closely in this range, as Fig. 4 shows for uranium.

The errors in these calculations are governed mainly by the basic assumption in the extraplation, namely, the degree to which the transuranium elements show the properties of actinides. Equation (1) is very convenient for evaluating r, because (2) shows that substantial variation in v leads to very little change in r. The maximum error of extrapolation arising from the use of (1) is such as to indicate limits of error of ±0.03 Å for the radii.

An interesting point is that (1), which states that the mean density of the electron gas in an atom or ion is proportional to the charge, is obeyed almost as closely as are the gas laws. For instance, the product vp for nitrogen varies by less than 1%

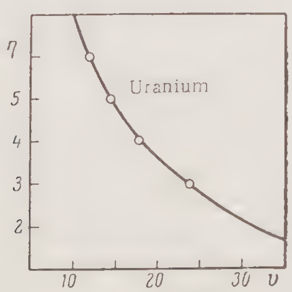

Fig. 4

between 1 and 40 atm at 15°C [11], while the variation for air is only 2%. Contrast the behavior of the osmotic pressure π, which for typical nonelectrolytes (e.g., glucose) in classical physical chemistry formed one of the principal tests of Van't Hoff's theory; the product $v\pi$ at 0°C may (Berkley and Hartley) vary by 15-20% [12]. The electron system in an atom or ion is extremely complex, and the concept of mean electron density is merely a convenient fiction, but here the ideal law $v\eta$ = const is followed to within 4-6%.

Conclusions

1. The simple law $v\eta$ = const (v = volume of atom or ion, η = charge or valence) is discussed in relation to the transuranium elements. It is found that Zachariasen's results confirm this law for ions, atoms in metals, and covalent bonds.

2. The law $v\eta$ = const is used to extrapolate the data given by Seaborg, to ionic, metallic, and covalent radii of other transuranium elements; radii have been calculated for curium, berkelium, californium, einsteinium, fermium, and mendelevium in various states of oxidation.

LITERATURE CITED

1. W. Zachariasen, "Crystal radii of the heavy elements," Phys. Rev., 73, 1104 (1948).
2. The Actinide Elements, edited by G. Seaborg and J. Katz (New York, 1954).
3. A.F. Kapustinskii, "Constancy and multiple proportions as basic laws in crystallography and chemistry," Kristallografiya, 1, 1, 90-94 (1956).
4. A.F. Kapustinskii, "Radii of eight-electron cations," Zh. Neorgan. Khim., 1, 82 (1956).

5. A. van Arkel, Molecules and Crystals (London, 1949).
6. T. Moeller, Inorganic Chemistry. An Advanced Textbook (New York, 1952).
7. G. B. Bokii, Introduction to Chemical Crystallography [in Russian] (1954), p. 120.
8. B. F. Ormont, Structures of Inorganic Substances [in Russian] (1950), p. 166.
9. D. Templeton and C. Dauben, "Lattice parameters of some rare-earth compounds," J. Am. Chem. Soc., 76, 5237 (1954).
10. V. Goldschmidt, Geochemische Verteilungsgesetze der Elemente. Oslo, 8, 69 (1926).
11. E. V. Biron, The Science of Gases and Liquids [in Russian] (1923), p. 30.
12. A. V. Rakovskii, Textbook of Physical Chemistry [in Russian] (1939), p. 261.
13. M. Haissinsky, "La place des elements transuraniens dans le systeme periodique," Experimentia IX/3, 117 (1953).
14. C. Bedreag, "Les uranides et les transcuriens," Compt. rend. Acad. Sci., 240, 18, 1767 (1955).

THEORY OF HYSTERESIS EFFECTS IN BARIUM TITANATE

L. P. Kholodenko

Marx Pedagogic Institute, Smolensk
Translated from Kristallografiya, Vol. 1, No. 4, pp. 393-402, July-August, 1956
Original article submitted February 18, 1956

The relation of polarization to field strength and temperature is considered for points above and below the transition temperature. An exploration is proposed for double hysteresis loops.

Hysteresis in barium titanate is of considerable importance but it has not been studied in detail. A fairly detailed study of hysteresis has been made for the case in which the transition to or from the ferroelectric[1] state may be considered as a second-order transition [1,2],[2] but some experiments indicate that the transition in $BaTiO_3$ is a first-order one. Some brief notes on hysteresis have been published [3] for this case; but the effects are then more varied, and they occur above and below the point of transition from phase I to phase II. The hysteresis curve takes a special shape above the transition temperature; double loops [4] are obtained.

Consider a temperature range embracing phases I and II, the electric field vector $\vec{E}$ being directed along the vector $\vec{P}$; then the expression [5] for the thermodynamic potential

$$\Phi = \Phi_0 + \alpha P^2 + \frac{1}{2}\beta_1 P^4 + \beta_2 (P_x^2 P_y^2 + P_y^2 P_z^2 + P_z^2 P_x^2) + \frac{1}{3}\gamma_1 P^6 + \gamma_2 [P_x^4 (P_y^2 + P_z^2) + P_y^4 (P_z^2 + P_x^2) + P_z^4 (P_x^2 + P_y^2)] + \gamma_3 P_x^2 P_y^2 P_z^2 - (\vec{P}\vec{E})$$

may be simplified by putting $P_x = P_y = 0$, $P_2 = P$, after which it becomes

$$\Phi = \Phi_0 + \alpha P^2 + \frac{1}{2}\beta_1 P^4 + \frac{1}{3}\gamma_1 P^6 - PE. \tag{1}$$

It is convenient to examine hysteresis by reference to the following two cases: (1) $\beta_1(T) > 0$, and (2) $\beta_1(T) < 0$, where T is the temperature at which the P(E) curve is recorded. Let T_{12} be the temperature of transition from phase I to phase II; then we have a second-order transition if $\beta_1 > 0$ for $T > T_{12}$ (if $E = 0$), because $d\beta_1/dT < 0$ [7], and the condition $\beta_1(T) > 0$ implies that also $\beta_1(T_{12}) > 0$. Conversely, the I-II transition is of first order if $\beta_1 < 0$ for $T < T_{12}$.

Case $\beta_1(T) > 0$

Here γ_1 is positive [5,6], so we may introduce the dimensionless polarization p,

$$P = \sqrt{\frac{\beta_1}{\gamma_1}}\, p, \tag{2}$$

and put (1) in the dimensionless form

$$\varphi = \frac{\Phi - \Phi_0}{\beta_1^3}\gamma_1^2 = \frac{\alpha\gamma_1}{\beta_1^2} p^2 + \frac{1}{2} p^4 + \frac{1}{3} p^6 - \frac{\gamma_1^{3/2}}{\beta_1^{5/2}} pE. \tag{3}$$

The dimensionless field e is defined by

$$\frac{\gamma_1^{3/2}}{\beta_1^{5/2}} E = 2e, \tag{4}$$

and we put

$$\frac{\alpha\gamma_1}{\beta_1^2} = \xi. \tag{5}$$

The final expression is

$$\varphi = \xi p^2 + \frac{1}{2} p^4 + \frac{1}{3} p^6 - 2pe. \tag{6}$$

The condition for a turning point in φ is

$$p^5 + p^3 + \xi p = e, \tag{7}$$

[1] The paraelectric and ferroelectric phases are denoted as phase I and phase II, respectively.

[2] This is necessary in order to allow us to stop the expansion of the potential in powers of P at terms of fourth degree.

and the type of turning point is governed by the sign of

$$\frac{\partial^2\varphi}{\partial p^2} = 2\xi + 6\,p^2 + 10\,p^4. \tag{8}$$

For $\xi > 0$, we have $\partial^2\varphi/\partial p^2 > 0$ for any e, so $\xi > 0$ gives the solution to (7) as corresponding to a minimum, which exists for all e. This, in the approximation to which fluctuations are neglected, means that hysteresis is impossible for $\xi > 0$; but (5) shows that $\xi > 0$, in conjunction with the positive sign of γ_1, is equivalent to $\alpha > 0$, so hysteresis is impossible for $T > T_{12}$.

It is best to put (8) in the following form for $\xi < 0$:

$$\frac{\partial^2\varphi}{\partial p^2} = 10\left(p^2 + \frac{3}{10} + \sqrt{\frac{9}{100} - \xi/5}\right) \times \left(p^2 + \frac{3}{10} - \sqrt{\frac{9}{100} - \xi/5}\right). \tag{9}$$

Then (9) shows that a minimum in φ corresponds to the p that satisfy

$$p^2 > \eta - \frac{3}{10}, \tag{10}$$

in which

$$\eta = \sqrt{\frac{9}{100} - \frac{\xi}{5}}. \tag{11}$$

The origin of the hysteresis has been elucidated [1,2]; φ(p) for the e = 0 is a symmetrical curve with two minima, but φ(p) for e > 0 has the right-hand minimum deeper than the left-hand one, which vanishes (together with the intervening maximum) at $e = |e_k|$, which corresponds to a $p = p_k$ given by

$$p_k = \sqrt{\eta - \frac{3}{10}} \tag{12}$$

at which point $\partial^2\varphi/\partial p^2$ is zero.

The condition for a minimum in φ may be put in a different form convenient for graphical examination.

We take e as a function of the extremal p instead of as a given quantity[3]; then from (7) we have

$$\frac{\partial^2\varphi}{\partial p^2} = 2\,\frac{\partial e(p)}{\partial p}. \tag{13}$$

Condition (10) is thus equivalent to

$$\frac{\partial e(p)}{\partial p} > 0, \tag{14}$$

while (12) is equivalent to $\partial e/\partial p = 0$ (or $\partial p/\partial e = \infty$).[4]

We solve (7) graphically to find p(e) for a given ξ; for this purpose we put (7) in the form

$$p^5 + p^3 = e - p\xi, \tag{15}$$

construct the curve $y = p^5 + p^3$, and locate the intersections with the straight lines $y = e - p\xi$ (Fig. 1). Large positive e (line 1) give only one value of p corresponding to minimum φ; e and p decrease together, because $\partial e/\partial p > 0$. At $e = |e_k|$ the line $e - p\xi$ meets the right branch of $p^5 + p^3$ and is tangential to the left branch (line AB). Lower e give three points of interesection (line 2), the middle one corresponding to a maximum in φ and the two end ones to a minimum. For $e = e_k < 0$ (line CD) the straight line touches the curve at the $p = p_k$ defined by (12), and $\partial p/\partial e$ becomes infinite. Further reduction in e gives only negative p, i.e., ones on the left-hand branch (line 3). The hysteresis curve has a width $2|e_k|$, and is defined by

$$e_k = \left(\eta - \frac{3}{10}\right)^{5/2} + \left(\eta - \frac{3}{10}\right)^{3/2} + \xi\left(\eta - \frac{3}{10}\right)^{1/2}. \tag{16}$$

Formula (16) also relates the width to the temperature; it may be simplified near the Curie point, where $|\xi| < 1$, and

$$\eta - \frac{3}{10} \approx -\frac{1}{3}\xi.$$

Taking only terms up to $\xi^{3/2}$, we have

$$e_k = -\frac{2}{3\sqrt{3}}\sqrt{-\xi^3}. \tag{17}$$

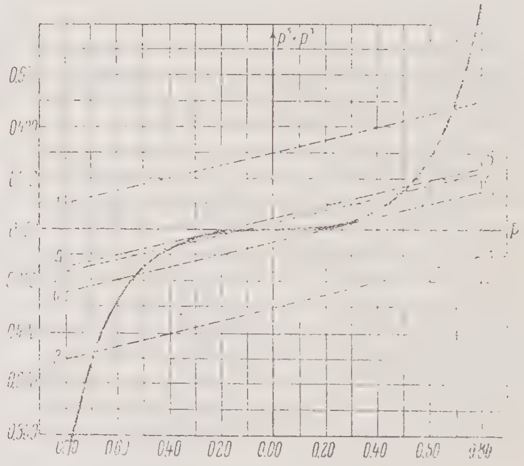

Fig. 1

[3]Each extremum has its own e(p) if there are several.

[4]The condition for the minimum to vanish has been used in this form in [2].

Finally, in terms of variables of direct physical significance[5]

$$E_k = -\frac{4}{3\sqrt{3}}\cdot\frac{1}{\sqrt{\beta_1}}\cdot\alpha^{\frac{3}{2}}(T_{12}-T)^{\frac{3}{2}}. \qquad (18)^5$$

Case $\beta_1(T) < 0$

Here p is defined by

$$P = \sqrt{-\frac{\beta_1}{\gamma_1}}\,p, \qquad (19)$$

and (1) is put as

$$\varphi = \frac{\Phi-\Phi_0}{-\beta_1^3}\gamma_1^2 = \frac{1}{3}p^6 - \frac{1}{2}p^4 + \xi p^2 - 2pe. \qquad (20)$$

Also, ξ has the same meaning as before, and

$$2e = \frac{\gamma_1^{3/2}}{(-\beta)_1^{5/2}}E. \qquad (21)$$

The turning points in φ(p) are now found from

$$p^5 - p^3 + p\xi = e, \qquad (22)$$

and the type of turning point is governed by the sign of

$$\frac{\partial^2\varphi}{\partial p^2} = 10p^4 - 6p^2 + 2\xi. \qquad (23)$$

For $\xi > 9/20$, we have $\partial^2\varphi/\partial p^2 > 0$, so hysteresis is impossible for $\xi > 9/20$.

For $\xi < 9/20$, we put (23) as

$$\frac{\partial^2\varphi}{\partial p^2} = 10\left(p^2 - \frac{3}{10} + \sqrt{\frac{9}{100} - \frac{1}{5}\cdot\xi}\right)\left(p^2 - \frac{3}{10} - \sqrt{\frac{9}{100} - \frac{1}{5}\xi}\right).$$

We again introduce η from (11) and put the condition for a minimum in φ as

$$\left(p^2 - \frac{3}{10} + \eta\right)\left(p^2 - \frac{3}{10} - \eta\right) > 0. \qquad (24)$$

Then (24) shows that φ has a minimum when

$$p^2 > \frac{3}{10} + \eta \text{ and } p^2 < \frac{3}{10} - \eta. \qquad (25)$$

Also, p^2 in the range $3/10 - \eta < p^2 < 3/10 + \eta$ corresponds to a maximum in φ; when

$$p = p_k = \pm\sqrt{\frac{3}{10} + \eta} \text{ and } p = p_k' = \pm\sqrt{\frac{3}{10} - \eta}, \qquad (26)$$

the minimum is lost (stability is lost).

We may solve (22) graphically, as for $\beta_1 > 0$, via the $y = p^5 - p^3$ curve of Fig. 2,[6] which intersects lines $y = e - p\xi$.

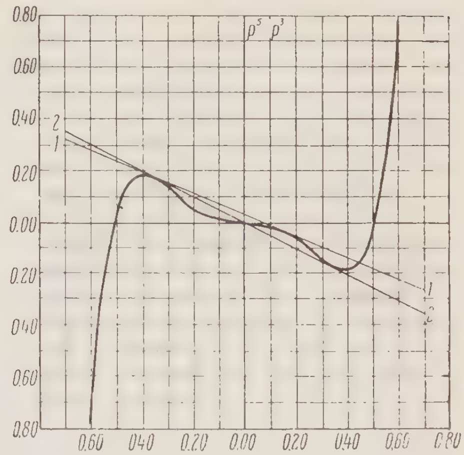

Fig. 2

Let $\xi < 0$; here the general form of p(e) is as for $\beta_1 > 0$. Let $0 < \xi < 9/20$; here we must distinguish the following ranges in ξ:

a) $0 < \xi < 0.2$, b) $0.2 < \xi < 0.25$, c) $0.25 < \xi < 0.45$.

This division is governed by the geometry of the accessory curve. Lines 1 and 2 in Fig. 2 are the common tangents to the left and right parts of the curve, their slopes being −0.2 and −0.25. The division has also another significance, because regions (a) and (b) together constitute the temperature range in which the crystal may exist as phase I or phase II in the absence of a field. In fact, we have that $0 < \xi < 0.25$ is, from (5), equivalent to $0 < \alpha < \beta_1^2/4\gamma_1$, which defines the region of temperature hysteresis in the I-II transition [7].

Let ξ correspond to range (a), and let e be large; then $e - p\xi$ (Fig. 3) meets the accessory curve once only (position 1). Reduction in e causes the line to touch the curve once (at C, position 2), then to intersect it at three points (position 3), and finally at five points (position 4). The condition $\partial p/\partial e > 0$, with Fig. 3, shows that the points of intersection corresponding to maxima and minima in φ occur alternately, intersection with branch FB always corresponding to a minimum. The loss of stability in this solution and the jump to branch CG occur at point B, where $e = e_k < 0$. The jump in the reverse sense (to curve BF) occurs at point C, where $e = -e_k$, when e is changed in the opposite sense. The p(e) curve takes the form of the usual loop, whose width is $2|e_k|$. Figure 4 shows this for the particular case $\xi = 0.15$.

[5] Formula (18) was first derived in [1].

[6] This is called the accessory curve.

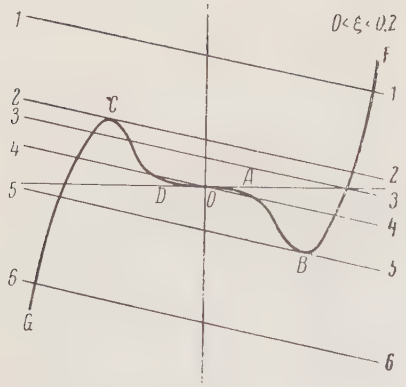

Fig. 3

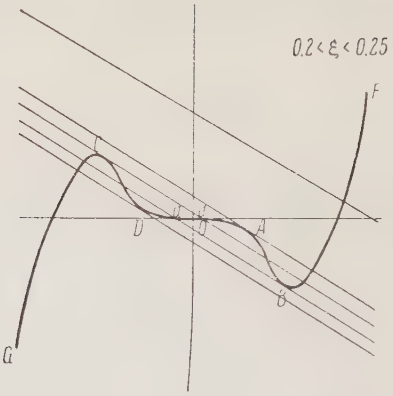

Fig. 5

Consider again ξ corresponding to range (a), with $e = 0$, the crystal not having been exposed to an electric field; the stable equilibrium position corresponds to $p = 0$, i.e., to the intersection of $e - p\xi$ with branch AD at the origin. As e increases, so will p, until the line $e - p\xi$ touches the curve at A. At this point the solution corresponding to p small becomes unstable,[7] there being a jump to branch BF.[8] However, e in the range $-|e_k'| < e < |e_k'|$, (in which e_k and $-e_k$ correspond to lines through D and A) will allow only the first of the solutions; curve aOd of Fig. 4 represents this p(e) curve. The existence of solution I distinguishes range (a) from the range $\xi < 0$.

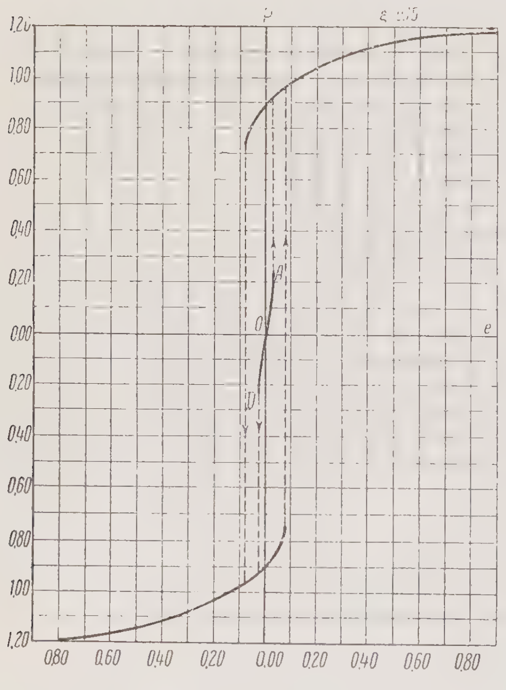

Fig. 4

The width $2|e_k|$ of the hysteresis curve may be found, as may $2|e_k'|$, the width of the range in e corresponding to solution I. We have from (22) and (25) that the first is given by

$$e_k = \left(\frac{3}{10} + \eta\right)^{5/2} - \left(\frac{3}{10} + \eta\right)^{3/2} + \xi\left(\frac{3}{10} + \eta\right)^{1/2}, \quad (27)$$

which for $\xi \ll 1$ may be simplified to

$$e_k = -\sqrt{\frac{3}{5}} \cdot \left(\frac{6}{25} - \xi\right). \quad (28)$$

The second is also[9] given by (22) and (25) as

$$e_k' = -\left(\frac{3}{10} - \eta\right)^{5/2} + \left(\frac{3}{10} - \eta\right)^{3/2} - \xi\left(\frac{3}{10} - \eta\right)^{1/2}, \quad (29)$$

and for $\xi \ll 1$ may be put, up to terms in $\xi^{3/2}$, as

$$e_k' = -\frac{2}{3\sqrt{3}}\xi^{3/2}. \quad (30)$$

In terms of variables of direct physical significance Eqs. (28) and (30) are

$$E_k = -2\sqrt{\frac{3}{5}} \cdot \frac{(-\beta_1)^{5/2}}{(\gamma_1)^{3/2}} \cdot \left(\frac{6}{25} - \frac{\alpha\gamma_1}{\beta_1^2}\right), \quad (31)$$

$$E_k' = -\frac{4}{3\sqrt{3}} \cdot \frac{\alpha^{3/2}}{(-\beta_1)^{1/2}} \approx -\frac{4}{3\sqrt{3}} \cdot \frac{\dot{\alpha}^{3/2}}{(-\beta_1)^{1/2}}(T - T_{12})^{3/2}. \quad (32)$$

The region of e allowing solution I vanishes for $T \to T_{12}$.

Now let ξ correspond to range (b); Fig. 5 illustrates the relation of the curve to the $y = e - p\xi$ lines. The results are as follows. The polariza-

---

[7] This is the solution appropriate to phase I, hence solution I.

[8] Solutions corresponding to branches BF and CG may be called solution II, by analogy.

[9] Figure 4 shows that the minus sign must be taken in (26).

tion is defined by $e - p\xi$ at its intersection with branch BF for a crystal initially in a strong field (with $e > 0$) that then decreases; at B ($e = e_k$) we get a jump to the p defined by branch AOD, and then a second jump (at $e = e_k'$, point D) to the polarization corresponding to branch CG. Variation of e in the reverse sense leads to jumps in the polarization at C and A.

Range (b) thus resembles range (a) in having a region of solution I, which corresponds to the $e - p\xi$ line meeting branch AOD of the accessory curve.

Figure 6 shows the p(e) corresponding to range (b) for the case $\xi = 0.22$; (27) and (29), for e_k and e_k', simplify also for ξ close to 0.25, so we put $\xi = 0.25 - \varepsilon$, with $0 < \varepsilon \ll 1$, to get

$$e_k \approx -\frac{\varepsilon}{\sqrt{2}}, \quad e_k' \approx -\frac{1}{\sqrt{10}}(0.16 - \varepsilon). \tag{33}$$

ξ close to 0.25 indicate T close to T_{21} (compare the previous case). We use (4) and (5) to convert (33) to E and T, with $\alpha(T) = \alpha(T_{21}) + \dot{\alpha}(T - T_{21})$, to get

$$E_k \approx \sqrt{-\frac{2\beta_1}{\gamma_1}\cdot\dot{\alpha}(T - T_{21})},$$

$$E_k' \approx -\frac{2}{\sqrt{10}}\left[0.16 + \sqrt{-\frac{\beta_1}{\gamma_1}\cdot\dot{\alpha}(T - T_{21})}\right].$$

Figure 7 indicates the possible states for range (c); for e decreasing from large positive values down to $e = |e_k|$,[11] we get p on branch FB, while further change in p down to point D occurs along

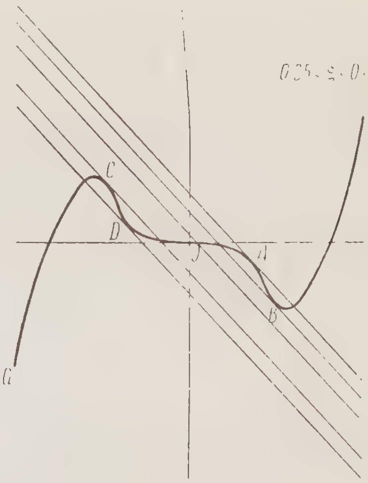

Fig. 7

branch BOD. At D ($e = e_k$) there is a jump to branch CG, p remaining on this branch as e decreases further. For e changing in the reverse sense, we get a jump from branch CG to DOA at C, and another from DOA to BF at A. The region of solution I corresponds to branch DOA, and Fig. 8 shows p(e) for this case ($\xi = 0.30$), which is of "double-loop" type [4].

The following explanation has been proposed [4] for this double loop: the temperature for the transition from phase I to phase II (and from II to I) is that at which the two phases have the same thermody-

[10] Here and subsequently we neglect the dependence of β_1 on T.

[11] $e = |e_k|$ corresponds to the tangent at B.

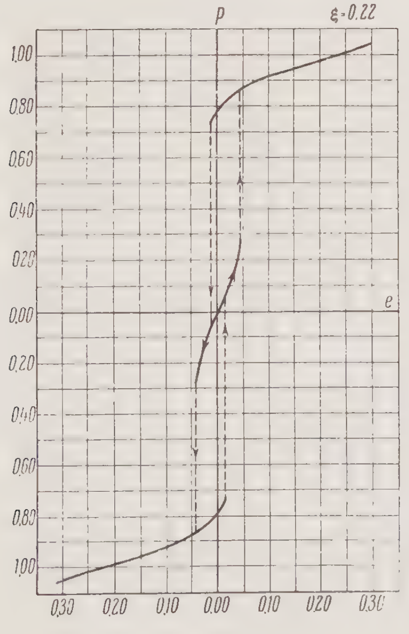

Fig. 6

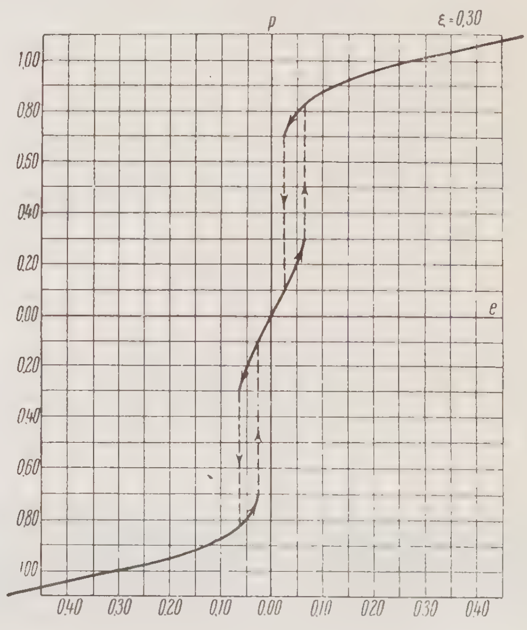

Fig. 8

namic potential. A field E displaces the transition point, positive E displacing it toward higher temperatures and negative E toward lower ones.[12] A crystal near to, but above the transition temperature thus acquires a certain spontaneous polarization above an E, governed by the distance from the transition point, but this is lost as the field is reduced. The crystal becomes polarized twice per cycle in an alternating field. No allowance was made for metastable states in [4], but these states are considered here, in that the transition from one possible state A to another possible state B occurs only when state A loses its stability (passes from a metastable condition to an unstable one). This is equivalent to neglect of fluctuations, a matter that has been examined in [7]. It can be shown that fluctuations are of no great importance in the theory of hysteresis. Secondary effects are probably responsible for the absence of the theoretically predicted discontinuities on the experimental hysteresis curves.

LITERATURE CITED

1. V. L. Ginzburg, "Polarization and piezoelectric response in barium titanate near the ferroelectric transition point," Zh. Éxperim. i Teor. Fiz., 19, 36-41 (1949).
2. G. A. Smolenskii and V. Kh. Kozlovskii, "Temperature dependence of the dielectric constant of a crystal, with allowance of anharmonicity in the ion vibrations," Zh. Éxperim. i Teor. Fiz., 23, 445-463 (1953).
3. A. F. Devonshire, Advan. Phys., 3, 85 (1954).
4. W. J. Merz, "Double hysteresis loop of $BaTiO_3$ at the Curie point," Phys. Rev., 91, 513 (1953).
5. M. Ya. Shirobokov and L. P. Kholodenko, "The thermodynamic theory of ferroelectric effects in crystals of barium titanate type," Zh. Éxperim. i Teor. Fix., 21, 1239-1249 (1951).
6. L. P. Kholodenko, "The thermodynamic theory of ferroelectric effects in barium titanate," Zh. Éxperim. i Teor. Fiz. (in press).
7. L. P. Kholodenko, "Theory of phase transitions in barium titanate," Zh. Éxperim. i Teor. Fiz. (in press).

[12] See, for example, [3, 6].

ELECTRON-DIFFRACTION DETERMINATION OF THE STRUCTURE OF ANTIMONY TELLURIDE

S. A. Semiletov

Institute of Crystallography, Academy of Sciences of the USSR
Translated from Kristallografiya, Vol. 1, No. 4, pp. 403-406, July-August, 1956
Original article submitted March 20, 1956

The structure of Sb_2Te_3 was studied by electron diffraction. In place of the earlier-proposed structure with a statistical distribution of Sb and Te atoms, a structure of the tetradimite type (Bi_2Te_2S) was established. The lattice spacings (hexagonal) were $a = 4.24 \pm 0.02$ kX, $c = 29.90 \pm 0.10$ kX. The cell contained six Sb and nine Te atoms. The atoms occupied positions (a) and (c), the space group was $R\bar{3}m$ with parameters $Z_{Sb} = 0.400$, $Z_{Te} = 0.211$.

According to published data [1], the Sb–Te system contains a compound Sb_2Te_3; magnetic-susceptibility measurements of the alloys showed that in the solid state this could dissolve 3-5% Sb and 2-4% Te. The question of the type of solid solution formed with the components by the compound Sb_2Te_3 has so far not been studied.

There is also a short published communication on the structure of Sb_2Te_3 [2].

According to this paper, Sb_2Te_3 crystals have a rhombohedral cell with a statistical distribution of the Sb and Te atoms.

An analogous indication is given for the structures of Bi_2Se_3 and Bi_2Te_3, but our own results [3] show this to be erroneous. We also note that the compound Sb_2Te_3 is distinguished by a clear maximum on the phase diagram and singular points on the composition/property curves, i.e., it is a daltonide in the terminology of Kurnakov, and a characteristic feature of these is known to be an ordered rather than statistical distribution of the atoms.

In the present investigation, we determined the structure of Sb_2Te_3 by electron diffraction. The samples for study were prepared in the form of layers 10^{-6} cm thick by vacuum condensation of the vapor onto celluloid-film substrates and rocksalt crystals. In preparing the samples we either evaporated the original components from two evaporators (Vekshinskii method) or evaporated an already prepared alloy corresponding in composition to Sb_2Te_3; condensation was effected onto substrates at room temperature, and after sublimation the samples condensed onto rocksalt crystals were vacuum annealed at 200°C for 20-30 min.

In studying samples prepared by the method described, we obtained two different types of electron-diffraction pictures, namely, some with a small number of diffuse rings (Fig. 1), and others of the oblique-texture type (Fig. 2).

The electron-diffraction photographs of the first type were obtained from unannealed and those of the second type from annealed specimens. In the first case the sample was set perpendicular to the beam, and in the second at an angle of ~65°. The values found from the texture photograph (standard NH_4Cl) for the spacings of the hexagonal lattice were

$$a = 4.24 \pm 0.02 \text{ kX};$$

$$c = 29.90 \pm 0.10 \text{ kX}.$$

Typical of diffraction pictures of the texture type was a paired disposition of reflections on ellipses with $h - k \neq 3n$, associated with the existence of a rhombohedral extinction condition, while the

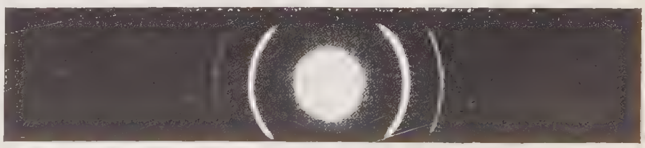

Fig. 1. Electron-diffraction photograph of Sb_2Te_3 with diffuse rings.

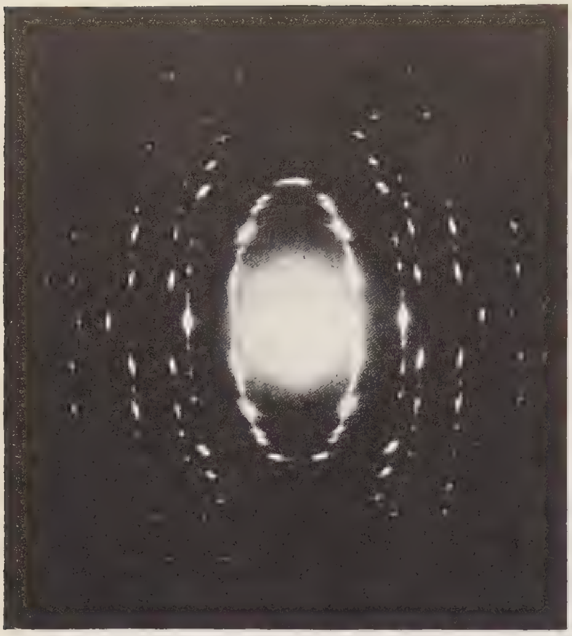

Fig. 2. Electron-diffraction texture photograph of Sb_2Te_3.

strongest reflections were disposed on layer lines with $l = 5n$.

The electron-diffraction photographs showed up to 45 layer lines with around 300 reflections.

We obtained analogous diffraction pictures earlier for samples of Bi_2Se_3 and Bi_2Te_3 [3]. This fact, together with the similarity between the spacings of the Sb_2Te_3 cell and the corresponding spacings of Bi_2Se_3 (a = 4.14 kX, c = 28.9 kX) and Bi_2Te_3 (a = 4.38 kX, c = 30.4 kX) clearly indicates that the several structures are similar.

This last fact is also confirmed on comparing the reflection intensities.

In carrying the work further, we started from the fact that the Sb_2Te_3 structure, like that of Bi_2Te_3, was based on a nine-layer tetradimite stacking of Te atoms, in which Sb atoms occupied two-thirds of the octahedral cavities. In the structure in question, Sb and Te atoms occupy the (a) and (c) positions of the space group $R\bar{3}m$.

The parameters of the atoms in the Sb_2Te_3 structure were determined in the following way. Antimony and tellurium are neighboring elements in the periodic system of Mendeleev and hence, to a fair degree of accuracy, their scattering powers may be regarded as equal.

Bearing this in mind, we obtain, after substituting the coordinates of the atoms in the expression for the structure amplitude and making certain transformations:

$$\Phi_{hkl} = 4\left(1 + 2\cos 2\pi \frac{h-k+l}{3}\right) \times$$

$$\times \left[(1 + 2\cos 2\pi l Z_{Te}) f_{Te} + 2\cos 2\pi l Z_{Sb} \cdot f_{Sb}\right]$$

$$\approx 4\left(1 + 2\cos 2\pi \frac{h-k+l}{3}\right)$$

$$\times\left[(1 + 2\cos 2\pi l Z_{Te} + 2\cos 2\pi l Z_{Sb}) \cdot f_{Sb}\right].$$

The expression in the first brackets either equals zero (for $h - k + l \neq 3n$) or three (for $h - k + l = 3n$), and since we are interested only in the relative intensities of reflections present in the photograph (i.e., for $h - k + l = 3n$), it may be omitted.

It follows from the expression in square brackets that the intensities of the reflections present in the photographs are independent of h and k and depend only on l. Taking this into account, and noting that reflections with l = 17 and 22 are practically absent from the photographs owing to the extremely low intensity, we obtain:

$$1 + 2\cos 2\pi \cdot 17\, Z_{Te} + 2\cos 2\pi \cdot 17\, Z_{Sb} \simeq 0$$

and

$$1 + 2\cos 2\pi \cdot 22\, Z_{Te} + 2\cos 2\pi \cdot 22\, Z_{Sb} \simeq 0.$$

These equations are valid for $Z_{Te} \simeq 0.2$ and $Z_{Sb} \simeq 0.4$, or inversely.

The parameters so obtained are refined by minimizing the function

$$R(Z) = \frac{|\Sigma|\Phi_{theor}| - |\Phi_{exp}||}{\Sigma|\Phi_{exp}|}.$$

These calculations were only made for reflections of the type $11l$ and $21l$, since the intensities of the reflections, as already mentioned, depend only on l, ellipses with $h - k = 3n$ (for example 110) containing reflections with $l = 3n$ and ellipses with $h - k \neq 3n$ (for example 210) reflections with $l \neq 3n$. In other words, in order to allow for all values of l two ellipses and not one must be taken.

In this we again took $f_{Sb} = f_{Te}$ to simplify the calculation of Φ_{theor}.

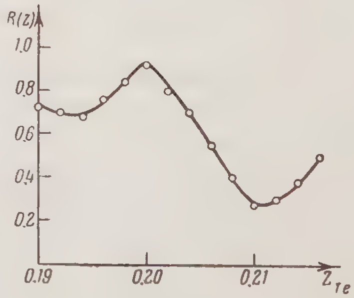

Fig. 3

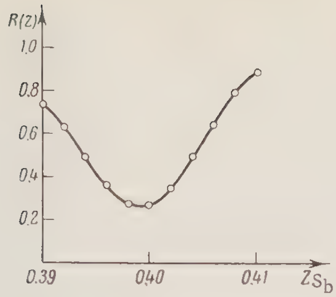

Fig. 4

Calculations were made in two ways. First, Z_{Sb} was kept equal to 0.4 and a minimum found for $R(Z_{Te})$, the Z_{Te} varying from 0.190 to 0.216 in steps of 0.002.

From this calculation the curve of Fig. 3 was drawn, with a minimum at $Z_{Te} = 0.211$.

In the second stage, a minimum of the function $R(Z_{Sb})$ was found with Z_{Te} fixed at 0.211.

Figure 4 shows a curve with a minimum at $Z_{Sb} = 0.4$ relating to this part of the calculations.

Here, Z_{Sb} varied from 0.390 to 0.410 in steps of 0.002.

The resultant atomic-parameter values were $Z_{Te} = 0.211$, $Z_{Sb} = 0.400$.

The shortest interatomic distances calculated from these values of parameters were as follows: $Sb-Te_I = 3.06$ kX; $Sb-Te_{II} = 3.16$ kX; $Te-Te = 3.62$ kX.

Finally, the factor R fell to 0.27, i.e., 27%.

As regards the earlier-mentioned photographs with diffuse rings (Fig. 1), these could be indexed on the basis of a hexagonal cell with spacings $a = 4.24$ kX, $c' = c/5 = 29.9/5 = 5.98$ kX. As indicated earlier, the strongest reflections on the texture photographs had $l = 5n$. It is possible that on the photographs with diffuse rings the weak reflections with $l \neq 5n$ are insignificant because of the great diffuseness; hence, in indexing them we take a cell with $c' = c/5$.

However, there is also a second possibility, namely, that immediately after sublimation a non-equilibrium phase is formed on the substrate, having a statistical, disordered arrangement of the Sb and Te atoms, and that only after annealing is the tetradimite structure with ordered atoms formed.

In fact, in the case of a statistical arrangement of atoms, each layer of the tetradimite stacking AcBAcBaCB... will be identical in composition with all other layers, i.e., we shall obtain stacking of the ACBACB type, in which the cell spacing along the c axis is only determined by the arrangement of the layers, and since this arrangement is repeated every three layers, the spacing c' is five times smaller than the basic spacing (in the tetradimite structure repetition occurs every fifteen layers).

Thus, in the case of a statistical arrangement of atoms, we have a rhombohedral stacking ACBACB, in which each layer contains $3/5$ Te atoms and $2/5$ Sb atoms, i.e., in the hexagonal cell there are $3(3/5\,Te + 2/5\,Sb)$ "atoms" with coordinates 000, $\frac{1}{3}\frac{2}{3}\frac{1}{3}$, $\frac{2}{3}\frac{1}{3}\frac{2}{3}$, and atomic scattering factor $f_{av} \sim 3f_{Te} + 2f_{Sb}$.

The structure amplitude of such a model

$$\Phi_{hkl} = \left(1 + 2\cos 2\pi \frac{h-k+l}{3}\right) \cdot f_{av}$$

equals either zero (for $h - k + l \neq 3n$), or 3 (for $h - k + l = 3n$).

Hence, the experimental Φ_{hkl} of the reflections present in the photograph should fall off as $\sin v/\lambda$ increases in analogy with the fall in the curves, i.e., reflections with large d should have larger amplitudes.

TABLE 1

№	2r	d	hkl	I/p	$\Phi^2 = \frac{I}{pd^2}$	$\lvert\Phi\ \text{exp}\rvert$
1	24.6	3.20	$\bar{1}01$	100	10	3.1
2	33.7	2.34	102	11	2	1.4
3	36.0	2.19	110	70	14.5	3.8
4	43.5	1.82	201	36	11.0	3.3
5	49.5	1.60	$\bar{2}02$	11	4.5	2.1
6	54.0	1.46	113	1	0.5	0.7
7	56.4	1.40	$21\bar{1}$	5	2.0	1.4
8	61.0	1.29	212	2	1.2	1.1
9	63.5	1.26	300	5	3.0	1.7

The experimental data presented in Table 1, however, show that the model with the statistical arrangement of atoms does not satisfy this (since $\Phi_{110} > \Phi_{102}$, $\Phi_{21\bar{1}} > \Phi_{113}$, $\Phi_{300} > \Phi_{212}$, $\Phi_{300} > \Phi_{113}$).

Thus, the first proposition, according to which rings with $l \neq 5n$ are invisible on the diffuse-line photographs because of the great line spread, is nearer to reality than that based on a statistical disposition of atoms.

LITERATURE CITED

1. M. Hansen, Constitution of Binary Alloys [Russian translation] (IL, 1941).
2. Strukturbericht, Bd. II (Leipzig, 1937).
3. S.A. Semiletov, "Electron-diffraction study of the structure of sublimed layers of Bi–Se and Bi–Te," Tr. Inst. Kristallogr. 10, 76-84 (1954).

NATURE OF AMORPHOUS ANTIMONY

G. A. Kurov and Z. G. Pinsker

Institute of Crystallography, Academy of Sciences of the USSR
Translated from Kristallografiya, Vol. 1, No. 4,
pp. 407-409, July-August, 1956
Original article submitted May 11, 1956

Thin films of antimony prepared in the form of a wedge by vacuum evaporation were studied. A sharp variation in the electrical properties of the films, associated with structural transformations taking place within them, was observed. It was found that as amorphous antimony transforms into crystalline there is a sharp rise in electrical conductivity and the sign of the current carriers changes. The structure of the samples was checked by electron diffraction at the same time as the electrical measurements. It was concluded that the transformation observed was not recrystallization but a phase transformation of a metastable amorphous phase of antimony into a crystalline phase.

It is known that thin films of antimony obtained by vacuum evaporation onto a cold substrate develop a metastable phase, which according to many authors [1-4] is amorphous. This is indicated, in particular, by electron-diffraction examination of such films [1]. The electron-diffraction picture shows diffuse haloes instead of the sharp lines typical of the crystalline state. The intensity maxima of the haloes lie at diffraction angles differing from those corresponding to the lines of crystalline antimony [2]. It is also found [2] that when the phase in question transforms into the crystalline state, the short-range order of the atoms in the structure changes. Studies made of the electrical properties of antimony films [3] showed that in fairly thin layers (~100 Å) the antimony had a negative temperature coefficient of resistance over a wide temperature range (from extremely low to room temperature), i.e., constituted a semiconductor. On heating to a certain temperature, depending on the thickness and other factors, this layer underwent irreversible transformations. At the same time the electrical conductivity sharply increased. The transformations in antimony films were also accompanied by a rise in the reflection coefficient of visible light [4].

However, despite the investigations described, the question as to whether amorphous antimony constituted a new allotropic modification, or whether we were dealing with the same crystalline antimony in a highly dispersed state, cannot be regarded as fully decided. In this paper we study the variation in certain electrical properties of thin films of antimony, in connection with structural transformations taking place in them. We feel that the data here presented should be useful in solving the problem in hand.

The change in properties, on passing from the amorphous to the crystalline state, can be followed most clearly by studying a layer of variable thickness prepared in the form of a wedge [4]. Such a layer may be obtained by evaporating antimony in a high vacuum with subsequent condensation on a suitable substrate. On the sample surface directly above the evaporator, the layer has its greatest thickness, this falling monotonically on passing away from the evaporator. With diminishing thick-

Fig. 1. Photograph of the film near the edge of the transformation boundary (by transmitted light, x 72).

Fig. 2. Photograph of the film near the edge of the transformation boundary (by reflected light, × 1440).

ness the layer gradually becomes transparent, taking on a blue-violet color (in transmitted light). Then comes a sharp boundary beyond which the layer is still more transparent and has a brown tint [4].

We evaporated the antimony in a system of the same type as that described in [5] with a pressure of about 10^{-5} mm Hg. The evaporator was a nickel tube with a slit along the generator (slit length 100 mm, breadth 0.2 mm). Condensation took place on glass plates of 100 × 25 mm . Figure 1 shows a micrograph of part of an antimony wedge near the transformation boundary, obtained in transmitted light. Below the boundary, i.e., on the side of reduced film thickness, the transparency rapidly increases. Figure 2 shows a photograph of the same film taken in reflected light. We see that on passing through the boundary in the direction of decreasing thickness the reflection coefficient of visible light diminishes sharply.

The film was studied by electron diffraction on both sides of the transformation boundary. For these experiments the antimony wedge was evaporated onto a thin celluloid film and simultaneously onto a glass plate parallel to this (in order to control the position of the transformation boundary).

Figure 3 shows an electron-diffraction photograph of the part of the wedge below the transformation boundary. The picture with haloes shown in Fig. 3 is typical of amorphous antimony. Above the transformation boundary the film is crystalline (Fig. 4), the dimensions of the crystallites being very small (about 10^{-6} cm). On passing upward from the boundary, the grain size increases and the grains become visible to the unaided eye.

In order to determine the thickness of the amorphous-antimony films, we used a multiple-beam interferometry method [6]. We measured the height of the step formed by the edge of the film on the glass substrate. The method is described in detail in [7].

It was thus established that the amorphous antimony deposited on the neutral substrate (glass) was preserved for a long time at room temperature (without turning into crystalline form) in films up to 110 or 130 Å thick.

Besides the electron-diffraction investigations, we measured the electrical conductivity of the amorphous and crystalline antimony, and also determined the sign of the carriers. In working with very thin semiconducting films (thinner than 100 Å) it is important to ensure good electrical contact of the sample with the measuring probes. In view of this, we made a slight change in the method of producing the films. Evaporation was effected simultaneously from two evaporators situated over the ends of the glass plate. This gave a layer of crystalline antimony separated by a band of amorphous film. Reliable contact between the amorphous part of the sample and the measuring probes was then ensured by the fact that the latter were set up in the thicker crystalline parts. The electrical conductivity of the amorphous films was $\sigma \simeq 1\,\Omega^{-1}\text{cm}^{-1}$. After heating to 80 or 100°C, the amorphous film crystallized and its electrical conductivity rose to $\sigma \simeq 2 \cdot 10^2\ \Omega^{-1}\text{cm}^{-1}$, i.e., by a factor of 200.

The sign of the carriers in the semiconducting layer may be determined from the sign of the

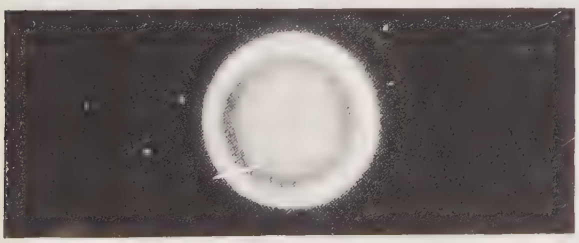

Fig. 3. Electron-diffraction photograph of amorphous antimony.

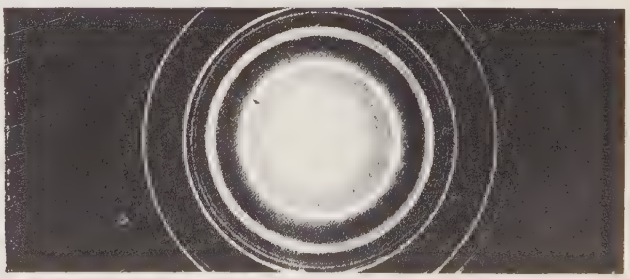

Fig. 4. Electron-diffraction photograph of crystalline antimony.

thermal emf. For measuring the thermal emf of very thin films, we used a system with a fine control of the pressure of the thermoprobes on the sample. This consisted of two levers (beams). To one end of each of the levers was fixed a thermoprobe; on the other was a counterweight. In the middle of the lever was placed a quartz wedge, bearing with its sharp edge on a polished brass surface. The pressure of the thermoprobe on the film was regulated by moving the counterweight. The temperature difference of the thermoprobes was 40°C. For films of crystalline antimony, the thermal emf was $\alpha = +30\ \mu V/°C$ (with respect to copper) at temperatures from room to 60 or 70°C. At the transformation boundary the thermal emf underwent a jump with a change of sign and became equal to $\alpha = -100$ to $-120\ \mu V/°C$; thus, the amorphous antimony has electron- and the crystalline, hole conductivity, i.e., we have an n-p junction in the wedge.

Thus, at the present time, it is established that in thin layers of antimony obtained by vacuum evaporation there is an irreversible transformation accompanied by sharp changes in the properties and structure of the layers.

The structure typical of the amorphous phase is replaced by crystalline. At the same time there is a change in the short-range order of the atoms. The electrical conductivity and reflection coefficient of light rise sharply, the sign of the carriers changes, and the semiconducting layer becomes metallic. If we were dealing with recrystallization instead of a phase transformation, then, instead of the sharp boundary, we should find a smooth change in properties along the wedge since, as the thickness of the layer diminished, so would the linear dimensions of the crystallites. Analysis of all the data available in the literature, as well as our own results, indicates that, on heating or increasing the thickness of antimony films, there is a phase transformation from the amorphous metastable state to the crystalline, and not recrystallization.

LITERATURE CITED

1. I.A. Prins, "Diffraction of electrons in amorphous and crystalline antimony," Nature, 131, 760-761 (1933).
2. L.I. Tatarinova and Z.G. Pinsker, "Electron-diffraction study of amorphous antimony by Fourier analysis of the intensity curve," Dokl. Akad. Nauk SSSR, 95, 2, 265-268 (1954).
3. J. Cohen, "Semiconducting films of antimony," J. Appl. Phys., 25, 6, 768-801 (1954).
4. S.A. Vekshinskii, New Method for the Metallographic Study of Alloys [in Russian] (1954).
5. G.A. Kurov, "Physical properties of films of certain magnesium alloys," Tr. Inst. Kristallogr., 11, 124-133 (1955).
6. S. Tolansky, Multiple-Beam Interferometry of Surfaces and Films (Oxford, 1948).
7. N.V. Gliki, Dissertation [in Russian] (Inst. Kristallografii, 1953).

INFLUENCE OF NONUNIFORM STRESSED STATE ON THE MECHANISM OF THE PLASTIC DEFORMATION OF THALLIUM AND CESIUM HALIDES

M. V. Klassen-Neklyudova and A. A. Urusovskaya

Institute of Crystallography, Academy of Sciences of the USSR
Translated from Kristallografiya, Vol. 1, No. 4,
pp. 410-418, July-August, 1956
Original article submitted February 14, 1956

It is shown that the formation of reoriented regions (kinks) in single crystals is possible only if deformation by compression and tension is accompanied by the production of macroscopic bending moments. In addition to the complex stressed state, it is essential for kink formation that the slip plane and slip direction should be oriented with reference to the axis of deformation of specimens in such a manner that deformation by slip is difficult.

Usually, the study of the plastic deformation of single crystals commences with investigations with uniform stress distribution, ensured by deformation by tension. However, even when polycrystalline specimens are subjected to uniform tension, uniformity of stress distribution inside the grains is disturbed, owing to the interaction of differently oriented grains. To understand the deformation process of the grains of polycrystals, it is essential to widen the range of investigations dealing with the study of the process of plastic deformation of single crystals, i.e., to elucidate the influence of changes introduced by the transition from the uniform to the nonuniform stressed state.

Complication of the experimental conditions may furthermore provide valuable information for understanding the plastic deformation of single crystals.

In one of our articles [1] dealing with the study of the plastic deformation of crystals of TlBr – TlI solid solution, it was shown that in longitudinal bending of prismatic specimens of these crystals, deformations were produced in them, which were localized in the form of a wide lamella or band (of the order of several millimeters wide). The boundaries of this band were not crystallographic boundaries. Within such a band was a set of wedge-shaped regions, in which the lattice had been rotated through a certain angle unsymmetrically with reference to the adjacent regions and to portions of the crystal external to the band.

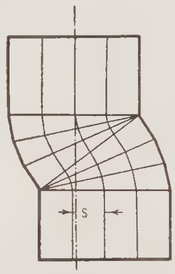

Fig. 1. Diagram of specimen in which a kink band has been formed on longitudinal bending.

Thus, the band or lamella was not a twin lamella formed in the deformation of the crystal, but some transitional region between two parts of the crystal which had been shifted by an amount s (Fig. 1). In [1], the suggestion was made that the phenomenon observed by us ought to be regarded as kink formation, which was first discovered by Mügge [2] in a number of minerals, and first produced by Orowan [3] as the result of plastic deformation by longitudinal bending of zinc single crystals.

It should be noted that in the deformation of single crystals and polycrystals of mineral and metals, other forms of plastic deformation, also due to the formation of regions twisted through different angles, are to be observed. These forms of deformation are known as "irrational twins" [4], "deformation bands" [5], "plates" [6], "accommodation bands" [7], and so forth.

The present article deals with a more detailed study of the phenomenon of kink formation, which we have observed not only in TlBr – TlI crystals, but

also in CsI and CsBr crystals. The formation of similar twisted regions has also been observed by us in the action of a concentrated load on naphthalene and bismuth single crystals [8].

Investigation of Kink Formation by Compression and Longitudinal Bending

These investigations were carried out on TlBr – TlI crystals grown by A. B. Zemtsov, and CsI and CsBr crystals grown by V. N. Varfolomeeva in the Laboratory for the Synthesis of Optical Single Crystals. Both groups of crystals were grown from the melt.

The specimens of thallium halide crystals of definite crystallographic orientations (determined by means of impact figures [5]) were cut out very slowly on an automatic fretsaw, designed by V. G. Govorkov. The specimens of cesium iodide and bromide were cut out by means of a thread saw using water as solvent. The specimens for compression testing had the form of four-sided prisms with cross section 3 × 4 to 5 × 5 and height 8-30 mm. The surface of the specimens was ground on ground glass with abrasives and then carefully polished. (The TlBr – TlI crystals were polished with moist washleather and chromic oxide, and the CsI and CsBr crystals on felt with water.)

Deformation was carried out in a special press with a device for the application of a gradual slow load. An ordinary vise was used for rapid deformation.

The specimens of various orientations were subjected to compression with uniform stress distribution over the cross section of the specimen. In accordance with published data [9], the slip elements of TlBr – TlI crystals were the $\{110\}$ planes and $<100>$ directions. As our investigations have shown, the slip elements were exactly the same in CsI and CsBr crystals.

In specimens, in which the compression axis coincided with the [111] and [110] directions, or with a direction close to one of these two directions, deformation by slip along one or several of the $\{110\}$ slip plane systems was observed on compression. Slip occurred for any ratios between the height of the specimens and their cross section, including also the case of longitudinal bending.

Specimens, the compression of which occurred along an axis coinciding with the [100] slip direction, behaved quite differently. With this orientation of the specimens, deformation by slip along planes of the rhombododecahedron and in the direction of the cube edges is forbidden. In the compression of these specimens, kinks occurred near their ends. Figure 2 shows a photograph of

Fig. 2. TlBr – TlI crystal deformed by compression strictly along the principal axis, coinciding with the [100] slip direction. At the ends of the specimen are visible deposits consisting of a number of kink bands.

such a specimen taken in natural transmitted light. The kinks are visible in the form of dark regions at the ends, which do not transmit light because of the presence of a large number of cracks in the kink bands. The occurrence of kinks at the ends is accompanied by a crackling sound. These experiments showed that with uniform compression of thallium and cesium halide crystals, kinks occurred only for an orientation of the specimens such that slip was impossible. On the basis of the fact that with such an experimental arrangement kinks occurred only at the ends of the specimen, the following conclusion may be made: Kink formation is due to the presence of a complex stressed state produced at the ends of specimens as the result of friction between the specimen and the jaws of the press.

In the next series of experiments, we subjected the specimens to nonuniform compression. Nonuniform stress distribution was produced in different ways; either the rectangular specimen was placed askew between the press jaws (Fig. 3a), or the axis of the specimen was arranged strictly perpendicular to the press jaws, but the end faces of this specimen were not cut at right angles to its other sides (Fig. 3b). In either case, the load was applied to the edge or to the apex of the trihedral angle of the specimen. With such methods of compression, kinks were produced without trouble in specimens in which the principal axis coincided with the slip direction or deviated slightly from it, the kink band being situated near the middle of the specimen. Compression, under similar conditions, of specimens whose principal axis was parallel to the [111] or [110] directions failed to produce kinks. Experiments with nonuniform compression showed, however, a wider range of orientation of the specimens, for which the production of kinks on compression was observed. It was found that kinks may be produced in specimens in which the axis makes an angle of 0-25° to the direction of the cube edge. These experiments also showed that the width of

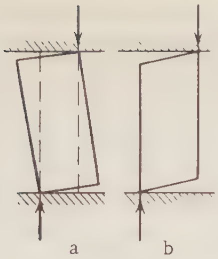

Fig. 3. Compression conditions of specimens of crystals of thallium and cesium halides, with the principal axis parallel or nearly parallel to the slip direction, for which kink-band formation is observed.

the kink band depends directly on the angle of skew of the specimen in the case of compression by the method shown in Fig. 3a, and also on the angle formed by the axis of the specimen with the slip direction. (This latter relationship is in agreement with the results of similar experiments by Gilman [11] with zinc.) If the angle between the axis of the specimen and the slip direction exceeds 25°, the kink band is not clearly marked. Figure 4 shows photographs of deformed CsBr specimens taken in polarized light (Fig. 4c was taken with an interposed gypsum plate). The axis of the first specimen (Fig. 4a) coincides exactly with the slip direction, the kink band is clearly marked and quite narrow. In the next photograph (Fig. 4b), a specimen is shown with the axis differing from the slip direction by an angle of 21°. The outlines of this specimen were smoother and the band narrower than in the specimen shown in Fig. 4a. Figure 4c shows the upper part of a CsBr specimen, in which a kink has formed at the end.

The first two specimens (Figs. 4a,b) assumed the shape of a knee bend. According to Euler, a knee bend is one of the forms of longitudinal bending of elastically isotropic rods, which a rod assumes as the result of loss of elastic stability, when one end of it is permanently fixed and the other is able to move along the jaws of the press. It should be noted that in our experiments the ends of the specimens were not rigidly secured, and the possibility was not precluded that one of the ends could be displaced slightly in the horizontal direction. The kink bands were formed at the point of inflection of the axis of the specimen. Longitudinal bending is produced in the compression of rods, or due to the presence of inhomogeneity in cross section along the length of a specimen or in consequence of eccentricity of the applied forces. In all the cases we have investigated, kinks were formed in the presence of macroscopic bending moments.

To determine the rate of formation of a kink band, use was made of motion picture photography of the compression process in polarized light (with a rate of exposure of 24 frames per second). These experiments showed that kinks are formed in period of less than $1/_{24}$ sec.

The sound emitted by a specimen during kink formation may be due to two causes. Either cracks are formed during kink formation, these cracks being propagated with the speed of sound, or reorientation of lattice regions occurs in the kink band with a speed approaching the speed of sound, as in twinning. The formation of a large number of cracks in the region of a kink is confirmed by the formation of regions which do not transmit light (Figs. 2 and 4a).

It should be noted that the formation of the kink shown in Fig. 4a was accompanied by a crackling sound, while the formation of smooth kinks, like that shown in Fig. 4b, was not accompanied by any emission of sound.

Investigation of Deformation by Uniform Tension

The investigation of the formation of kinks in crystals on deformation by compression led us to conclude that in kink formation a part is played by the crystallographic orientation of the principal axis of prismatic specimens with reference to the axis of compression, and by nonuniform stress distribution over the cross section of specimens (presence of macroscopic bending moments).

To elucidate whether the presence of a nonuniform stressed state was really necessary for

Fig. 4. Photographs in polarized light of kink bands formed on compression of cesium bromide crystals.

kink formation, we carried out experiments, in which TlBr – TlI single crystals were subjected to uniform tension. Platelets were cut from these single crystals. The middle parts of the lateral surfaces of the platelets were carefully filed out with a fine file to such an extent that the cross section of the operative part of each specimen was reduced to one-half or one-third the cross section of the part of the specimen located in the jaws of the machine (the length of the operative part was 10 mm, and its cross section was 4-5 mm^2). The surfaces of the specimens were carefully ground and polished. The specimens were then heated in a thermostat to 280°C, kept at that temperature for one hour, and then cooled slowly for 8-10 h. Relief of internal stresses was verified by examination of the specimens in polarized light.

The specimens were subjected to tensile stress on an apparatus of the type of a Polyani machine, in which the specimens were clamped immovably by one end, while the other end was secured (through a dynamometer) to a gradually raised screw. Uniformity of tension was ensured by the use of a cardan type clamp. In the course of the application of tension, the stress distribution in the specimens was under continuous observation in transmitted polarized light. Specimens were subjected to tension in which the principal axis was variously oriented with reference to the principal crystallographic directions.

The tension experiments showed that if specimens of different orientations are subjected to tension exactly along their principal crystallographic axis, plastic deformation by slip occurs with the same slip elements as in the case of compression. An exception is provided by tension along the [100] direction, which is the slip direction of these crystals. In this case, the specimens fractured without appreciable change in length (we have so far been unable to observe mechanical twinning in these crystals). In most cases, fracture occurred along the {110} plane, and the surface of the fracture was either a smooth surface or toothed, the teeth being surrounded by smooth, almost specular, planes of the rhombododecahedron.

Fig. 5. Photograph in polarized light of portion of TlBr – TlI crystal subjected to tension. Four systems of slip traces are to be seen.

The slip occurring when tension was applied to the specimens along directions differing from the slip direction, always occurred along two or more planes of the rhombododecahedron, and with increase in the angle of deviation of the axis of tension from the [100] direction, the proportion by which the second system of slip planes participated increased. Figure 5 shows part of a specimen adjacent the tip. The axis of the specimen made an angle of ~25° with the [100] direction. Visible on the surface of this specimen are four systems of slip traces, the sites of emergence on the surface of different planes of the rhombododecahedron.

These experiments thus showed that with uniform tension, plastic deformation occurred only by complex slip. The formation of regions with reoriented lattice was not observed in the case of deformation caused by tension.

The experiments were made at room temperature and the rate of deformation was $2.5 \cdot 10^{-4}$ to $1.1 \cdot 10^{-6}$ cm/sec.

Figure 6 shows tensile stress curves for specimens of three orientations. During tension of the specimens, the axis of which was parallel to one of the <100> directions, being the only slip directions in these crystals at 20°C, slip was impossible, and therefore plastic deformation did not occur, and fracture occurred immediately after elastic deformation. Tension in the [111] direction was more favorable for the occurrence of plastic deformation by slip; since, in this case the direction of the stress bisects exactly the angle between the slip direction and the normal to the slip plane. The behavior of specimens subjected to tension in the [110] direction was intermediate between the first and second cases.

Furthermore, for tension curves of TlBr – TlI crystals, the presence of serrations on the part of the curve corresponding to plastic deformation is characteristic; these serrations are caused by the drop in stress at a given elongation of the specimen. A sharp drop in stress is usually observed in twinning, and such drops in stress are not characteristic of deformation by slips. For elucidating this phenomenon, we examined specimens in polarized

Fig. 4c.

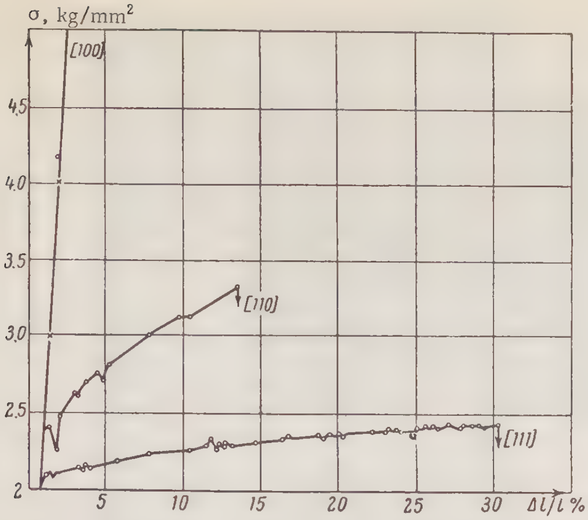

Fig. 6. Tensile stress curves at room temperature of TlBr – TlI crystals for three crystallographic directions. The top curve corresponds to tension along [100] (the graph only shows part of it; fracture corresponds to $\sigma \sim 10$ kg/mm^2). The middle curve corresponds to tension along the [110] direction. The bottom curve corresponds to tension along the [111] direction.

Fig. 7. Diagram of experiment on subjecting a crystal to tension with bending, in which the formation of a kink band is observed.

light, while they were under tensile stress. It was found that each serration on the tension curve corresponded to an avalanche-like formation of a packet of displacements. The latter were formed at any point on the specimen, and in some cases the avalanches of displacements spread over the entire operative part of the specimen.

The influence of various factors on the form of the deformation curves of TlBr – TlI crystals has been studied by Regel' and Zemtsov [12].

Production of Kinks in Tensile Deformation Accompanied by Bending

In view of the fact that in pure tension we were unable to obtain a kink band, we tried producing in the specimen a nonuniform stressed state, in addition to tension. The compression experiments had shown that one of the conditions for the occurrence of kinks in crystals was the presence of macroscopic bending moments. Making use of this result, we subjected specimens to bending, in addition to tension, this being done by oblique attachment of the specimens in the clamp, as shown in Fig. 7. With such a method of clamping the specimen, its left-hand part (see Fig. 7) was subjected to tension to a greater degree than the right-hand part, resulting in bending of the specimen, with a convexity directed to the right. (It should be noted that the obliquity in clamping the specimens should be fairly large.) Under these deformation conditions, we finally succeeded in obtaining kink bands, but these bands were not so pronounced as those obtained by compression. The kink bands were formed in the middle portion of the specimens or in regions which were transitional from the operative part to that held by the grips. It was thus possible to produce kink bands in TlBr – TlI specimens, subjected to tension in the [110] direction. With such orientation of the specimens, two {110} planes (one perpendicular to the axis of tension and the other parallel to it) were forbidden for slip, but slip could take place along the other four planes of the rhombododecahedron, making an angle of 60° (30°) to the direction of the axis of tension. The direction of the tension in these planes makes an angle of 45° with the axis of tension. Slip along these planes, however, does not preclude the possibility of kink formation.

Figure 8a shows a portion of a TlBr – TlI specimen subjected to tension with bending. The axis of the specimen is parallel to the [110] direction. In the middle part of the specimen is to be seen a slightly bent lamella (dark on a light background). Higher magnification shows the complex structure of this lamella (Fig. 8b). This specimen was deformed not only with kink formation but also with complex slip (on the photograph reproduced, the displacements are not visible).

When TlBr – TlI specimens having other orientations were subjected to tension with bending, kinks were not produced. In deformation under such conditions of specimens, whose principal axis coincided with the [111] direction, slip occurred simultaneously along several systems of planes of the rhombododecahedron. Specimens whose axis was parallel to the [100] direction fractured without appreciable sign of plastic deformation. Evidently, when specimens of such orientation were subjected to tension with bending, fracture occurred before kinking was able to take place in them.

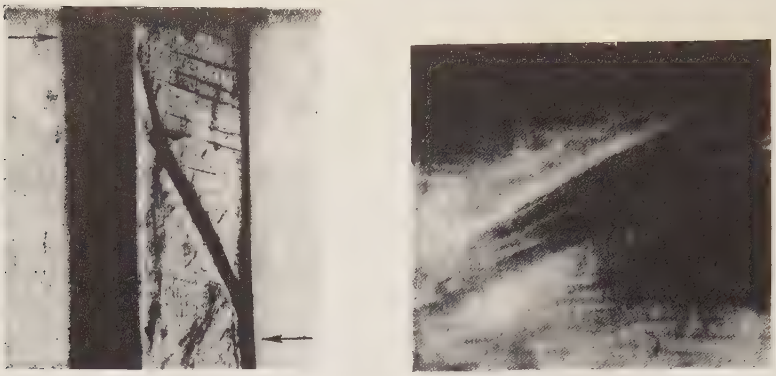

a b

Fig. 8. TlBr–TlI specimen in which a kink band has been formed by tension with bending: (a) Form of specimen with kink band at × 18; (b) portion of the same kink band at × 180. Inside the band, over its entire extent, is to be seen one boundary of a wedge-shaped region. Several such boundaries are to be seen in the lower part of the band.

Thus, experiments on the tension of TlBr–TlI crystals, at room temperature and a rate of application of tensile stress of $2.5 \cdot 10^{-4}$-$1.1 \cdot 10^{-6}$ cm per sec, showed that for plastic deformation by kink formation to take place under conditions of tension, it was necessary to use specimens of a definite orientation (with the axis parallel to [110]) and to produce a complex stressed state resulting in a combination of tension and bending. In the case of tension alone or bending alone, the formation of kink bands was not observed.

Investigation of the Influence of Local Stresses at Defective Places on Kink Formation

Some investigators (Hess and Barrett [13], Gilman and Read [14]), on the basis of their experiments with metals, assert that kink formation is assisted by the presence in the specimens of local heterogeneities. We made special experiments to verify this statement.

Defects were made intentionally in the specimens before deformation, either surface scratches were made, or throughgoing orifices were drilled in them, or specimens with cracks were selected. In a number of specimens, the surface was damaged by pricking it with a needle in the deformation process (with the object of avoiding recovery effects).

In carrying out these experiments, we were never able to observe, in crystals of thallium and cesium halides, the occurrence of kinks originating from the damaged portions; only packets of displacements were formed around the damaged portions.

In the case of uniform compression along the slip direction of specimens provided with a surface scratch, the occurrence of kinks was observed near the ends, but not in the vicinity of the scratch. If specimens having an orientation favorable for slip, but unfavorable for kink formation, were subjected to uniform compression, the presence in them of local defects (needle pricks, orifices, scratches) failed to cause the occurrence of localized kink bands. Deformation occurred by normal slip, while under very high loads the specimens deformed by slip with longitudinal bending. The presence of scratches and pricks in thallium halide specimens subjected to tension did not appreciably affect the course of plastic deformation. The specimens were deformed by ordinary slip, and fracture did not always occur near such defects.

The presence of an orifice, and also pressure applied to the specimen during tension, did, however, have some influence on the course of plastic deformation, and on the appearance of the fracture of the deformed specimen. In specimens whose length did not coincide with the [100] direction, and in which there was an orifice in the central part, slip occurred in the initial stage of plastic deformation along a system of planes of the rhombododecahedron. At the same time, elastic stresses were set up near the orifice, and in polarized light these stresses looked like multicolored isochromes, arranged in the form of a cross, with branches diverging from the orifice. In the tension process, the number of slip bands increased and the color of the isochromes varied. At a certain value of the stress, in addition to the slip traces covering the whole of

Fig. 9. Photograph in polarized light of a portion of the TlBr–TlI specimen with orifice, which has been subjected to tension. In the application of tension to this specimen, pockets of displacements have appeared from two sides of the orifice.

the surface of the specimen, slip traces appeared suddenly ("explosively"), diverging from the orifice in the form of a bundle of lines along four or two directions. These lines corresponded to slip traces along planes of the rhombododecahedron, but differed from the slip planes which acted on the initial stage of plastic deformation. Soon after the appearance of these cruciform slip traces, fracture of the specimen occurred, this necessarily taking place near the orifice. Figure 9 shows a photograph of part of a TlBr–TlI specimen, subjected to tension, having an orifice at its center. This specimen was subjected to tension until two packets of lines appeared near the orifice, but was not stressed to fracture.

Thus, contrary to statements by Hess and Barrett [13[, and Gilman and Read [14], our experiments showed that the presence of stress concentration alone at defects does not cause the formation of kinks in thallium and cesium halide crystals. Only packets of displacements are produced near damaged places in crystals of the halides. The formation of kinks near scratches in the experiments of Gilman, Read, Hess, and Barrett was due to the specific nature of the substance (metal) they investigated.

The fact that artificial damage to crystals and the presence of local defects in the case of metals produce kink formation, while such influence is absent in the case of thallium and cesium halides, may be explained by means of data on the investigation of the process of plastic deformation in crystals of different substances (with bonds of widely differing types) under the action of a concentrated stress [8, 10,15,16]. These investigations showed that when a concentrated stress acts on crystals, plastic deformation figures (surface and throughgoing impact and pressure figures) are formed. In crystals of the halides TlBr, TlI, TlBr–TlI, CsI, and CsBr, and also in crystals of galena (PbS), deformation by slip underlies the formation of these figures. Under the action of a concentrated stress on Zn, Bi, and Sn crystals, similar plastic deformation figures were formed, but always because of twinning and accompanying accommodation kinks [7], representing regions intermediate between the undeformed crystal and one of the boundaries of the twinning plane.

These investigations have thus shown that the process of plastic deformation at places of stress concentration in halide crystals differs from the deformation process under similar conditions in metals.

Summary

1. It has been found that plastic deformation in thallium and cesium single crystals takes place because of the occurrence of kinks if there is a complex stressed state, characterized by the presence of macroscopic bending moments, in addition to tension or compression.

2. It has been found that for kinks to form on compression or tension, it is essential, in addition to bending moments, for the crystallographic axes to be oriented in a definite manner with reference to the axis of deformation of the specimen.

3. For kink formation to occur during deformation by compression, it is necessary that the orientation of the specimen should not permit deformation by slip, that is to say, the axis of compression of the specimen should be parallel to the slip plane or deviate from it by an angle not exceeding 25°. The crystallographic slip direction also should be either parallel to the axis of compression or deviate from it by not more than 25°.

4. With the application of uniform tension to TlBr–TlI crystals, no kinks are formed for any crystallographic orientation of the specimen. In this case, there occurs deformation by slip or fracture without appreciable change in length of the specimen.

5. The formation of kinks with the application of nonuniform tension (tension with bending) al-

so only occurs for a definite orientation of the specimen, i.e., when the direction of the axis of tension coincides with the [110] direction. If the axis of tension coincides with the [100] direction, in the case of tension with bending, as in the case of uniform tension, before fracture of the specimen, only the linear part of the deformation curve can be observed. Specimens subjected to tension with bending in the [111] direction are deformed entirely by complex slip, which may occur along six systems of slip planes.

6. Contrary to the results of experiments by Gilman, Read, Hess, and Barrett with zinc, our investigations showed that the presence of stress concentration at local defects does not cause kink formation in thallium and cesium halide crystals subjected to compression or tension.

7. The difference in the influence of local defects in our experiments and in the experiments of Gilman et al. is explained on the basis of a previously conducted comparative investigation of the mechanism of the formation of plastic deformation figures formed in metals and halide crystals when a concentrated stress acts on different faces of the crystals. A concentrated stress in metal crystals actually produces kink formation, accompanied by mechanical twinning, while under the action of a concentrated stress on thallium and cesium halide crystals, deformation occurs by complex slip, and kinks are not formed.

LITERATURE CITED

1. A.B. Zemtsov, M.V. Klassen-Neklyudova, and A.A. Urusovskaya, "Complex occurrence of plastic deformation of single crystals," Dokl. Akad. Nauk SSSR, 91, 4, 813-916 (1953).
2. O. Mügge, "Über Umlagerungen in Zwillingsstellung am Clorbaryum $BaCl_2 + 2H_2O$," N. Jb. Min., 1, 131 (1888)
3. E. Orowan, "A type of plastic deformation new in metals," Nature, 149, 3788, 643-644 (1942).
4. N.A. Brilliantov and I.V. Obreimov, "Plastic deformation in rocksalt. III," Zh. Éxperim. i Teor. Fiz., 5, 3-4, 330-339 (1935).
5. C.S. Barrett, "Structure of iron after compression," Trans. AIME, 135, 296-322 (1939).
6. A.V. Stepanov and A.V. Donskoi, "New mechanism of the plastic deformation of crystals," Zh. Tekhn. Fiz., 24, 2, 161-183 (1954).
7. D.C. Jillson, "An experimental survey of deformation and annealing processes in zinc," Trans. AIME, 185, 1009-1017 (1950).
8. A.A. Urusovskaya, "Impact and pressure figures in crystals of hexagonal metals," Tr. Inst. Kristallogr., 11, 140-145 (1955).
9. A. Smakula and M. Klein, "The plastic deformation and crystal orientation of thallium halides," J. Opt. Soc. Am., 39, 6, 445-453 (1919).
10. A.A. Urusovskaya, "Plastic deformation figures observed in crystals of the halides TlBr + TlI, CsI, and CsBr," Tr. Inst. Kristallogr., 12, 170-179 (1956).
11. J. Gilman, "Mechanism of ortho kink-band formation in compressed zinc monocrystals," J. Metals, 6, 2, 5, 621-629 (1954).
12. V.R. Regel' and A.B. Zemtsov, "Influence of the crystallographic orientation of TlBr – TlI crystals on the yield point in tensile testing," Tr. Inst. Kristallogr., 11, 166-171 (1955).
13. J.B. Hess and C.S. Barrett, "Structure and nature of kink-band in zinc," J. Metals, 185, 599 (1949).
14. J. Gilman and T. Read, "Bend-plane phenomena in the deformation of zinc monocrystals," J. Metals, 5, 1, 49-55 (1953).
15. M.V. Klassen-Neklyudova and A.A. Urusovskaya, "Throughgoing impact and pressure figures in cubic crystals of halides," Tr. Inst. Kristallogr., 11, 146-151 (1955).
16. A.A. Urusovskaya, "Mechanism of the formation of throughgoing impact figures in zinc," Tr. Inst. Kristallogr., 12, 180-185 (1956).

STRUCTURE OF FAULT (KINK) BANDS OF CERTAIN IONIC CRYSTALS

E. V. Kolontsova, I. V. Telegina, and G. M. Plavnik

M. V. Lomonosov State University, Moscow

Translated from Kristallografiya, Vol. 1, No. 4, pp. 419-424, July-August, 1956
Original article submitted March 23, 1956

Pressure-deformed single crystals of CsI and TlI–TlBr, previously studied in polarized light, were examined by narrow-beam x-ray photography. Inside the kink bands appeared sections of crystal constituting twins with respect to the original.

One of the manifestations of the inhomogeneous structure of plastically deformed crystals is the system of so-called fault or "kink" bands formed under certain conditions of deformation in single-crystal metals and ionic compounds. Investigations made by a number of authors [1-3] have shown that kink bands occur in crystals of different systems subjected to different forms of deformation over a wide temperature range. From this fact many workers have come to the conclusion that kink formation is a fundamental property of the deformation process, and that study of this phenomenon may therefore throw light on the mechanism of plastic deformation in crystals as a whole.

The external form of kink bands is much the same for different crystals, although the breadth of these regions varies over fairly wide limits, from one micron to several millimeters.

Structural examination of kink bands in papers hitherto published has been carried out by means of wide beams of x rays (diameter 0.5 mm and more); the diffraction picture on the photographic plate in this case is created by a large part of the crystal, so that it is practically impossible to establish laws governing the structure of the kink bands and regions close to them. Moreover, the comparatively wide kink bands observed in polarized light have internal fine structure [4].

In order to study the detailed structure of kink bands we took Laue photographs with beams of various diameters from 1 mm to 40 μ, in association with microscope observation in polarized light. This enabled us to correlate the fine structure of the deformed crystals given by x-ray data with the distribution of stresses inside the kink band. We studied single crystals of cesium iodide and a solid solution of thallium bromide and iodide deformed by pressure.

For the x-ray examination we took two sections of TlBr–TlI and CsI samples containing kink layers developed by longitudinal compression. The sections were given to us by the Institute of Crystallography.

The samples were prepared in the form of thin plates by grinding the deformed blocks. In order to eliminate possible bending, the blocks were glued to a glass plate. The crystallographic orientation of the samples is shown in Fig. 1.

The study of kink bands in the TlBr–TlI single crystals by optical methods was effected in the Institute of Crystallography by Klassen-Neklyudova et al. [4]. Figure 1a shows a schematic picture of the stress distribution from their data, as well as certain details in the kink band which they did not notice (the latter are shown by a thick line).

The optical picture of a kink band in a CsI crystal is shown in Fig. 1b. As in the TlI–TlBr crystals, we can clearly see wedge-shaped regions (into which the inner part of the band is divided) rotated with respect to each other so that they form, as it were, two fans proceeding from points O and O'. Clearly visible is the upper boundary of the band, stretching through the whole crystal; approximately perpendicular to this boundary are light

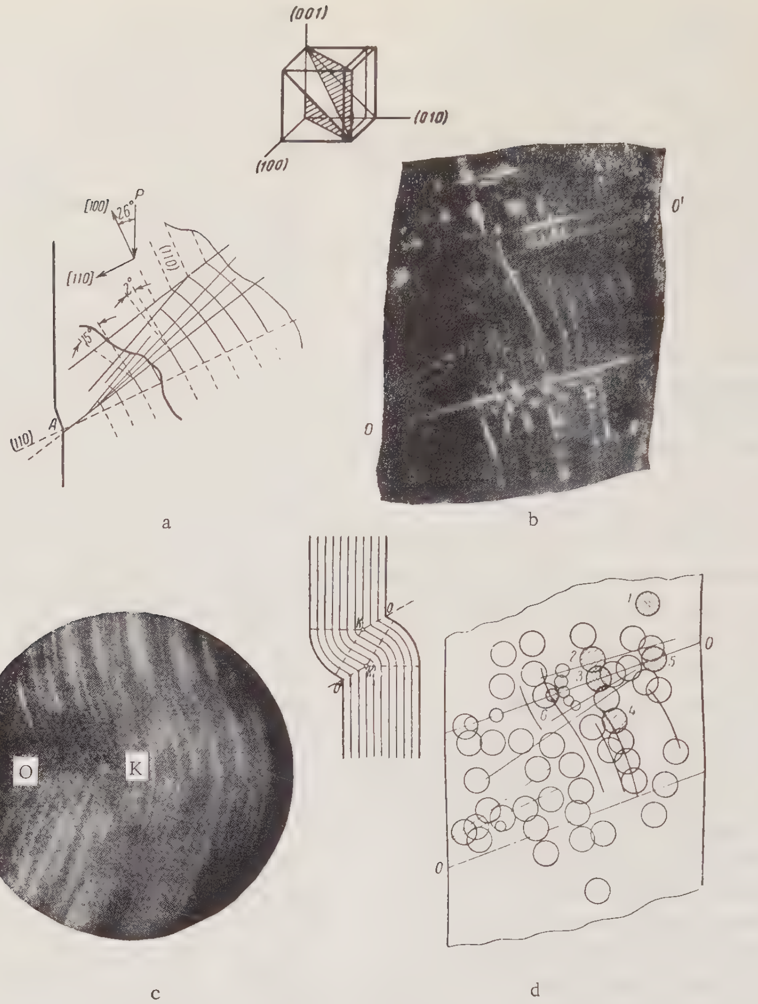

Fig. 1. Optical pictures of kink bands in crystals of thallium and cesium halides. (a) Schematic representation of a kink band observed in polarized light in a TlI−TlBr crystal. (b) CsI plate in polarized light (x 9); crystallographic orientation of plate shown above. (c) Part of a CsBr block in polarized light; on the right is a scheme of the kink bands given by Orowan. (d) Disposition of the parts examined by the Laue x-ray method in the CsI crystal (○ − diaphragm 0.5 mm; O' − diaphragm 0.2 mm). Shaded regions are the parts of the crystal, the x-ray photographs of which are given in the article.

lines passing along the sample, forming S bends inside the sample along arcs of concentric circles; these are the traces of $(1\bar{1}0)$ slip planes on the surface. Perpendicular to the $(1\bar{1}0)$ slip lines are slip lines of a second active slip system, the (011). Outside the kink band, the (011) slip lines are parallel to each other and approximately the same in intensity. Inside the kink band their intensity varies sharply: We can distinguish lines forming the boundaries of the kink band and boundaries of the wedge-shaped regions making angles of 4, 12, 16, 16, 4, and 0°, respectively, with the original directions. Hence, the orientation of the crystal is restored outside the band. At points O and O' on the surface of the crystal there are sharp grooves separating the kink band from the main crystal.

Comparison of Figs. 1a and 1b shows that, in addition to the common features typical of kink bands, the CsI and TlI−TlBr crystals also show substantial differences in band structure. In the TlI−TlBr crystals, a single slip system is active, and the boundaries of the wedge-shaped regions are therefore not slip lines. In the CsI crystal two systems are active and the boundaries of the wedge-shaped regions therefore do constitute slip lines.

Correspondingly there is also a difference in the behavior of the lines of the principal active system at the boundaries of the wedge-shaped regions.

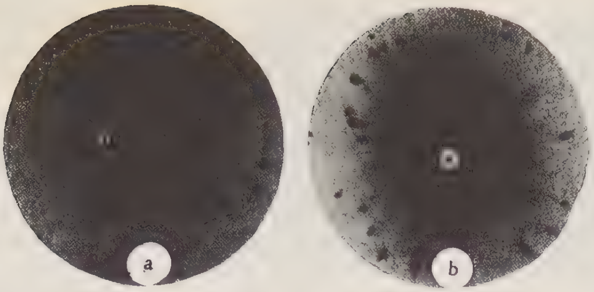

Fig. 2. X-ray photographs typical of parts of the CsI crystal at the boundary of the kink band (a) and outside the latter (b); (a) corresponds to part (2) in Fig. 1d, and (b) to part (1) in Fig. 1d.

In the CsI crystals these bend smoothly, while in the TlI – TlBr crystals the slip lines undergo a sharp break, especially marked near point A in Fig. 1a, i.e., near the channel in the surface. It is hard to follow the behavior of the slip lines of the principal system around points O and O', corresponding to channels, in the CsI sample used, since the intensity of the lines diminishes sharply in these regions. We can see, however, that the slip lines are smoothly bent on concentric circles with centers at O and O', respectively, and on the straight lines OK and O'K' there is a sharp break in the slip lines just as in the TlI – TlBr crystals in a region adjacent to the surface fracture of the crystals (Fig. 1c).

In order to compare the above optical picture with local x-ray data, the x-ray beam had to be directed at the selected portion of crystal. In order to determine the coordinates of this position, the following method was adopted. Along the boundary of the band was glued a fine glass fiber. This fiber and the side edge of the crystal were used as coordinate axes, and the distance from these to the parts selected for the photographs inside and outside the band were measured with a micrometer scale.

The crystal thus calibrated was set in the Laue camera, which was furnished with a specially constructed optical attachment and lifting mechanism, making it possible to change the position of the crystal without altering its orientation in space. With the optical attachment it was possible to establish the position at which the primary beam struck the crystal to within 10 μ. The position of this point was determined in general from the luminescence of a zinc-sulfide screen set in place of the crystal. In taking x-ray photographs of the CsI crystals, the fluorescence of the crystal itself under the x rays was used.

A detailed x-ray investigation with a narrow 40-μ diameter beam, and also beams of 0.2 and 0.5 mm, was made on the CsI crystal; since the optical picture was richer for this than for TlI – TlBr and easily seen in polarized light, the parts of the CsI crystal chosen for x-ray study are shown in Fig. 1d, which also shows the dimensions of the irradiated parts. In the TlI – TlBr crystal a beam of diameter 0.2 mm was used at the boundaries of the wedge-shaped regions, inside them, and in the region near point A; a 0.5-mm beam was used in various parts inside and outside the kink band.

The choice of regions for x-ray study was determined by the problem posed, namely: (a) to check whether the variation of the orientation of parts inside the kink bands in the CsI and TlI – TlBr crystals obeyed the general laws set out in [3], and to compare the optical and x-ray data; (b) to study how the structure of the crystal varies at smooth bends and sharp breaks of the slip lines; (c) to determine in what way the boundaries of the wedge-shaped regions differ from the insides; (d) to check whether the asterism pictures differ in the places where the slip planes emerge on the surface of the crystal (light lines in polarized light) and the dark regions adjacent to them. We see from Fig. 1d that the choice of diaphragms limiting the x-ray beam was also governed by the conditions of the problem. A series of photographs covering the whole band was obtained with a circular diaphragm 0.5 mm in diameter. For observing the "light" and "dark" regions, a circular diaphragm of diameter 0.2 mm was used, and for determining the structure inside the wedge and at the boundary regions, a slit diaphragm of 0.04 × 0.7 mm.

An x-ray diffraction pattern typical of the boundary regions of the kink band of the CsI crystal appears in Fig. 2a; Fig. 2b shows one obtained outside the band. Figure 3 shows x-ray pictures illustrating the change in the asterism on passing from the upper boundary of the band to the lower. The sharp change in the asterism in Figs. 3a and 3b, the extinction of some reflections and the appearance of new ones for a relatively small change in the rotation angle, is connected with the selective absorption of the primary radiation by the sample and the weakening of soft rays by the glass substrate, as a result of which the set of wavelengths taking part in the reflection is small. The x-ray photograph of Fig. 3c was obtained with a slit diaphragm at the wedge boundary. The photographs obtained with a slit diaphragm inside the wedge were analogous to that shown in Fig. 3c. Figure 4 shows x-ray photographs typical of those parts of the crystal adjacent to the surface fracture of the crystal.

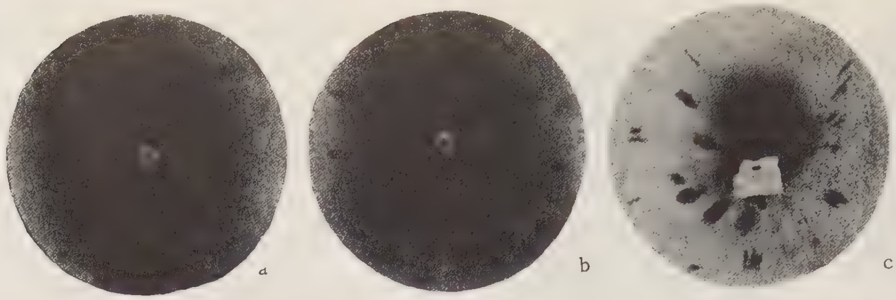

Fig. 3. X-ray photographs illustrating the change in orientation of the crystal lattice inside the kink band of the CsI crystal. (a) corresponds to part (3) in Fig. 1d, (b) to part (4) in Fig. 1d, (c) to a part of the crystal at the boundary between the second and third "wedge" in the upper part of the kink band.

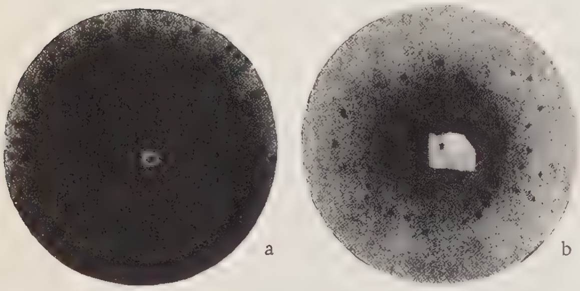

Fig. 4. X-ray photographs typical of parts adjacent to the sharply curved boundary of the crystal: (a) corresponds to region (5) in Fig. 1d (CsI), (b) to the boundary between the wedge-shaped regions in the TlI – TlBr crystal.

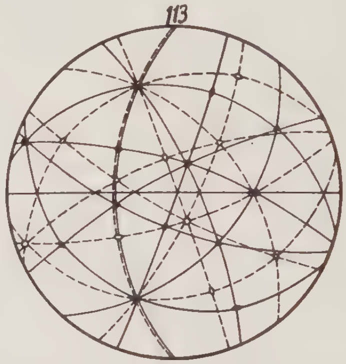

Fig. 5. Gnomostereographic projection constructed from the x-ray picture of Fig. 4a. The marks ■ indicate the original crystal, while marks □ indicate the rotated crystal. The vertical direction corresponds to the [113] direction.

By analyzing the x-ray photographs obtained with CsI, we see that:

1. Inside the kink bands there is rotation of the lattice in two opposite directions relative to the center of the band. The main direction of rotation, the [110] direction, lies in the active slip plane $(1\bar{1}0)$ perpendicular to the direction of slip [001]. The maximum rotation angle is 10 to 12°, which approximately corresponds to optical data.

By analyzing the gnomostereographic projection, it follows that, in addition to the main rotation, there is an additional rotation of the lattice around the $[01\bar{1}]$ direction. Outside the kink band the orientation of the crystal is everywhere the same.

2. Inside the kink band and in the regions close to this, the crystal is divided into individual blocks rotated with respect to each other. The block sizes differ; at the boundary of the band they are quite large (order of several microns), and inside the band they are much smaller. This indicates that the degree of lattice deformation increases from the edges of the band to the center.

3. The sharp bands disposed approximately perpendicularly to the slip lines, the boundaries of the wedge-shaped regions, do not differ in structure from the parts inside these regions. An analogous conclusion may be reached with respect to the structure of the slip bands and the intermediate parts between them.

4. In parts of the crystal adjacent to the point O, where there is a sharp change in the external form of the crystal and the greatest stresses may be expected, twin formation is observed.

In the x-ray photograph shown in Fig. 4a, we see two types of interference maxima: elongated spots from the main crystal (compare Fig. 3b) and sharp spots corresponding to a part of the crystal turned through 55° around the [110] direction relative to the main crystal.

Thus, the directions $[00\bar{1}]$ and $[11\bar{1}]$, [111] and [001], $[\bar{1}10[$ and $[\bar{1}10]$ of the main and rotated crystal coincide, and the (113) plane is common in both crystals, i.e., constitutes a twinning plane (see Fig. 5). The sharpness of the spots indicates that

in this part of the crystal the stresses are removed. The region where twinning is observed stretches inside the crystal to a distance of 1.8 mm, in good agreement with Fig. 1.

Besides these laws, we should note the extreme inhomogeneity of the internal structure of the kink band, which necessitated the large number of photographs covering the whole band (Fig. 1d).

Analysis of the x-ray pictures obtained with the TlI–TlBr crystal confirms the agreement between optical and x-ray data in estimating the rotation of the lattice inside the kink band and clearly illustrates the limited possibilities of the optical method in studying the nature of plastic-deformation phenomena. As in the CsI crystal, in the TlI–TlBr crystal the orientation of the crystal lattice inside the kink band differs from that of the original crystal by a rotation around the [110] direction. In the TlI–TlBr crystal the orientation does not change smoothly, as in CsI, but sharply on passing through the boundary separating one wedge-shaped region of the kink band from another. In the x-ray photograph obtained with a 0.2-mm beam from a part of the crystal adjacent to the boundary between the wedges, we can see a splitting of the interference spots into two spots rotated around the [110] direction relative to one another. The angles of rotation from optical and x-ray data coincide within the limits of measuring error. Thus, in the part of the crystal situated close to the considerable curvature in the crystal surface, we can observe rotation of the "wedge" as a whole through 15° and more, without rupture of continuity (see Figs. 1a and 4b), whereas, according to the data of [4], the crystal could not rotate through more than 2° without crack formation. This rotation may be described as twinning with respect to irrational planes of type (11n), since the angle of rotation varies inside the band. For a rotational angle of 15°, the (118) plane serves as a twinning plane.

Thus, the boundaries of the wedge-shaped regions, equally well observable in polarized light for TlI–TlBr and CsI crystals, are essentially different in character. As already noted, in the CsI crystal the structure of the parts along the boundary differs in no way from the internal structure of the wedges, while in the TlI–TlBr crystal, along the boundaries of the wedge-shaped regions, there is conjugation of the lattices of the two contiguous wedges in the form of "irrational" twinning.

Hence, we may assert that a sharp break in the slip lines observed inside kink bands corresponds to conjugation of the lattices by twinning without substantial internal disruption of the lattice (see Fig. 4b), while a smooth bend indicates a gradual turning of the portions of crystal accompanied by a considerable distortion of the crystal lattice.

On the basis of the foregoing data, we may draw the following conclusions:

1. The scheme of the rotation of the crystal lattice inside a kink band proposed by Orowan is evidently valid for all crystals.

2. The point of view of Barrett, Taylor, and Orowan regarding the nonparticipation of twinning in the formation and development of kink bands is not supported by our observations on the CsI crystal.

It may also be thought that phenomena well-known in the literature, kink formation, twinning with respect to irrational planes [5], "lamellation" in NaCl crystals [6], described as twinning along the (119) plane, the formation of bent regions near twinning boundaries in crystals of the hexagonal system, all these are manifestations of a combination of well-known deformation mechanisms, slip with bending and twinning in the broad sense. Which of these will be more sharply expressed, slip or twinning, depends on the orientation of the samples, their ductility, and also the local stress distribution, i.e., on the quality of the sample surfaces and the external stress field acting on the crystals.

In conclusion, we consider it our pleasant duty to thank M.V. Klassen-Neklyudova and A.A. Urusovskaya for kindly presenting the samples.

LITERATURE CITED

1. E. Orowan, "The kinking of plastic deformation in metals," Nature, 149, 643-646 (1942).
2. F.D. Rosi, "Mechanism of plastic flow in titanium," J. Metals, 6, 1, 58-69 (1954).
3. J.B. Hess and C.S. Barrett, "Structure and nature of kink bands in zinc," J. Metals, No.9, 599-606 (1949).
4. A.B. Zemtsov, M.V. Klassen-Neklyudova, and A.A. Urusovskaya, "Complex phenomena in the plastic deformation of single crystals," Dokl. Akad. Nauk SSSR, 91, No. 4 (1953).
5. N.A. Brilliantov and I.V. Obreimov, "Plastic deformation of NaCl," Žh. Éxperim. i Teor. Fiz., 5, 314, 330 (1935).
6. A.V. Štepanov and A.V. Donskoi, "New mechanism of plastic deformation of crystals," Zh. Tekhn. Fiz., 24, 2, 162-183 (1954).

STUDY OF THE INTERSECTION OF TWIN LAYERS IN CALCITE SINGLE CRYSTALS

V. I. Startsev, V. M. Kosevich, and Yu. S. Tomenko

Khar'kov Institute for the Mechanization of Agriculture, and Khar'kov Polytechnical Institute

Translated from Kristallografiya, Vol. 1, No. 4, pp. 425-428, July-August, 1956
Original article submitted March 9, 1956

The intersection of twinning layers on deformation of a calcite single crystal by a concentrated load was studied. The retardation of elastic twin layers without blocking of the residual twin layer and the development of cracks along cleavage planes when one twin layer intersects another are described.

The application of a method enabling individual twins to be followed has made it possible to elucidate the main laws governing the development and propagation of single twinning layers on plastic deformation in both ionic and metal crystals [1,2,3]. However, the development of a single twinning layer only takes place in certain conditions of loading (for calcite, in the presence of concentrated shear stresses in the twinning plane). For an arbitrarily applied load (most important practical case), there is simultaneous twinning in several systems. The number of such systems depends on the symmetry of the crystal; in calcite, bismuth, and antimony there are three, and in zinc six. In order to understand the deformation of crystals by twinning fully, we must know not only how individual twinning layers develop, but how these interact on mutual intersection.

In this paper we shall set out some results of a study on the interaction of twinning layers in calcite single crystals. Calcite is advantageously distinguished from other crystals in that, first, the interaction of twinning layers in it may be considered theoretically (see [4,5]); second, twinning in calcite may be observed in the pure form (not complicated by the occurrence of slip); and, third, the transparency of calcite makes it possible to see the three-dimensional picture.

In the experiments we used prismatic samples cut from calcite single crystals in such a way that the bases of the prism were parallel to the twinning plane (110). The samples were then polished on a cloth with chromium oxide.

The twinning experiments were carried out on several forms of Garber's apparatus. The load on the deforming blade was applied by means of a lever, one end of which was attracted by an electromagnet. Smooth variation and measurement of the load were effected by varying the current in the coils of the electromagnet. The value of the load was determined from a previously constructed calibration curve. The twinning was observed and photographed by means of a microscope set up perpendicular to the side of the sample.

In view of the fact that the construction of the apparatus did not permit twinning to be effected in two planes simultaneously, only the interaction of an elastic twin with a thin residual twin obtained earlier was studied. This primary layer had a thickness of 1-2 μ.

An elastic twin arising on application of a load, after reaching a certain critical size, rapidly increases in length (just as on passing into a residual layer [1]). However, on meeting a residual twin layer in its path it does not penetrate through it, but is held up by it. On removing the load the twin vanishes completely, no traces remaining in either the parent crystal or the residual layer. It should be noted that we have never observed the free propagation of an elastic twin of such large dimensions (length about 6 mm) in crystals of this size.

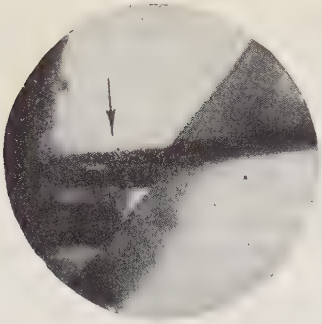

Fig. 1. Intersection of twinning layers in calcite with displacement of the elastic twinning layer (arrow) parallel to itself. × 25.

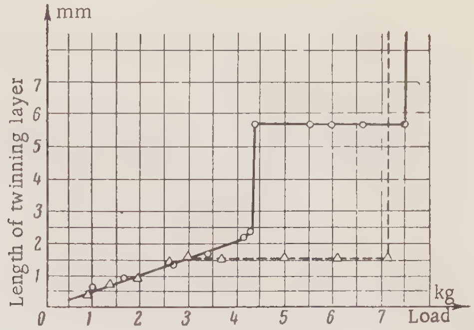

Fig. 2. Graph showing the dependence of the length of an elastic twin on the load on intersection with a stable twinning layer.

The repetition of twinning leads to the same result. If we continue to increase the load, the twin ultimately penetrates through the residual layer. This, however, does not take place at once, but only for considerable overloadings (order of 8 kg). Before this, the twin retains elastic properties at all times. After breaking through the layer, the twin simultaneously broadens. If the load is not removed rapidly after the intersection, the sample collapses.

After passing through the residual layer, the elastic twin does not remain elastic; it transforms into quite a thick stable layer which at the point of intersection appears shifted parallel to itself (Fig. 1). It is hard to explain this shift by the existence of a secondary twin in the residual layer, as occurs in metals, since the residual layer is very thin and the shift quite large.

Figure 2 shows the dependence of the length of the elastic twin on the applied load. At the onset of twinning there is the ordinary growth of a twin layer proportional to the load (continuous line on the graph). For a load of 4.3 kg (in the present experiment), the elastic twin comes up to the residual layer in one jump, but still remains elastic. Further increase of the load produces no change in the dimensions of the twin, and only at 7.55 kg does the elastic twin pass through the residual layer. If the distance between the residual layer and the face of the sample on which the concentrated load is acting is shorter than the maximum length of the elastic twin when there is no residual layer in the sample, then the sudden change in the length of the twin before contact with the stable layer does not take place. The graph for this case is shown in Fig. 2 by a broken line.

In some cases there is a more complex intersection of twinning layers. An elastic twin, after touching some point of a stable layer, stops. For some load (4.75 kg in one of the experiments), wedge-shaped petals grow from the point of contact in the direction of the cleavage plane (indicated by figures 3 and 4 in Fig. 3); these have only one point in common with the primary residual layer and intersect the secondary layer along the $[1\bar{1}0]$ line.

These petals disappear on removing the load, no traces remaining. Geometrical construction, allowing for the deformations arising (see below), leads to the conclusion that the petals are microscopic cracks capable of healing themselves on removing the load. On increasing the load further, the cracks increase their dimensions still further. For a load of 6.8 kg, the elastic twin breaks through the residual layer and itself passes into the stable state. At the same time crack 3 (Fig. 3) stops growing, and twin 5 branches out below it parallel to the elastic twin, which intersects the residual twinning layer 1 and the blocked petal 4. A qualitative ex-

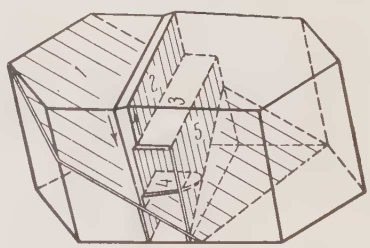

Fig. 3. Intersection of twinning layers in calcite with crack development in the cleavage plane. (1) Stable twinning layer. (2) Elastic twinning layer growing from top to bottom. (3) Crack (petal) from which twinning layer 5 proceeds downward. (4) Second wedged petal. Arrows indicate directions of displacements of atoms on twinning.

planation of the effects observed may be obtained by considering the deformation accompanying twinning.

When twinning takes place there is a rotation of the crystal lattice through a certain angle. The relative displacements of atoms lying on opposite sides of the twin layer associated with this rotation are proportional to the thickness of the layer. In the case of an elastic twin, which in the equilibrium state has a wedge-shaped form, the greatest displacements occur at the loading surface, and the step illustrated in Fig. 3 develops. At the wedge end of the elastic twin the relative displacements of the atoms are zero. When, however, the end of the elastic twin touches a stable layer, an increase in the load no longer lengthens the twin, but broadens it. This breaks up the equilibrium configuration of the elastic twinning layer. The end of the twin ceases to be wedge-shaped, and a pair of forces arises and tends to create the same step at the end as that at the surface of the crystal. This pair of forces is directed almost perpendicular to the cleavage plane, and, naturally, when it exceeds the rupture strength of the calcite along the cleavage plane, a crack results. The formation of a new twin at the end of the elastic crack may be explained as twinning under the influence of bending forces, which creates a further step, reducing the stress concentration in the crack.

We must emphasize again that in all cases the intersection of the thin residual twin by the elastic twin demands a considerable increase in external stress. This cannot be explained simply by the fact that, on creation of a new orientation in the crystal lattice in the residual twinning layer, the force is no longer applied in the twinning plane. Experiments made on twinning in calcite by a force applied at an angle to the twinning plane show that, for the development and propagation of a twinning layer, some increase in the applied force is required, but this is not large. Clearly we must remember that, in a thin stable layer, compressed by the mass of the main crystal, there cannot be a free realization of the deformations necessary for the development of a secondary twin. Moreover, it is possible that at the twin boundary there is a "faulty" lattice constituting a transitional zone between the original and twin orientations in the crystal and leading to considerable hardening.

In an earlier paper devoted to a theoretical study of elastic twinning in calcite [5], it was concluded that an elastic twin could not penetrate from one block of a crystal into another if the difference in orientation exceeded a few seconds. This conclusion is confirmed experimentally by studying twinning in mosaic crystals of sodium nitrate [6]. In the light of the experimental data presented in the present paper, it would be interesting to make a mathematical calculation of the intersection of twinning layers in calcite. This calculation could also be useful in estimating the surface energy of the cleavage plane of calcite if we analyze the process leading to the development of elastic petal cracks in the cleavage plane.

Conclusions

We have studied the intersection of an elastic twinning layer with a thin stable twinning layer in calcite. The elastic twin penetrates through the residual twin as the load increases, at the same time shifting parallel to itself. At the point where the elastic and residual twins touch, self-healing (elastic) cracks occur in the cleavage planes.

LITERATURE CITED

1. R.I. Garber, "Mechanism of the twinning of calcite and sodium nitrate on plastic deformation," Zh. Éksperim. i Teor. Fiz., 17, 47-52 (1947).
2. I.A. Gindin and V.I. Startsev, "Twinning of bismuth," Zh. Éksperim. i Teor. Fiz., 20, 738-741 (1950).
3. V.I. Startsev and V.M. Kosevich, "Elastic twinning of metals," Zh. Éksperim. i Teor. Fiz., 25, 861-864 (1955).
4. I.M. Lifshits and I.V. Obreimov, "Some considerations on the twinning of calcite," Izv. Akad. Nauk SSSR, Ser. Fiz., 12, 65-80 (1948).
5. I.M. Lifshits, "Macroscopic description of twinning phenomena in crystals," Zh. Éksperim. i Teor. Fiz., 18, 1134-1143 (1948).
6. R.I. Garber, S. Ya. Zalivadnyi, and V.I. Startsev, "Effect of mosaic structure on the resistance of sodium nitrate to mechanical twinning," Dokl. Akad. Nauk SSSR, 58, 571-572 (1947).

STUDY OF THE INTERSECTION OF TWINNING LAYERS IN SINGLE CRYSTALS OF ANTIMONY, BISMUTH, AND ZINC

V. I. Startsev, V. M. Kosevich, and Yu. S. Tomenko

Khar'kov Institute for the Mechanization of Agriculture, and Khar'kov Polytechnical Institute
Translated from Kristallografiya, Vol. 1, No. 4, pp. 429-435, July-August, 1956
Original article submitted March 9, 1956

The intersection of twinning layers in single crystals of antimony, bismuth, and zinc was studied. Various cases of the interaction of twinning layers on intersection are described. Schemes to explain the observed effects are presented. The intersection effects in the various metals are compared.

Results of a study of phenomena taking place when twinning layers intersect in a calcite single crystal were given in [1]. It is interesting to extend this work to metals in which twins form easily. In this paper we shall study the intersection of twinning layers in single crystals of antimony, bismuth, and zinc. The elastic stage of twinning in metal crystals was only found in antimony [2]. Hence, in studying bismuth and zinc, residual twinning layers were examined.

The intersection of twinning layers in the metals considered was studied in samples of dimensions 3 × 5 × 10 mm cleaved from single-crystal plates along the cleavage planes. Deformation was effected by means of a simple attachment placed on the object stand of a metallographic microscope. This consisted of clamps for the sample and blade, with a screw for smooth application of load, and enabled the sample to be bent in various planes or deformed by a concentrated load. Twinning was observed directly in the cleavage plane during deformation. It was thus possible to capture the very fine effects occurring in the intersection of twinning layers; in the ordinary metallographic method of observation these are eliminated in polishing the section [3]. The fact that one twinning layer can penetrate through another was established in [4], where the ordinary metallographic method was used, but no details of the intersection were observed.

On studying the intersection of twinning layers in metals by observing their traces on the cleavage planes, we noted the following cases of interaction.

First Case of Interaction. The growing twin layer meets another earlier-developed layer in its path. In order to create this kind of intersection, a twinning layer was first formed in one direction in the single crystal, then the position of the sample in the deforming apparatus was changed so that the load produced a twin in another direction without appreciably altering the former one.

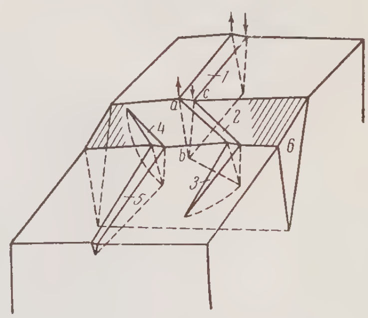

Fig. 1. Three-dimensional scheme of the most general case of interaction between twins in two different directions on intersection. The partly shaded horizontal twin developed first. The new twin propagates from top to bottom. Arrows indicate the direction of deformation on twinning.

Under these conditions. twin interaction of the kind shown in Fig. 1 occurred. While the twin layers were still not touching each other, their development took place on the ordinary basis [2]. On touching the old twinning layer 6, the new twin 1 stopped increasing its length for some time. Increasing the load at this stage simply broadened the twinning layer 1. Later, the new twin 1 was able to create a secondary twin 2 as a continuation of itself in the old twin 6. At the point where twin 2 emerged another twinning layer 3 developed and propagated in the same direction as 1. Thus, at the intersection point twin 1 suffered a break, but without losing its continuity. On further increasing the load, both the primary twins 1 and 3 and the secondary 2 continued growing. The broadening of the secondary, however, was insignificant compared with that of the primary.

This penetration of one twin through another, without breaking, by the formation of a secondary twin, is found most frequently in antimony. At the place where the layers intersect they become blocked and transform into residual twins. The elastic properties of the primary twin remain only outside the limits of the intersection. No vanishing of the secondary twin was observed.

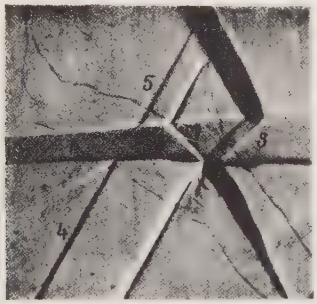

Fig. 2. Interaction of twins in zinc. View of (0001) plane. The horizontal layer 1 developed first; 2 and 3 are secondary twins; 4 and 5 represent a break intersection. × 90.

The penetration of one twin through another by way of the formation of a secondary twin is always possible in antimony when the load is large enough. In bismuth this interaction is rarely found; it usually occurs when the old twin is thinnish, of the order of 0.03 mm; in zinc it occurs still more rarely and only under special conditions; for example, on bending in a plane parallel to the plane of the old twin (Fig. 2).

In zinc, a new twin meeting an old is often only able to produce a secondary twin in the old one (Fig. 3b, part 3). On the other side of the intersection no new twin is produced even on substantially raising the load, which leads merely to a slight broadening of the secondary twin. Even more frequently in zinc, the new twin, meeting an old one on its way, stops propagating altogether, not even producing a secondary twin (Figs. 3a, b, parts 1).

The most typical kind of intersection for zinc is the break type; the new twin comes up to the old, is stopped, and then, when the load reaches a certain value, a continuation of the original twin arises on the far side of the old twin. No secondary twin is developed (Fig. 2, layers 4 and 5).

In bismuth, we also find the penetration of one twin through another without a break; increasing the load may lead subsequently to the development of secondary twins. The development of secondary twins takes place with greater difficulty, the wider the old twin. Most frequently in bismuth the interaction of the twins takes place entirely as in the scheme of Fig. 1. This scheme is realized for a small thickness (order of 0.01 mm) of the old twin. The sequence in which the twins develop may vary

a b

Fig. 3. (a) Initial stage of interaction of intersecting twins in zinc during simultaneous growth. × 90. (b) The same part of the crystal after increasing the load. × 90.

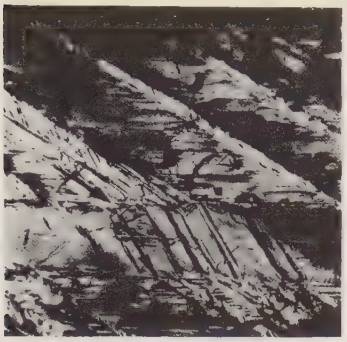

Fig. 4. Interaction of twins in the (111) plane in bismuth. The 1 is the twin developed first; the arrows show the sequence of propagation of the new twin. × 90.

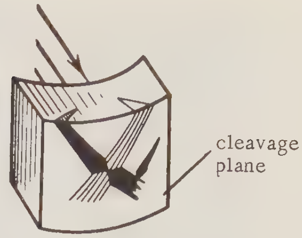

Fig. 5. Deformation of a crystal for the second case of interaction. Bending in a plane perpendicular to the cleavage plane.

considerably. For example, twin 1 (Fig. 1) may first produce twin 5, then twins 2 and 3, and then 4. It may also occur that all the twins develop almost simultaneously in one jump.

We were unable to observe interaction wholly on the scheme of Fig. 1 in zinc. In antimony such interaction occurs, but without the secondary twin 4.

We should mention that our main observations were made in certain planes [(0001) for zinc, (111) for bismuth and antimony] which were not parallel to the displacements of the atoms on twinning, i.e., for cases in which these planes intersected the twins across rather than along. We also made some experiments on metallographic sections taken from bismuth crystals along secondary cleavage planes, and also on sections taken from zinc crystals perpendicular to the cleavage planes. In both cases the twins were intersected along their length. The results were analogous to those found in the principal cleavage planes.

By way of example, we show a photograph of the interaction of twins in bismuth in the $(1\bar{1}1)$ plane leading to the formation of a secondary twin (Fig. 4). It should be noted that in these planes we only found the simplest interaction schemes.

The development of secondary twins on the intersection of primary twins may be explained as follows. When the new twin 1 (Fig. 1) comes up to the old one, at the first instant they touch at only one point; since insufficient stress is yet applied to the boundary of the primary twin, no secondary twin arises at this stage. Increasing the load and broadening the twin 1 leads to an increase in the area of contact with the layer 6. Shear stresses are thus applied to the side of the old twin, corresponding to those displacements which accompanied the development of twin 1 (shown by arrows in Fig. 1). In order that twinning should occur in layer 6, the stresses must be applied in a favorable direction. In view of the symmetry of the lattice rearrangement on twinning, the direction of the applied stresses in the case of intersecting twins coincides with the direction of twinning in the old twin. Hence it is natural that on intersection, after reaching a definite load, one twin should produce a secondary twinning layer in the second.

It is considerably more complicated to explain the rectilinear penetration of one twin through another involving a break in continuity. Here we can only express the view that the decisive role is played by the fact that the horizontal twin has a wedge-shaped form and does not pass right through the crystal. Hence, the regions situated on opposite sides of a large stable twin are parts of one and the same single crystal. This facilitates the rectilinear penetration of the twinning layer since it does not pass right through the old stable twin, but around it underneath. It may also be that the rectilinear transfer of deformation is favored by slip in the second twin; this has the required direction in zinc and bismuth.

Second Case of Interaction. The intersecting twins of two different systems develop almost simultaneously, and on increasing the load both increase their transverse dimensions. One case of loading for which this interaction is obtained appears in Fig. 5.

In zinc, the initial stage of interaction takes place rather differently from that which occurs in the first case. Thus, in Fig. 3a (section O) we can see clearly how the inclined twin bends part of the vertical twin and creates considerable distortion at the point of intersection. In Fig. 3b we see the same part of the crystal under greater load. No secondary twins developed here.

The intersection of twins in zinc presents hardly any obstacle to the broadening of each twin individually. On broadening they form a complex system, being sharply distinguished from one another.

The intersecting lines of separation at the cross-over are clearly seen in Fig. 3b (section 2). Outside the intersection region, the development of the twins continues in the usual fashion.

In bismuth, at the point of intersection, the development of twins takes place less freely and with greater crystallographic regularity. First, no bent section arises; second, all the lines of separation are distinguished by great sharpness. It is a feature of bismuth that two sections of intersecting twins giving analogous displacements may pass into one another even without any visible boundary, forming a bent but monolithic twinning layer.

In antimony mutual intersection has a sharp effect on the subsequent development of twinning layers. At the point of intersection these remain very narrow and only broaden freely at some distance away.

This difference in the nature of the intersection in the metals in question is evidently due to the fact that deformation by slip does not occur equally easily in antimony, bismuth, and zinc. In zinc the twinning process at the point of intersection of the twinning layers is supplemented by slip, which takes place quite easily in this metal. This leads to a considerable increase in the region of distortions. In antimony, slip is practically absent. At the point of intersection, displacements in different directions develop and retard one another. Since deformation can only be effected by twinning, twins do not develop in this region.

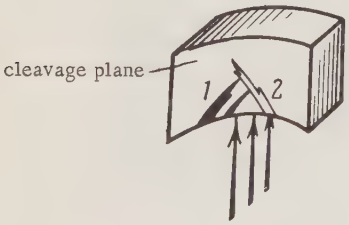

Fig. 6. Deformation scheme for the mutual intersection of twins. Bending in a plane parallel to the cleavage plane.

Third Case of Interaction. Two twinning layers begin growing simultaneously from different places and, on reaching a certain load, intersect. This takes place, for example, on bending a ductile crystal around an axis perpendicular to the cleavage plane if the orientation of the crystal allows twinning layers to develop simultaneously in two twinning systems (Fig. 6). In bismuth, in this case, twinning layers (even thin ones) block one another on meeting. In the photograph presented in Fig. 7, in the lower part of the crystal the light twin stops a series of dark ones; in the upper part of the same crystal a dark twin blocks a light one. Increasing the load leads to the development of weak secondary twins.

Fourth Case of Interaction. After intersection, one twin layer finds favorable growth conditions and the other does not.

In this case there is absorption of one twin by the other. Here an initially thin twinning layer is entirely filled up with secondary twins (Fig. 8), and then additional distortions develop, the nature of these not being susceptible to metallographic interpretation. In bismuth, with this interaction, the primary twin breaks up into individual bands. In antimony a wide twin near a narrow one breaks up into still finer parts. Absorption of a thin stable layer in antimony ends only in its being filled with secondary twins.

The absorption of the thin twin takes place most completely in zinc. Successive stages of the pro-

Fig. 7. Mutual blocking of twins in bismuth as in Fig. 6. In the lower part of the figure the light twin has stopped a series of dark twins; in the upper part a dark twin has stopped a light one. The arrows indicate secondary twins. × 90.

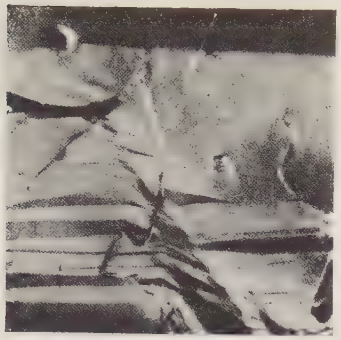

Fig. 8. Absorption of one twin by another in bismuth. The arrow marks the absorbed dark twin, in which secondary light twins are clearly visible. × 90.

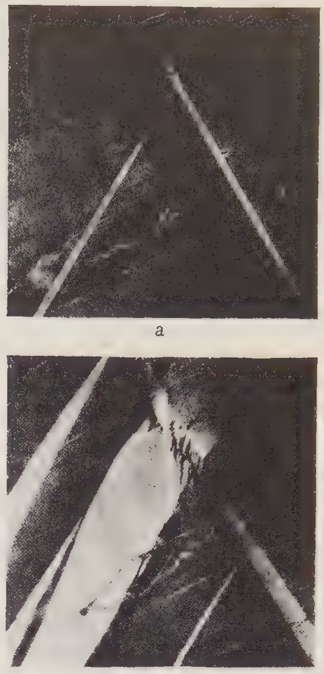

a

b

Fig. 9. Interaction of twins in zinc. (a) Initial stage. (b) Load increased; the twin for which the growth conditions are more favorable has partly absorbed the thin one. × 90.

cess are shown in Fig. 9. Figure 9a shows the initial stage of interaction, when the twin layers are similar in magnitude and when one of the interactions described in the first case occurs. Figure 9b shows the moment of twinning when, in the part overlapped by the wide twin, the narrow twin is completely filled with secondaries and further deformed, so that, in the place where it was, the surface has a hill-like relief. The wide twin is only split into parts, and hence the narrow one interferes little with its development.

Fifth Case of Interaction. Sometimes in a wide twinning layer we may find the development of secondary twins without interaction of the former with a twinning layer in another direction. The reason for these twins developing may be the creation, by some means, of stresses in the wide twin. If conditions are created for the development of the secondary twins, then, on passing to the boundary between the twinning layer and the parent crystal, they may produce an ordinary twinning layer in the main crystal. However, in such cases the secondary twin is most often stopped by the boundary and develops no further.

Discussion of Results

From the experiments here made we may conclude that in the majority of cases a residual twinning layer does not constitute an insuperable obstacle for the propagation of another twin. This fact cannot be regarded as trivial. We know that any process of plastic deformation breaking the regularity of the crystal lattice makes subsequent deformation more difficult. Twinning produces considerable changes in the structure of a single crystal. A twinning layer always has appreciable size, and the orientation in it differs from that of the main crystal by tens of degrees. The crystal is thus split into individual parts, the boundaries between which, it would seem, should block any processes of plastic deformation. It turns out, however, that one twinning layer penetrates comparatively easily through another.

It is interesting to establish an explanation for the easy intersection of twins: whether it is that, on twinning, the exclusive regularity of the crystal lattice is preserved or that, in metals, twinning by its nature is not sensitive to substantial distortions of the crystal lattice. In order to solve this problem, we may bring in data on twinning in crystals which are known to have a distorted crystal lattice (for example, deformed by slip) or in bicrystals, where the change in orientation at the surface of separation is not subject to definite crystallographic relationships, as occurs at the boundary separating a twin from the main crystal.

From published data on this subject, supplemented by our own, we arrive at the following conclusion. Twinning easily takes place after the crystal has been subjected to considerable deformation by slip. An illustration for bismuth is given in Fig. 10. It was shown in [5] that twins of zinc crystals subjected to elongation by tens of percent are no different in principle from twins obtained in unde-

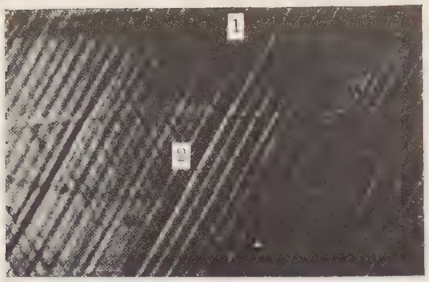

Fig. 10. Twinning after slip in bismuth. 1 and 2 are twinning layers. The break in the slip lines is connected with the fact that the twins create a certain relief on the cleavage plane. × 540.

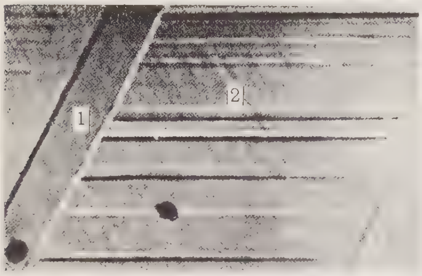

Fig. 11. Slip after twinning in bismuth. The slip bands are stopped by the twins. 1 = twinning layer; 2 = slip bands. × 540.

formed crystals. Our own observations entirely confirm this. It is well known that on slip a single crystal breaks up into a number of individual blocks, rotated with respect to each other [6]. Slip, however, does not penetrate through twinning layers (see Fig. 11).

On the twinning of bicrystals there is often penetration of the twinning layer through the boundary. We studied zinc bicrystals, the orientations of the components differing by 1 to 30°, and an antimony bicrystal with a difference of 15° in the orientation of the components. In all cases, the twinning layers penetrated through the intergrain boundaries for certain loads, increasing their transverse dimensions at the boundary. Only for a large difference between the orientations of the components was a partial narrowing of the twinning layer possible at the intergrain boundary (see Fig. 12). These data support the idea that in metals twinning has a weak effect on the distortion of the crystal lattice.

It should be noted that twinning, at room temperatures anyway, is accompanied by additional plastic effects facilitating the intersection of twins. Of the metals studied, zinc had the greatest ductility and antimony the least. At the same time, such processes as the absorption of one twin by another

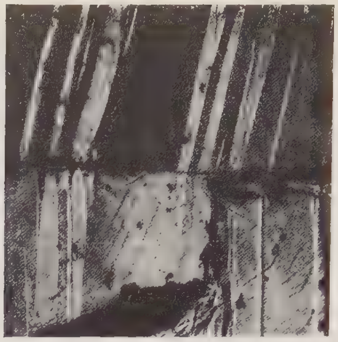

Fig. 12. Penetration of twins through the boundary of a zinc bicrystal. × 90.

take place most easily in zinc. In zinc the intersection of layers has hardly any blocking action for simultaneous expansion of the layers, while in antimony the blocking effect is great.

In view of what has been discussed, we consider the data on the intersection of twins in calcite [1] to be extremely important; in this, only cracking in the cleavage planes and twinning are observed. In calcite, the intersection of twinning layers takes place far less easily than in metals, as indicated by the need to apply heavier loading. The only process which can bring about twin intersection is cracking in the cleavage plane. Hence, on the intersection of twinning layers in calcite cracks develop in the cleavage planes; this is not found in metals. It may be expected that in metals more brittle than antimony we shall also find cracks in the cleavage planes on the intersection of twins.

More precise conclusions regarding the processes taking place on the intersection of twinning layers and regarding the disruption of the crystal lattice on twinning must await further study of these questions from both theoretical and experimental standpoints.

Conclusions

1. We have studied the intersection of twinning layers in bismuth, zinc, and antimony. We have shown that: a) twins easily penetrate through each other with or without the formation of secondary twins; b) in certain conditions the layers block each other; c) one twinning layer may absorb another.

2. We have compared the nature of the interaction between twinning layers in zinc, bismuth, and antimony.

3. We have given data on the penetration of twinning layers through slip bands and the grain boundaries, and the penetration of slip bands through a twinning layer.

LITERATURE CITED

1. V.I. Startsev, V.M. Kosevich, and Yu. S. Tomenko, "Study of the intersection of twinning layers in single crystals of calcite," Kristallografiya, 1, 4, 425-428 (1956).
2. V.I. Startsev and V.M. Kosevich, "Elastic twinning of metals," Dokl. Akad. Nauk SSSR, 101, 861-864 (1955).
3. V.I. Startsev and V.M. Kosevich, "Interaction of twins in bismuth, zinc, and antimony," Dokl. Akad. Nauk SSSR, 104, 412-414 (1955).
4. I.A. Gindin and V.I. Startsev, "Twinning of bismuth," Zh. Éxperim. i Teor. Fiz., 20, 738-741 (1950).
5. M.V. Yakutovich and É.S. Yakovleva, "Form of a mechanical twin in zinc and causes producing it," Zh. Éxperim. i Teor. Fiz., 9, 884-888 (1939).
6. N.A. Brilliantov and I.V. Obreimov, "Plastic deformation in rocksalt," Zh. Éxperim. i Teor. Fiz., 5, 830-839 (1935).

X-RAY MEASUREMENT OF COEFFICIENTS OF THERMAL EXPANSION OF POLYCRYSTALLINE MATERIALS IN THE RANGE –50 TO +100°C

V. V. Zubenko and M. M. Umanskii

M. V. Lomonosov State University, Moscow

Translated from Kristallografiya, Vol. 1, No. 4, pp. 436-441, July-August, 1956
Original article submitted September 5, 1955

A description is given of a focusing x-ray camera for precision measurement of cell parameters at –50 to +100°C for polycrystalline materials. The entire camera, including the film, is kept at a fixed temperature. The effective diameter of the film is determined from light marks applied at the working temperature. The performance of the device is illustrated by reference to the thermal expansion of aluminum and bismuth.

Thermal expansion is of considerable technical importance, especially over the range –50 to +100 °C. The x-ray method is virtually the only one for determining the true expansion coefficients (not the mean ones) for a polycrystalline material, for it measures all the unit-cell parameters (e.g., the hexagonal repeat distances a and c). These coefficients are small for most crystalline materials, so the parameters and the temperature must be measured to 0.03% or better.

Measurements at this level require patterns without pronounced line overlap, so they are possible only for cubic, tetragonal, and hexagonal materials, and then only if the cell is not too large. The distances between the lines give the cell parameters; the temperature must not vary by more than 1-2°C during the measurements.

Measurements at moderate temperatures are most readily done with the entire camera heated; ordinary cameras may then be used. The upper limit of temperature is set by fogging of the x-ray film, and we have tested several films (Agfa Laue, Agfa Duro, Russian X and XX) with this in view. There is relatively little deterioration in a dry x-ray film kept at 100°C for 2-3 h, but most films withstand 110° only for 30-40 min. Moreover, the film tends to shrink at these temperatures, mainly during the first 10-20 min. It is thus possible to use a camera at 100-110°C provided that the total time spent at that temperature is only 1-2 h. The films withstand –50 to –70° well, and this range is most easily covered with an RKF-86 (focusing) camera, which is meant for precision measurements [1], as the exposures are short.

The RKF-86 is firmly mounted in a small thermostat (the RKF-86-T camera, Fig. 1). The body of the vessel is made of asbestos board, which is readily worked and is reasonably strong. One section of the heater is mounted in the base under the bottom of the heater, being covered by an alumi-

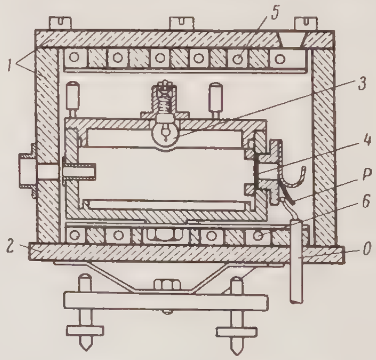

Fig. 1. Schematic section of the RKF-86-T camera: (1) demountable parts of thermostat; (2) base of thermostat, attached to RKF-86 camera; (3) lamp; (4) specimen; (5) and (6) parts of heater; (P) spring pressing on thermocouple; (O) hole for thermocouple leads.

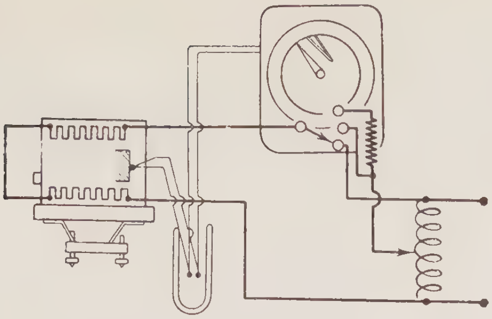

Fig. 2. Temperature-stabilization system employing an ÉPD-17 electronic potentiometer.

num plate attached to the camera. The vertical wall is formed by an asbestos tube of internal diameter 125 mm and wall thickness 12 mm. The top plate is screwed on and carries the second part of the heater; it is readily removed to allow the specimen to be changed. The temperature of the camera (specimen) is recorded by a thermocouple, which is inserted through the bottom of the thermostat and is pressed onto the brass body of the camera by a spring. The camera temperature may also be measured with a thermocouple inserted through the top plate. The thermometer is supported in a recess, which also provides good thermal contact with the camera. The film is mounted in the RKF-86 camera along the inner cylindrical surface and is pressed onto the latter by clamping strips at the ends. These strips are held by screws. The film alters in length as the camera is heated, so the ends cannot be held rigidly; a gap must be left to allow the film to be kept continuously pressed onto the body of the camera.

The temperature is stabilized as follows. The sensing element is a bimetal that controls the heater via a relay; this maintains the temperature to within 1-2°. If closer control is needed, an electronic potentiometer (Fig. 2) is used, the sensing element here being two chromel–copel thermocouples in series. The hot ends are coated with cellulose acetate to insulate them from the body of the camera. The cold ends are immersed in a Dewar containing melting ice. The relay system in this case is provided by an ÉPD-17 electronic potentiometer calibrated for platinum against platinum–rhodium. The two couples provide 14 mV per 100°C, which extends the control range to 120°C, with control to about a tenth of a degree. The recorder of the ÉPD-17 also indicates any variation in the temperature. One of the three channels is used to provide rapid initial heating, while the other two provide stabilization within set limits. The camera expands on heating, but the film contracts irreversibly. In addition, the film changes in size during

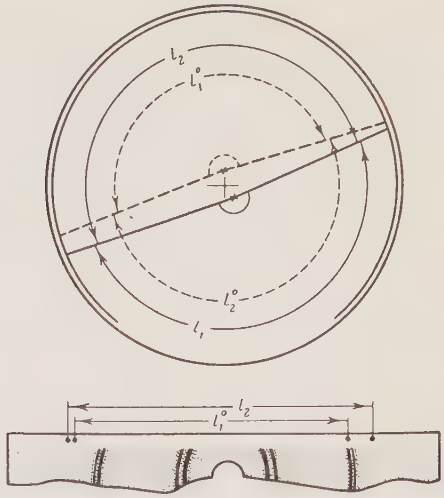

Fig. 3. Method of determining the effective diameter of the film.

processing. The effective diameter at the time of recording must be known in order to determine the reflection angles; the method previously used with the KMSP camera [2] may be employed. The edge of the top cover on the camera bears a brass cylinder that extends 5-7 mm over the film and retains it. This cylinder also contains a pea bulb and has two holes (0.5 mm each) placed along a diameter. The light from the lamp passes through these holes to produce marks corresponding to the diameter of the camera. The top cover may be turned through about 180° to produce a second pair of marks. The exposure is adjusted to give marks of contrast such as to provide very precise measurement of the position. Figure 3 shows that the distances l_1 and l_2 between the points enable one to determine the diameter of the film to about 0.02 mm. There is no need to have the lamp exactly at the axis of the camera, because the holes are exactly at the ends of a diameter and so are precisely 180° apart. The only important requirement is that the axis of this ring should coincide with the axis of the film.

The RKF-86-T records reflection angles between 60 and 88°. The distance 2S between symmetrically placed lines gives the reflection angles from

$$\vartheta = 90^\circ - 2S \cdot M, \tag{1}$$

where

$$M = \frac{57.3}{8 \cdot R} = \frac{45^\circ}{l_1 + l_2}.$$

The RKF-86-T may be used below room temperature also, because the thermostat provides good insulation; the camera and thermostat are

Substance	Temp., °C	Reflected angle	Radiation	hkl	$\alpha \cdot 10^6$
Al	$-46 - +102$	$83° - 80°23'$	Cu K_α	27	24.3 ± 1
	$+19 - +96$	$81°06' - 80°28'$	Co K_α	20	24.3 ± 1
Bi	$+20 - 92$	$85°27' - 80°40'$ $77°23' - 77°7'$	Fe K_α	$04\bar{4}2$ $31\bar{4}5$	$\alpha = 15.4 \pm 1$ $\alpha = 12.8 \pm 1$

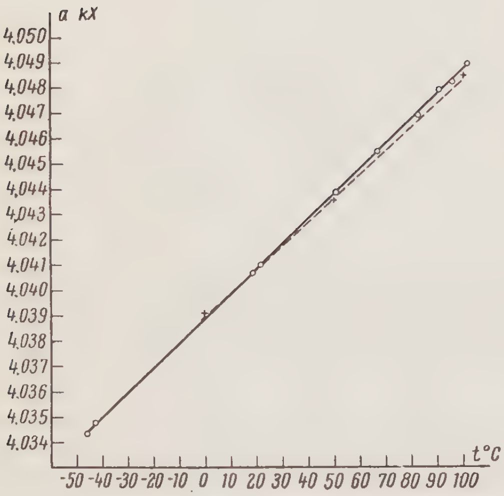

Fig. 4. Relation $a = f(t°)$ for Al (broken line from [3]).

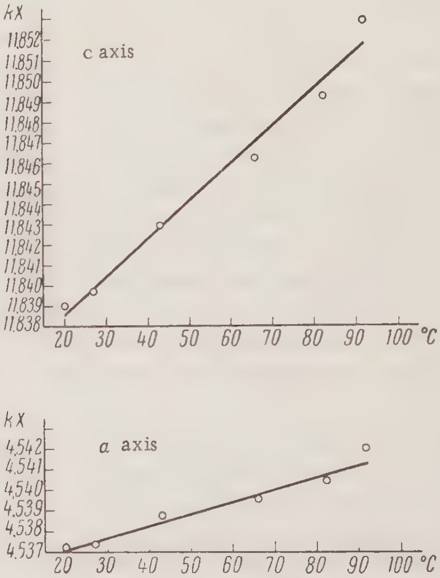

Fig. 5. Relation of a and c to temperature for Bi.

cooled to the required temperature and the subsequent rise is so slow that there is little change (only 1-2°C) during the exposure time (about 45 min). Dry ice may be placed between the walls of thermostat and camera to produce temperatures below 0°C; the thermostat may also be surrounded by dry ice. Any temperature below 0°C may be maintained for an adequate time by suitable precooling and by adjustment of the amount of dry ice. Of course, the temperature is then not so stable as when the camera is heated above room temperature.

This RKF-86-T camera has been used at various temperatures and with various radiations on aluminum and bismuth[1]; Figs. 4 and 5 give the unit-cell parameters as functions of temperature.

Both substances gave linear relations, but the values for bismuth showed rather a large spread, partly because they have to be deduced via a system of equations (the quadratic form for the hexagonal system contains a and c, as well as the reflection indices). We calculated a and c from the $04\bar{4}2$ and $31\bar{4}5$ reflections.

The coefficient of thermal expansion α is defined by

$$\alpha = \frac{a_{t_2} - a_{t_1}}{(t_2 - t_1)\, a_{t_1}}. \tag{2}$$

The error is

$$\Delta\alpha = \alpha \frac{2\Delta t}{t_2 - t_1} + \alpha \frac{\Delta a}{a} + \frac{2\Delta a}{(t_2 - t)_1\, a}, \tag{3}$$

in which Δt is the error in the temperature measurement and Δa is the error in the parameter measurement. We may express $\Delta\alpha$ with sufficient accuracy as

$$\Delta\alpha = \frac{2 \cdot \Delta a}{(t_2 - t_1)\, a}. \tag{4}$$

The table gives the results for Bi and Al.

Figure 4 shows our results for aluminum and also those given in [3]; the slight difference between the two sets may be due to difference in purity.

[1] The patterns were measured with an IZA-2 comparator; l_1 and l_2 were determined with errors not exceeding 0.05 mm, and 2S with an error not exceeding 0.1 mm.

LITERATURE CITED

1. M.M. Umanskii, "Cameras for x-ray structure analysis," In: X-Ray Methods of Examination in the Chemical Industry [in Russian] (1953).
2. S.S. Kvitka, E.V. Kolontsova, and M. M. Umanskii, Izv. Akad. Nauk SSSR, seriya fiz., 16, 372 (1952).
3. A. J.C. Wilson, Proc. Phys. Soc., 54, 487 (1942).

A SPECIALIZED GEIGER COUNTER APPARATUS FOR INTENSITY MEASUREMENT OF X-RAY REFLECTIONS

Yu. I. Graevskaya, V. I. Iveronova, and V. P. Tarasova

M. V. Lomonosov State University, Moscow
Translated from Kristallografiya, Vol. 1, No. 4, pp. 442-445, July-August, 1956
Original article submitted April 19, 1956

A description is given of a simplified apparatus for measuring the integral intensities of x-ray diffraction lines, which is based on a standard URS-55 instrument together with parts of an OSK-1 optical bench, PS-64 scalers, and RM-4 Geiger counters. The range in reflection angle ϑ is 5 to 74°. Stabilization (of voltage or current) is not used, the beam intensity being monitored by a separate counter.

Geiger counters provide rapid and accurate intensity measurement for x-ray lines.

Any ionization method differs essentially from the photographic method in that the measurements are made at isolated points and at different times, which imposes severe demands on the stability of the radiation source. Voltage and current stabilization can give an adequately constant intensity, and the standard Russian URS-55 equipment satisfies these demands, while providing a flexible means of recording the geometry and intensity distribution of an x-ray diffraction pattern. However, the geometry of the pattern is often simple and already known, in which case the only task is to measure the relative line intensities. This implies a great reduction in the requirements, because the reflection angles need not be measured very precisely; in particular, there is no need for instruments to record the intensity as a continuous function of reflection angle. An apparatus to meet these requirements is easily built up from standard units and components.

The apparatus described here is intended for the examination of lattice distortion at the atomic level in polycrystalline metals and alloys; it is based on a URS-55 bench-mounting x-ray system together with PS-64 scalers. Figure 1 shows the essential parts.

The beam from the x-ray tube is reflected by a flat monochromator crystal attached directly to the tube; the reflected beam passes through a 20-μ aluminum foil, which attenuates it somewhat. The beam falls on the specimen, which may be turned around an axis perpendicular to the beam. The pattern is recorded by a counter that may be turned around the same axis. The incident beam is monitored by means of one of the diffraction lines from the aluminum foil, which is received by a monitor counter. All other diffracted beams from the foil are blocked out by lead and aluminum stops.

This system eliminates the need for current or voltage stabilization, because a monitor counter is used in the working beam, which avoids difficulties commonly arising from wander in the focal spot, evaporation onto the tube window, alteration in the monochromator crystal, etc. All line counts are referred to some fixed number of counts recorded by the monitor.

A beam monitor is sometimes used in the beam from the other window of the x-ray tube, but only in short-term measurements [1]. This approach requires a monochromator in the second beam, because the intensity of the continuum does not vary in the same way as that of the characteristic radiation. The usual monochromator crystal does not remove the continuum entirely, because the reflected beam still contains a proportion of continuum dependent on the operating conditions of the tube and also on the setting and perfection of the monochrom-

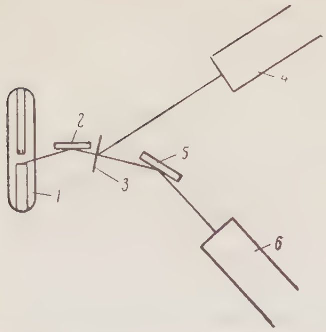

Fig. 1. The diffraction system: (1) x-ray tube; (2) monochromator crystal; (3) aluminum foil; (4) monitor counter; (5) specimen; (6) working counter.

ator crystal. It is rather difficult to obtain two identical crystals and to set them up in identical ways, the more so because the reflectivity tends to vary in time in a way dependent on the particular crystal. The best results are therefore obtained with the monitor in the working beam, but sometimes the working conditions force one to insert the monitor in the second beam, in which case it is best to insert an aluminum foil and use one of the diffraction lines, as for the working beam. This gives rather better performance in the monitor (which now receives virtually monochromatic radiation), though this is still inferior to that for the working beam.

PS-64 scalers linked to mechanical registers are used to record the counts. The working voltages at the counters are chosen from response curves recorded on the 111 line of a nickel specimen.

The monochromator is a pentaerythritol crystal, with the (002) cleavage plane used in reflection. This material was chosen on the basis of its high reflectivity and small reflecting angle (about 10°), which provides a very convenient layout of tube, crystal, and specimen, as well as reducing the time required for a single measurement to about 2 min. Table 1 [2] gives the relative reflection intensities for Cu Kα for several materials.

TABLE 1

Substance	Plane	Relative intensity
Rocksalt	200	31
Lithium fluoride	200	93
Quartz	$10\bar{1}1$	43
Aluminum	200	29
Diamond	111	120
Graphite	0002	620
Pentaerythritol	002	115

It is easy to prepare pentaerythritol crystals of quality suitable for the purpose. Our system operates satisfactorily with a crystal about 5 × 3 mm and 0.5-1 mm thick. Single crystals of size large enough to yield such plates (or somewhat larger ones) may be grown at a variety of temperatures from several solvents including water. Good crystals will grow spontaneously on slow cooling of aqueous HCl (1 part concentrated acid, 18 parts H_2O) saturated at 20-30°C above room temperature; but better ones are obtained by inserting single crystals as seeds attached to glass fibers with mineral wax. Only completely transparent crystals should be used as monochromators, for these give strong sharp reflections and reproducible reflectivity. The compound does have the disadvantage of a certain susceptibility to attack by atmospheric water vapor, so it is best to coat the crystals with some impermeable lacquer, e.g., nitrocellulose dissolved in a mixture of amyl acetate with acetone. This does not provide perfect protection, but the crystal remains serviceable for over 1 year.

The crystal may be mounted in a special holder [3], which is attached directly to the metal case of the URS-55 tube; it contains a rectangular metal plate having holes to pass the incident and reflected beams, the latter going to a cylindrical collimator. The tube is set to pass the reflected beam along a diameter of an OKS-1 circular optical bench, which carries an RM-4 counter. The specimen holder lies at the center of this circle, and its angle of rotation is read from a scale graduated in degrees. The crystal is set 12 cm from the plane of the specimen, which is at the same distance from the slit on the counter. The angular position of the counter is read on a second scale. The working range in the reflection angle ϑ is 5 to 74°.

The specimen is set to the appropriate ϑ (relative to the undeviated beam), while the counter is set at an angle close to 2ϑ. A range of about 3° covering the diffraction line is scanned, with measurements at steps of 0.5°. The slit width is set at 4 mm, which corresponds to about 2° of arc, or 3-4 times the normal width of a line at the working distance. The line intensity can be measured with the counter in a fixed position in this way; the counter need be moved only in order to determine the exact position corresponding to 2ϑ, at which the count rate is maximal. Similarly, the specimen may be set to the optimal position (that giving minimum absorption factor) corresponding to the angle ϑ between the surface of the specimen and the primary beam.

The reproducibility has been tested with a flat specimen of unannealed nickel powder (111, 113,

and 133 lines). The line intensities were constant to 4%, while the ratios of 111 to 113 and of 111 to 133 were constant to 3-4%. This test was performed by setting up the specimen and counter afresh each time. In addition, tests were done without moving counter or specimen; here, the spread was about 1.5%, which is very nearly the random error of measurement, because about 11,000 counts were recorded in each measurement. The main source of variation is thus due to difficulty in resetting the specimen and counter exactly. The limit of detection was examined with rocksalt powder, which was found to give measurable intensities for all lines that can be recorded with copper radiation, including ones, such as 311 and 331, whose ratios to the strongest line, namely 200, are, respectively, 2:100 and 1:100 [4].

The line intensities are always referred to the simultaneous readings on the monitor; the reading N_1 given by the working counter is normalized via the factor $5000/N_2$, in which N_2 is the number of counts recorded by the monitor, whose nominal count rate is 5000 per minute. The normalized result N is

$$N = N_1 \frac{5000}{N_2}.$$

We are indebted to our assistant N. E. Kravchenko for his careful work on some of these tests.

LITERATURE CITED

1. E. Gillam and D. J. Cole, "On monitoring a Geiger-counter spectrometer beam," J. Sci. Instr., 30, 429-430 (1953).
2. R. Renninger, "Absolut-Vergleich der stärksten Röntgenreflexe Verschiedener Kristalle," Acta Cryst., 7, 677 (1954).
3. S. S. Kvitka, "A planar monochromator for the BSV-4 tube," Kristallografiya, 1, 4, 485-487 (1956).
4. M. E. Swanson and R. K. Fuyat, "Standard x-ray diffraction powder patterns," Nat. Bur. Std. Circular 539, II 41-43 (1953).

METHODS OF X-RAY GONIOMETRY FOR EXAMINING CRYSTALS*

M. M. Umanskii and D. M. Kheiker

M.V. Lomonosov State University, Moscow, and
All-Union Asbestos Cement Research Institute
Translated from Kristallografiya, Vol. 1, No. 4,
pp. 446-459, July-August, 1956
Original article submitted September 9, 1955

Photographic and ionization methods are compared. It is shown that photographic methods are convenient for layerwise examination of the reciprocal lattice, while ionization methods are convenient for sequential examination of nodes. The various types of diffractometer are compared, as are the appropriate areas of use for the various methods of x-ray goniometry. A method is described for recording the entire possible interference field with a URS-50I fitted with a modified GUR-3 to convert the former to a diffractometer for single crystals.

The most important of the problems that can be solved by x-ray goniometry are as follows: (1) determination of the type, shape, and size of the unit cell; (2) determination of laws of absence, and hence the x-ray group; and, (3) determination of F_{hkl} (structure amplitudes). Other methods can be used for the first; the second requires examination of certain types of interference only, and does not make it essential to record all the diffraction pattern; and the third is the special area of x-ray goniometry which requires detection of all interferences that are reasonably possible, or at least all of those with small reciprocal-lattice vectors H. The most important aspect at present is to find the optimal solution to the last problem.

Photographic methods were long the only ones in this area [1-3], but recent advances in ionization methods have given rise to goniometers equipped with counters, which are often called diffractometers [4-7].

A photographic film consists of a vast number of point detectors that can store radiation effects; this enables a film to record the entire pattern (or much of it) simultaneously.

A counter records the different points at different times; it is a detector of very high sensitivity, but it can handle only one point at a time, and this demands very high stability in the primary beam. In addition, the method of recording has to be altered; it is undesirable to measure the pattern in the ways used with films. The methods could be the same if one could use a mosaic of counters with its entire (large) surface area sensitive to the x rays.

A major advantage of the diffractometer is the very high sensitivity in conjunction with the simultaneous recording of position and intensity in the peak; in addition, the intensity readings are usually more precise.

Here we review the various methods used in x-ray goniometry and consider the areas in which each may be used to best effect.

Relations Between Methods of Representing the Reciprocal Lattice

The main and specific problem in goniometry is intensity measurement on all possible reflections (determination of the weights of the reciprocal-lattice nodes). A given node is characterized by a vector **H**, which may be specified in terms of the indices of the node and the coordinate vectors **a***, **b***, and **c***:

$$\mathbf{H}_{hkl} = h\mathbf{a}^* + k\mathbf{b}^* + l\mathbf{c}^*. \quad (1)$$

*Read June 24, 1955, at the Fifth All-Union Conference on the Application of X-Rays to the Examination of Materials.

The reciprocal lattice may be considered as a series of layers, as a family of parallel net planes composed of regularly placed nodes, or as a family of parallel straight lines also regularly built up from nodes. It is valueless to consider the reciprocal lattice as a set of nodes without relationships.

The reciprocal lattice taken as a system of layers may be represented in cylindrical coordinates, i.e., **H** may be expressed in terms of its three components: ξ, the projection of **H** on the plane of the layer; ζ, the projection of **H** on an axis perpendicular to the plane of the layer; and φ, the angle between the coordinate axis (reference direction in the plane of the layer) and the direction of ξ.

The parallel-line representation makes it convenient to consider the lattice in an orthogonal coordinate system having axes η, ε, and ζ; axis ε coincides with the reference straight line of the family (it is natural to take ε as lying along one of the coordinate axes in the reciprocal lattice, say b^*), axis η is perpendicular to ε in a coordinate plane of the reciprocal lattice (say, a^*b^*), and axis ζ is normal to ε and η, and hence to the a^*b^* plane. A given node is thus represented in one case by components of **H**, namely, ξ, ζ, and φ, and in the other case by the coordinates η, ε, and ζ. All nodes in the plane of the n-th layer in both cases correspond to the same ζ. The relations of ζ, ξ, φ to η, ε, ζ are:

$$\left.\begin{array}{l} \varepsilon^2 + \eta^2 + \zeta^2 = H^2, \\ \varepsilon^2 + \eta^2 = \xi^2, \\ \eta = \xi \cdot \tan\varphi \end{array}\right\}. \tag{2}$$

It is very common to represent the reciprocal lattice as a system of parallel layers in ζ, ξ, φ coordinates, on account of the common use of layer-line patterns, which may be considered as photographs of the planes. Several books [1-3] deal in detail with this representation and with the relations of ζ, ξ, φ, hkl and $\mathbf{a}^*$, $\mathbf{b}^*$, $\mathbf{c}^*$. The parallel-line representation in terms of ε, η, ζ is logical in diffractometer work, where the nodes are measured in sequence, e.g., all the nodes in one series, then all those in another, etc.

We may relate ε, η, ζ to hkl and to $\mathbf{a}^*$, $\mathbf{b}^*$, $\mathbf{c}^*$ as follows for the cubic system. The unit cell of any other system may be considered as a distorted cubic cell, and the conversion may be made via the coefficients for the deviation [8], which are expressed in terms of the cell parameters. The relation of $\varepsilon\eta\zeta$ to hkl and $\mathbf{a}^*$ for the cubic system may be used with the appropriate conversion coefficients to find the relation for any other system, e.g.,

Orthorhombic

$$\varepsilon = k/b,\ \eta = h/a,\ \zeta = l/c,$$

or

$$\varepsilon = kb^*,\ \eta = ha^*,\ \zeta = lc^*. \tag{3}$$

Triclinic

$$\varepsilon = \frac{h \operatorname{tg}\Delta}{a \sin\beta} + \frac{k}{b \sin\alpha \cos\Delta} - \frac{l}{c}\left(\operatorname{ctg}\beta \operatorname{tg}\Delta + \frac{\operatorname{ctg}\alpha}{\cos\Delta}\right),$$

$$\eta = \frac{h}{a \sin\beta} - \frac{l}{c}\operatorname{ctg}\beta,$$

$$\zeta = \frac{l}{c},$$

where $\sin\Delta = \dfrac{\cos\gamma - \cos\alpha\cos\beta}{\sin\alpha\sin\beta}$.

$$\varepsilon = kb^* - ha^*\cos\gamma^*$$

$$+ lc^*\left(\sin\alpha^* \operatorname{ctg}\gamma^* \cos\Delta^* - \frac{\sqrt{\sin^2\beta^* - \sin^2\alpha^* \sin^2\Delta^*}}{\sin\gamma^*}\right),$$

$$\eta = ha^*\sin\gamma^* - lc^*\cos\Delta^*\sin\alpha^*,$$

$$\zeta = lc^*\sin\alpha^*\sin\Delta^*,$$

where $\cos\Delta^* = \dfrac{\cos\alpha^*\cos\gamma^* - \cos\beta^*}{\sin\alpha^*\sin\gamma^*}$.

Geometric Relations in Layerwise Recording

This recording is specific to photographic methods; photographic goniometer patterns are always representations of reciprocal-lattice planes. The common Weissenberg patterns are simply distorted images of these planes, and various graphical and other methods have been devised for converting this to undistorted ones. In addition, methods have been developed for obtaining undistorted images directly, in which case the goniometer goes some way in elucidating the pattern instead of merely recording it. The photographic methods are common knowledge; layerwise recording is possible also with counters.

The following are the geometrical principles of such recording. We assume that the crystal can rotate around an axis perpendicular to the a^*b^* plane, and the nodes are assumed to lie on straight lines parallel to the b^* axis. The initial position of the crystal is taken to be such that the b^* axis is perpendicular to the plane containing the primary beam and the axis of rotation. Let μ be the angle between the primary beam and the reciprocal-lattice plane, with ν the angle between that plane and the reflected beam.

We need: (a) the relation of μ and ν to ζ, the height of the layer of the reciprocal-lattice plane under examination; (b) the relation of the rotation angle ω of the crystal to the coordinates (η, ε, ζ) of the node in the recording position; (c) the relation of the azimuthal angle Υ of the reflected beam to (η, ε, ζ); and, (d) the relation between Υ and ω.

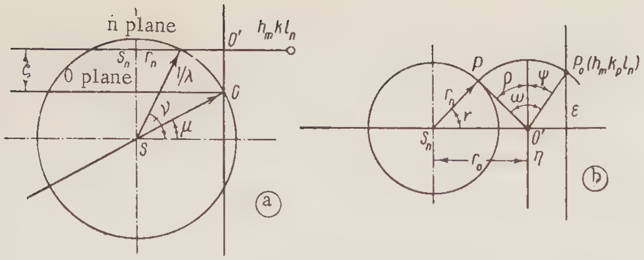

Fig. 1. Reciprocal lattice and reflection sphere for the general case $\mu \neq \nu$; (s) center of reflection sphere; (s_n) and (r_n) center and radius of reflection circle (section of the sphere by plane n); (O) zero node of reciprocal lattice; (O') point where rotation axis meets plane n; ($h_m k l_n$) nodal line in reciprocal lattice; (P_0) node on line $h_m k l_n$; (P) node P_0 after rotation through ω; (ρ) and (ψ) accessory angles; (Υ) angle between planes of primary and reflected beams; ($\varepsilon, \eta, \xi, \zeta$) coordinates of node; (a) plane of primary beam and principal axis; (b) plane n.

We consider three cases: (1) the general case of any μ and ν; (2) primary beam perpendicular to rotation axis, $\mu = 0$; and (3) $\mu = -\nu$ (equal-inclination case).

1. General case (Fig. 1):

$$\left.\begin{aligned}
&\sin\nu - \sin\mu = \zeta\lambda,\\
&\omega = \rho + \psi,\\
&\sin\rho = \frac{\cos\mu - \cos\nu\cos\Upsilon}{\xi\lambda} = \frac{\cos^2\mu - \cos^2\nu + \xi^2\lambda^2}{2\xi\lambda\cos\mu},\\
&\tan\psi = \frac{\eta}{\varepsilon},\\
&\cos\Upsilon = \frac{\cos^2\nu + \cos^2\mu - \xi^2\lambda^2}{2\cos\nu\cos\mu},\\
&\Upsilon = \omega \pm \arccos\left(\frac{\cos\mu\cos\omega + \eta\lambda}{\cos\nu}\right).
\end{aligned}\right\} \quad (4)$$

2. Perpendicular beam, $\mu = 0$ (Fig. 2):

$$\left.\begin{aligned}
&\sin\nu = \zeta\lambda,\\
&\omega = \rho + \psi,\\
&\sin\rho = \frac{1 - \cos\nu\cos\Upsilon}{\xi\lambda} = \frac{\zeta^2 + \xi^2}{2\xi}\lambda,\\
&\tan\psi = \frac{\eta}{\varepsilon},\\
&\cos\Upsilon = \frac{2 - \zeta^2\lambda^2 - \xi^2\lambda^2}{2\sqrt{1 - \zeta^2\lambda^2}},\\
&\Upsilon = \omega + \arccos\frac{\cos\omega + \eta\lambda}{\sqrt{1 - \zeta^2\lambda^2}}.
\end{aligned}\right\} \quad (5)$$

3. Equal-inclination case, $\mu = -\nu$ (Fig. 3):

$$\left.\begin{aligned}
&\sin\nu = \frac{\zeta\lambda}{2},\\
&\omega = \rho + \psi,\\
&\rho = \frac{\Upsilon}{2},\\
&\tan\psi = \frac{\eta}{\varepsilon},
\end{aligned}\right\} \quad (6)$$

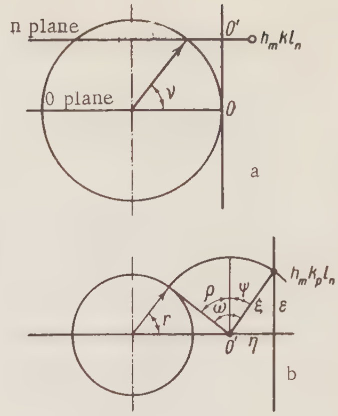

Fig. 2. Reciprocal lattice and reflection sphere for the perpendicular-beam case ($\mu = 0$); symbols analogous to those of Fig. 1.

$$\left.\begin{aligned}
&\sin\frac{\Upsilon}{2} = \frac{\xi\lambda}{\sqrt{4 - \zeta^2\lambda^2}},\\
&\cos\gamma = \frac{2 - \frac{\zeta^2\lambda^2}{2} - \xi^2\lambda^2}{2 - \frac{\zeta^2\lambda^2}{2}},\\
&\Upsilon = \omega \pm \arccos\left(\cos\omega + \frac{\eta\lambda}{\sqrt{1 - \frac{\zeta^2\lambda^2}{4}}}\right).
\end{aligned}\right\} \quad (6)$$

The choice of μ or ν (but not both) is arbitrary for the general case; in particular, cases μ and ν are uniquely determined by ζ, so the coordinates of the node determine all setting angles of crystal and counter (which lies along the reflected beam), namely μ, ν, ω, Υ. We have the very simple relation $\Upsilon = 2\omega$ for the central line ($\eta = 0$) of any

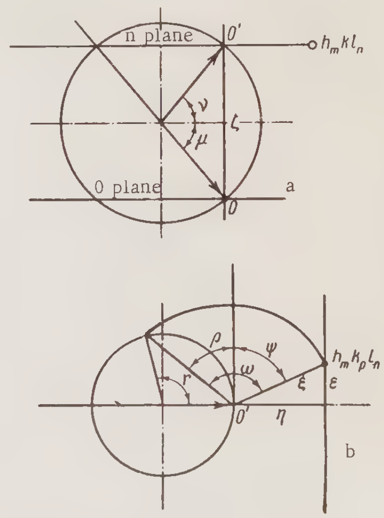

Fig. 3. Reciprocal lattice and reflection sphere for the equal-inclination case ($\mu = -\nu$); symbols analogous to those of Fig. 1.

plane (arbitrary ζ) for the equal-inclination case; this provides a simple means of coupling the rotation of the counter to that of the crystal.

Geometrical Relations in Linewise Recording

Counter measurements are best made on nodes lying on straight lines in the reciprocal lattice, with subsequent transfer between such lines [9]. The design of the diffractometer makes it convenient to have the incident and reflected beams in a plane perpendicular to the rotation axis ($\mu = 0$, $\nu = 0$). A crystal setting giving these lines (the densely populated ones, say, parallel to axis b*) perpendicular to the principal rotation axis of the crystal allows one to bring any nodal line (family b*) into the equatorial plane by rotation of the crystal around an additional axis parallel to this family of lines,[1] and to record the nodes lying in it, as for the usual recording of the nodes in the zero plane (Fig. 4). The reflected rays then always lie only in the equatorial plane, so we may call this the equatorial method. The nodes on line $h_m k l_n$ may be brought in turn into the recording position by rotation around the principal axis (also the rotation axis for the counter) after that line has been brought into the equatorial plane by rotation through γ around the additional axis. It is convenient to have the nodal lines (and hence also the additional axis) perpendicular to the primary beam in the initial position. The crystal setting required to produce the reflecting position is defined by $\omega = \rho + \psi$, while that of the counter is defined by Υ. These angles vary for the nodes in a single line.

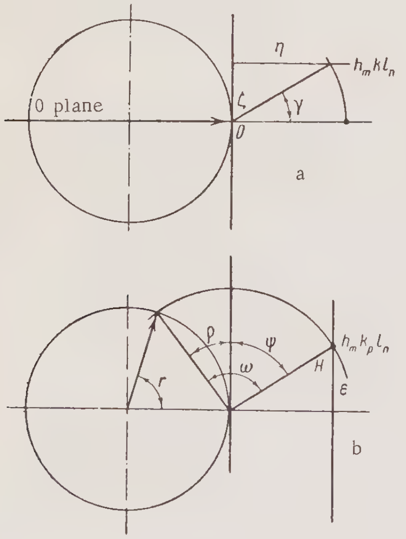

Fig. 4. Reciprocal lattice and reflection sphere for the equatorial method; symbols analogous to those of Fig. 1. Here, γ is the angle of rotation of the $h_m k l_n$ nodal line in the equatorial plane.

The relationships for the setting angles of the crystals in the equatorial method are

$$\begin{aligned} \tan\gamma &= \zeta/\eta, \\ \omega &= \rho + \psi, \\ \sin\rho &= \frac{H\lambda}{2}, \\ \tan\psi &= \frac{\sqrt{\zeta^2+\eta^2}}{\varepsilon}, \\ \Upsilon &= 2\rho. \end{aligned} \tag{7}$$

The relation of Υ to ω is given by

$$\Upsilon = \omega \pm \arccos\left(\cos\omega + \lambda\sqrt{\zeta^2+\eta^2}\right). \tag{7'}$$

There are various ways of recording the nodes in plane n when this is set in the equal-inclination position. All nodes in this plane are considered as lying on $h_m k l_n$ nodal lines, and all the nodes in the plane may thus be recorded in sequence (Fig. 3). In this case the node is brought into the recording position by setting μ and ν (which are the same for all these nodes), with additional rotations of the crystal and counter about a common axis, the principal axis of the goniometer.[2]

The crystal setting is defined by $\omega = \rho + \psi$, while that of the counter is defined by Υ. These angles vary for the nodes in a single line, as is shown by (7).

We may also consider the nodes as lying on central straight lines (lines through the rotation axis of the plane) instead of on the natural $h_m k l_n$ lines. We then have the simple relation $\Upsilon = 2\omega$, which allows simple mechanical coupling of crystal and counter. The start and the precise coupling of the motions must be set for each line individually.

The tangential method (Fig. 5) is a further possibility. We have seen that the use of central lines

[1] There are other possible ways of rotating the crystal around the additional axis to bring the desired node into the equatorial plane, but in every case the primary and reflected beams will lie in that plane.

[2] It is possible to incline the axis of the goniometer at an angle ν to the primary beam, and the counter at 2ν, instead of inclining the primary beam.

simplifies the relation between the counter and crystal angles (provides a simple mechanical linkage). Rotation around the additional axis (by analogy with the equatorial case) allows one to bring the nodal line into the equal-inclination position in the vertical plane perpendicular to the beam through the common axis of crystal and counter. If now the primary beam is inclined at an angle μ, with the counter at $\nu = -\mu$, the nodes on any line chosen at random may be recorded as for the central lines in the equal-inclination method. The tangential method has μ and ν constant only for a given line, not for the whole plane. The crystal must be turned through an angle $\omega = \rho$, and the counter through $\Upsilon = 2\omega$, when the line has been set in the equal-inclination position. A simple mechanical coupling is possible here also.

Here, the relationships for the setting angles of the crystals are

$$\left.\begin{aligned} \tan \bar{\gamma} &= \eta/\zeta, \\ \sin \mu &= \frac{\lambda}{2}\sqrt{\eta^2 + \zeta^2}, \\ \omega &= \rho, \\ \sin \rho &= \frac{\varepsilon\lambda}{2\cos\nu}, \\ \Upsilon &= 2\rho. \end{aligned}\right\} \tag{8}$$

Again we have the simple relation $\Upsilon = 2\omega$.

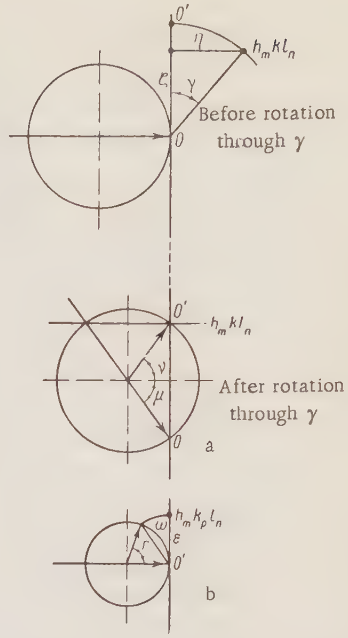

Fig. 5. Reciprocal lattice and reflection sphere for the tangential method; symbols analogous to those of Fig. 1. Here, γ is the angle of rotation of the nodal line in the equal-inclination position.

Comparison of Layerwise and Linewise Methods

All layerwise methods are based on division of the entire reciprocal lattice into hkl_n layer planes; photographic methods require only a knowledge of ζ in order to obtain the reflections corresponding to all the nodes in a given plane. The diffracted rays, no matter what Υ may be, will meet the film. The relation of Υ to ω must be known; the indices of the reflections are found by indexing the pattern: an undistorted image of the reciprocal-lattice plane (as from the cameras of [10, 11]) allows one to find the indices automatically. Photographic recording thus merely requires setting of μ and ν, which is done for each plane, while all nodes in the plane are recorded automatically.

Counter methods require the reflected ray to coincide with the axis of the counter, so ω and Υ must be properly related. The precise relation between these is dependent on the coordinates of the node as well as on the height of the layer; crystal and counter must be set separately for each node. All layerwise methods, except the equal-inclination one, have blind regions arising from the particular features of the method of recording, not from constructional details of the instrument. Linewise recording is the best approach for counter methods, and the techniques considered above leave no blind regions. Any restrictions are due solely to the design of the instrument; good design leads to minimal loss. A single nodal line is brought into the recording position (not an entire plane) in linewise recording; the coordinates (ζ, η) must be known for this purpose. The motion of the counter can sometimes then be coupled to that of the crystal to provide automatic recording of all nodes on the line without prior calculation of the positions. This restricted form of automatic working is probably of little value when the crystal rotates at a fixed speed, because much of the time is wasted on measuring the background. A line may contain (say) 10 nodes, and the intensity corresponding to a node may be measured over a range of 0.5°; then the full 180° rotation of the crystal is employed only to the extent of about 3% (0.5 × 10), whereas the useful interval of rotation for photographic recording under analogous conditions is 30% (10 × 10 × 0.5). The best method of linewise recording is probably not to be sought in fully automatic working, but rather in maximal simplification in the setting of μ, ν, ω, and Υ together with automatic computation of the setting

TABLE 1. Numbers of Settings for Crystal and Counter to Cover Entire Pattern in Various Sequential Recording Methods

Method	Equal-inclination	Equatorial	Tangential
Parameters	$\mu = -\nu,\ \omega,\ \Upsilon$	$\gamma,\ \omega,\ \Upsilon$	$\bar{\gamma},\ \mu,\ \nu,\ \Upsilon = 2\omega$
Relation of Υ to ω	$\Upsilon = \omega \pm \arccos\left(\cos\omega + \frac{\eta\lambda}{\sqrt{1-\frac{\zeta^2\lambda^2}{4}}}\right)$	$\Upsilon = \omega \pm \arccos(\cos\omega + \lambda\sqrt{\zeta^2+\eta^2})$	$\Upsilon = 2\omega$
Photographic	$2n$	not used	not used
Counter, individual setting	$2(n^3+n)$	$2n^3+n^2$	n^3+3n^2
Counter, automatic setting	$2(n^2+n)$	$3n^2$	$3n^2$
No. of adjustments to coupling	n^2	n^2	1

angles from the hk$l$ in conjunction with the parameters of the crystal.

The mode of recording determines the number of settings needed in linewise techniques. We replace the reflection sphere by a cube for this purpose, and assume it to contain n^3 nodes to be recorded (in planes each having n nodal lines, each with n nodes). The table gives the number of settings needed.

Equal-Inclination Method. The four angles μ, γ, ω, and Υ must be set for each node with a counter; there is no simple relation of Υ to ω, but μ and ν are constant for a given n plane. There are thus 2n common settings for the n layers, and also two settings (ω and Υ) for each of the n^3 nodes. The total is

$$N = 2n^3 + 2n.$$

Then, N = 2020 for n = 10.

Photographic recording requires μ and ν to be set for n planes; N = 2n, so N = 20 for n = 10.

Equatorial Method. Angles γ, ω, and Υ must be known for each node; γ is constant for an entire nodal line. The total is

$$N = 2n^3 + n^2.$$

Then, N = 2100 for n = 10.

Tangential Method. The quantities here for each node are $\bar{\gamma}$, μ, ν, ω, and Υ, but the last two have the simple relation $\Upsilon = 2\omega$, which is easy to set up in a mechanism; only four settings are needed, of which γ, ν, and μ are fixed for a given nodal line. The total is

$$N = n^3 + 3n^2.$$

Then, N = 1300 for n = 10.

The $\Upsilon = 2\omega$ relation allows automatic recording along nodal lines; the only setting needed is to bring each such line to the recording position, so N = $3n^2$, and N = 300 for n = 10.

Blind regions arising from the geometry of the method occur in some layerwise methods (perpendicular beam, constant cone, and plane cone, the last being a particular case of the second). Also, all these methods involve design restrictions, because a given design allows only certain combinations of ranges in μ, ν, ω, and Υ.

The various forms of linewise recording show that the equal-inclination and tangential techniques are the promising ones as regards the design of an automatic instrument with continuous counter recording. A diffractometer based on the equatorial method with individual node setting would be the least complex in design.

Adaptation of the URS-50I for Complete Examination of Single Crystals

The GUR-3 goniometer in the URS-50I provides for independent rotation of the counter and the stage (which carries the crystal) around their common axis. The stage can be turned through 360°; the counter, to any angle in the range –130 to +150°. The

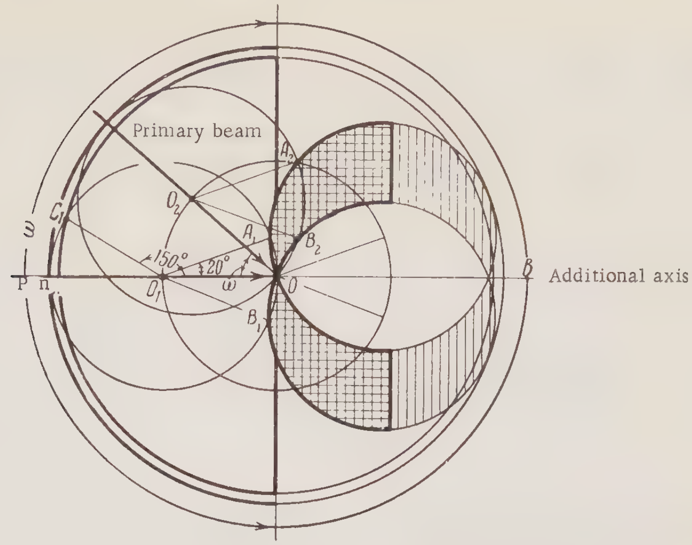

Fig. 6. The available region of the equatorial reflection circle in the GUR-3 as adapted for equatorial examination of single crystals. The heavy line indicates the usable region corresponding to the range in ω denoted by the arrows. The dead zone is shown with cross-hatching; this corresponds to the same range in ω. The single hatching denotes the rest of the dead zone. The other lines serve to construct the available region [$A_1O_1B_1$ = $A_2O_2B_2$ = 40° represents forbidden ranges in Υ due to the scale for reading γ, Υ_{max} = OO_1C = 150°].

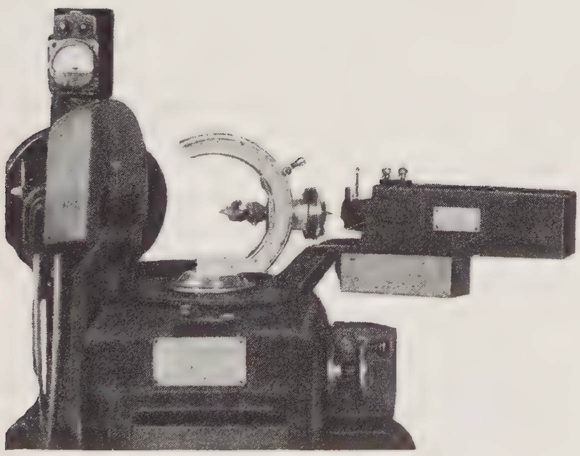

Fig. 7. The GUR-3 fitted for examination of single crystals.

collimator for the primary beam is perpendicular to that axis. The GUR-3 allows the use of a perpendicular beam to measure the intensities of all reflections in the zero plane. The stage of the GUR-3 may be fitted with a device to turn the crystal around an axis perpendicular to the axis of the stage; this converts the URS-50I to a diffractometer capable of operating in the equatorial mode to record linewise all the reflections from a single crystal. Figure 7 shows the URS-50I fitted with this. The scale that reads the angle of rotation around this additional axis (the angle that brings the nodal line into the equatorial plane) gives rise to blind regions, whose extent is governed by the dimensions of the scale and goniometer head. Figure 6 shows the available part of the reflection sphere. The blind regions can be avoided by moving the additional axis from its position perpendicular to the principal axis to one coincident with that axis, which provides for one setting of the crystal a complete absence of blind regions, provided that the repeat distance along the direction coincident with that axis does not exceed 18 Å (when copper radiation is used). The blind regions may be eliminated completely if the intermediate axis can be set in any intermediate position. The simplest way of modifying the GUR-3 is to mount a special adapter of the arc type used in the RKOP camera [10,12]. The GUR, as thus modified, allows the head to be turned around its axis (the additional axis, γ, from 0-360°), while the holder may be turned on an arc (δ = 0-90°), and may be set either to bring the axis of the head perpendicular to that of the stage in the GUR (δ = 90°) or parallel to it (δ = 0°). The GUR-3, as modified, is shown in Fig. 7; Fig. 8 shows reflections of hkl type recorded with the URS-50 and GUR-3, modified in this way. The crystal had its b axis along the axis of the goni-

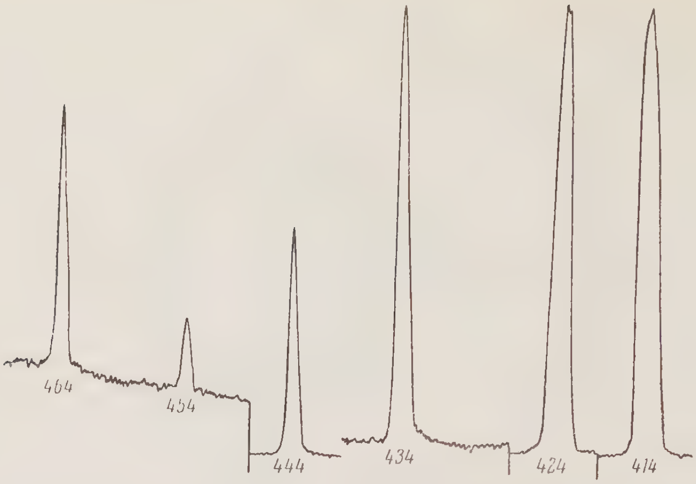

Fig. 8. Reflections from a Rochelle salt crystal recorded with a URS-50I and GUR-3 with special adapter. The ordinates are the intensities (units vary from reflection to reflection) corresponding to the planes whose indices are shown.

ometer head; the adjustment had previously been made by x-ray methods on another instrument, with final fine adjustment on the GUR itself. The reflections were recorded by setting δ, γ, ω, and Υ independently. The curves of Fig. 8 were recorded with the counter fixed each time in the position $\Upsilon = 2\omega$, the stage being turned at 0.25° per minute from $\omega = -1°$ to $\omega = +1°$. Various filters were inserted in order to record the strong reflections.[3]

Proper Uses of the Various Techniques of X-Ray Goniometry

There is sometimes expressed a demand for a diffractometer that, given a completely unknown crystal, would automatically provide all the information needed for a complete structure determination: cell parameters, list of all observed reflections, list of relative intensities. No attempt should be made to develop such an instrument at the present time.

It is best to derive the information about a structure in several stages. Ordinary photographic methods (rotation or oscillation) may first be applied to determine the shape and size of the unit cell. A photographic goniometer, e.g., the KFOR type [10, 11], may next be used to identify the systematic absences and hence the space group; such a camera gives an undistorted image of the reciprocal-lattice planes. The same camera may also be used to determine the shape and size of the unit cell.

The full data for the structure may be recorded photographically with a goniometer that provides equal-inclination recording (e.g., the RGNS type [12]). Here, further work is needed, as there is much loss of time in obtaining and processing the photographs. The full data must include series for all layer lines, which must be indexed and assigned relative intensities, either by reference to a density scale or by photometry.

A manual diffractometer (e.g., the modified URS-50I described above) may be used to accumulate the data, including the preliminary evaluation of setting angles for crystal and counter, setting of these angles, and recording (manually or otherwise) of the relative intensities. The object of using counters is to provide a major reduction in the time required to accumulate the data, while simultaneously providing higher accuracy on intensities. This will involve mechanization of the calculations before the problem can be considered as solved.

There is also a need for partly automatic diffractometers or for instruments providing automatic computation and setting of the angles; alternatively, such instruments might provide appropriate coupling between the crystal and counter motions.

LITERATURE CITED

1. M. Burger, X-Ray Crystallography [Russian translation] (IL, 1948).
2. A.I. Kitaigorodskii, X-Ray Structure Analysis [in Russian] (1950).
3. G.B. Bokii and M.A. Porai-Koshits, A Practical Textbook on X-Ray Structure Analysis [in Russian] (1950).

[3]Measurement of integral intensities is a complex question requiring a special discussion that cannot be accommodated here.

4. W. Cochran, "A Geiger-counter technique for the measurement of integrated reflexion intensity," Acta Cryst., 3, 268-278 (1950).
5. H. Evans, "Use of a Geiger-counter for the measurement of x-ray intensities for small single crystals," Rev. Sci. Instr., 26, 2, 156-161 (1953).
6. T.C. Furnus, "A Geiger-counter apparatus for collecting complete single-crystal diffraction data," Acta Cryst., 7, 620 (1954); T.C. Furnus and D. Harker, "Apparatus for measuring complete single-crystal x-ray diffraction data by means of a Geiger-counter diffractometer," Rev. Sci. Instr., 26, 449 (1955).
7. W.L. Bond, "An automatic recording x-ray diffractometer and plotting device," Acta Cryst. 7, 620 (1954); "A single-crystal automatic diffractometer," Acta Cryst., 8, 741-746 (1955).
8. B. Delone, N. Padurov, and A. Aleksandrov, The Mathematical Principles of the Structure Analysis of Crystals [in Russian] (1934).
9. F.L. Hirschefeld and G.M.J. Schmidt, "Geiger-counter measurements of single-crystall Bragg reflections. The geometrical problems," Bull. Res. Council Israel, 3, 37-45 (1953).
10. M.M. Umanskii, "Cameras for x-ray structure analysis," Collection: Application of X-Rays to the Examination of Materials [in Russian](1949), pp. 401-419.
11. Yu.A. Bagaryatskii and M.M. Umanskii, "A camera for photographing the reciprocal lattice. Part I. Principles and design of the KFOR," Zav. Lab., 15, 1320 (1949).
12. M.M. Umanskii, "Cameras for x-ray structure analysis," Collection: X-Ray Methods of Examination in the Chemical Industry [in Russian] (1953), pp. 119-138.

THE URS-50I AND URS-25I X-RAY DIFFRACTOMETERS FOR STRUCTURE ANALYSIS

Yu. K. Ioffe

Leningrad X-Ray Equipment Plant
Translated from Kristallografiya, Vol. 1, No. 4, pp. 460-467, July-August, 1956
Original article submitted September 5, 1955

Descriptions are given of the URS-50I and URS-25I, together with block diagrams and a brief description of the goniometer head. The URS-25I is meant for plant use in checking the cutting angles of quartz plates and has no automatic-recording facility. The URS-50I measures intensities to 3% by pulse counting or to ±6% with a pen recorder; the URS-25I measures intensities to ±10%.

X-ray analysis has been greatly simplified by the replacement of films by x-ray counters; in addition, there is a substantial saving in time and a marked improvement in accuracy.

The main advantages of x-ray counters are as follows:

(a) The minimum detectable intensity is much lower than for a film; a counter can register 2-3 Cu K_α quanta per second, whereas at least 10,000 Cu K_α quanta are needed to produce a detectable blackening at a point.

(b) Line intensities may be measured and recorded directly if suitable processing equipment is used, whereas an x-ray film needs the tedious operations of processing, microphotometry, and conversion of the density curve to an intensity curve.

(c) A counter usually gives higher accuracy than a film, because the emulsion on the latter varies in sensitivity, and the error is further increased by the microphotometer.

On the other hand, x-ray counters have the disadvantage of not revealing line structure (e.g., spottiness produced by coarse-grained specimens), and they demand complex electronic systems.

The URS-50I and URS-25I are intended for x-ray examination of materials; they provide high accuracy in Bragg focusing with polycrystalline sections, and also for polycrystalline wires, for single crystals in the equatorial plane, etc.

The URS-50I is intended for use in research institutes and industrial organizations; its output voltage is highly stabilized and is adjustable up to 50 kV, while the operation is largely automatic and of high precision.

The URS-25I is intended for plant use and provides up to 25 kV with two working positions; it differs from the URS-50I in being less precise and in having no automatic recorder. The URS-25I has been widely used in orienting quartz plates and in checking cutting angles. Figure 1 shows the block diagram of the URS-50I.

The URS-50I consists of three main units and one accessory: the x-ray equipment, the GUR-3 goniometer, the measuring equipment, and the VS-1 voltage stabilizer.

1. X-Ray Equipment. The control panel and EHT rectifier are included in this; the panel carries all the startup and control gear, including a six-tube current regulator for the x-ray tube. The EHT unit employs a doubler circuit giving a stabilized output, with

$$U_{\max} = 50\,\mathrm{kV} \quad \text{at} \quad I_{\max} = 12mA.$$

The EHT unit is linked via a cable to the tube; a set of tubes is provided, with anodes of Cr, Fe, Co, Ni, Cu, and Mo. The tube has a line focus 6 × 2.5 mm, whose projection along the axis of the working beam (at 2° to the plane of the anode) is only 0.3 × 2.5 mm. The anode is grounded and is water cooled. The tube has two beryllium windows, one working into the GUR-3; the other can work into an x-ray camera.

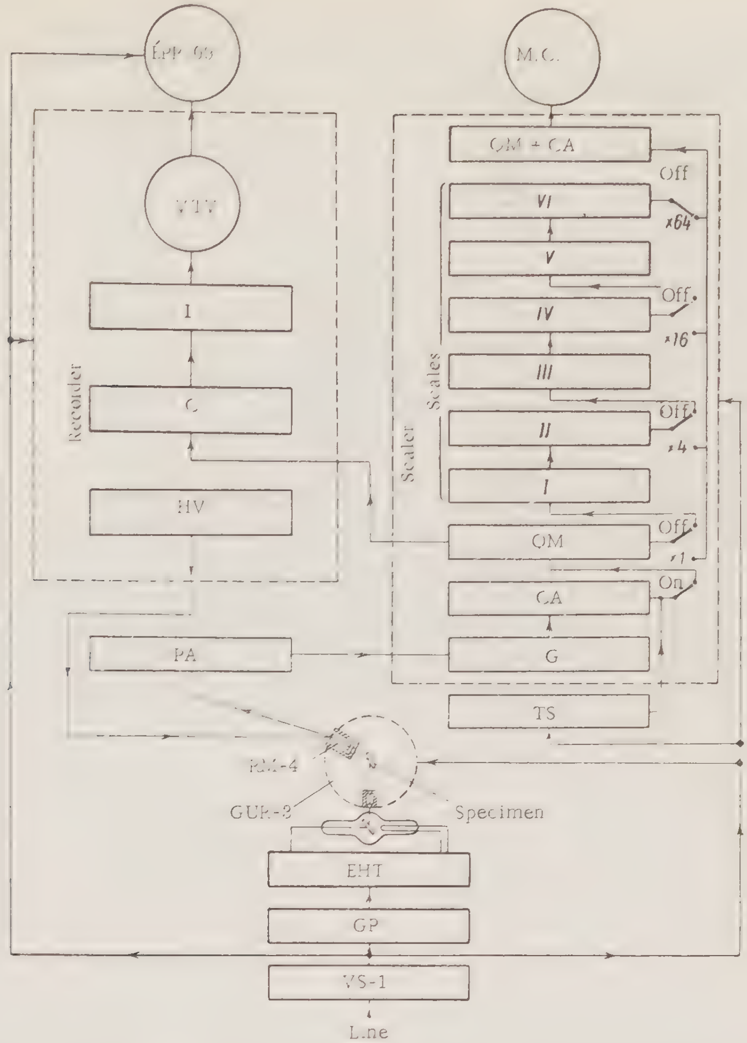

Fig. 1. Block diagram of the URS-50I. VS-1) voltage stabilizer, CP) control panel (with current stabilizer); EHT) tube supply; GUR-3) goniometer; RM-4) x-ray counter; PA) pulse amplifier; TS) time switch; MC) mechanical counter; G) gate; CA) clipping amplifier; QM) quiescent multivibrator; QM + CA) quiescent multivibrator + current amplifier; HV) power unit; C) clipper; I) integrator; VTV) vaccum-tube voltmeter; ÉPP-09) recorder.

2. Goniometer. This is used to measure diffraction angles. It carries the specimen, the x-ray counter, and all the parts for handling the x rays.

The latter consist of three vertical slits, two of which shape the beam (parallel or divergent); the third (receiving slit) is fixed in front of the counter. Sets of slits are provided, with widths of 0.1, 0.25, 0.5, 1.2, and 4 mm. In addition, two horizontal adjustable slits define the beam at the entrance to the goniometer and the counter.

The specimen (section or rod) rotates on the central axis, as does the arm carrying the receiving slit, the counter, and the pulse amplifier. The specimen-slit distance on the exit side equals the source-specimen distance (160 mm). The goniometer can take specimens weighing up to 5 kg, including small ovens, cooling units, etc. The specimen and counter may be rotated separately or together, the angular velocity of the counter being twice that of the specimen. The ratio 1 : 2 in the angles is accurate to ±1'. Bragg angles from −60 to +75° may be covered (twice this at the counter). The drive is manual or from a synchronous motor. The angles are read to ±1' by an optical projection system.

3. The Measuring Equipment. This consists of the RM-4 counter, PA pulse amplifier, scaler (with time switch and mechanical register), count-rate meter and counter power supply (in recorder unit), and an ÉPP-09 pen recorder.

The counter has a mica end window about 20 μ thick; the x-ray quanta produce output pulses at the load resistor of the counter, which are amplified and passed to the scaler, whose first three stages shape the pulses appropriately before passing them to the scales and count-rate meter. Scaling factors of 4, 16, and 64 are fitted, because the count rate may be as high as 5000 sec^{-1}, while the mechanical register will accept only 100 sec^{-1}, and then only if the pulses are equally spaced.

The pulse from the appropriate scale triggers the quiescent multivibrator, which drives the current amplifier, which provides a pulse of duration suitable to operate the register. This records the number of counts recorded in a given time as divided by the scaling factor. The counting time may be controlled manually or by an automatic timer. The count-rate meter averages the rate over a given period; it consists of a clipper, an integrator, and a vacuum-tube voltmeter. The clipper provides a suitable pulse shape, while the integrator is simply a capacitor that is charged by these pulses and that discharges through a shunt resistor. The steady voltage developed at the condenser is proportional to the count rate; it is measured by the vacuum-tube voltmeter, which reads the mean counts per second.

This ratemeter feeds a pen recorder type ÉPP-09, whose chart is driven in synchronism with the counter, the abscissa being proportional to the angle of rotation and the ordinate proportional to the count rate. This gives an $I = f(v)$ curve. The chart speed is adjustable between limits of 60 and 9600 mm/h, which is equivalent to 0.5-640 mm/deg. Angles can be read to ±0.5% from the chart.

4. The voltage stabilizer feeds all the equipment and gives ΔU_{eff} of ±0.2% or ΔU_a of ±1.5% for line variations from +5 to –15% of nominal.

The units are linked as follows. The beam from the tube is shaped to divergent or parallel form by the first two slits in the goniometer; the rays scattered by the specimen at the Bragg angle are received by the counter as it rotates around the axis of the goniometer, the peaks corresponding to positions of maximum intensity, at which the counter may be set. The angles and intensities may be read in three ways:

(1) The counter and specimen are set at specified angles, with the scaler operating into the register to record the counts occurring in a certain time. This measurement is repeated at other angles to record the appropriate part of the pattern.

(2) The specimen and counter are driven manually while observing the ratemeter reading, which indicates the appropriate diffraction angles and the relative intensities.

(3) Uniform rotation of specimen and counter by a synchronous drive, in conjunction with recording on the chart; this provides a recording of any desired part of the pattern.

The URS-25I has no scaler or recording system, so the angles and intensities are read as in (2) above. The x-ray side of the equipment is the same in both.

The basic considerations in the design of the equipment have been high accuracy in conjunction with minimum consumption of time and labor.

High accuracy requires: (a) stabilized emission, (b) precision measuring circuits, (c) statistical accuracy in the results.

The URS-50I has stable emission by virtue of the line stabilizer and current stabilizer. The two together keep the x-ray intensity within ±3% of the set value for line fluctuations of +5 to –15% from nominal. The scaler has no source of error (apart from that in the timer, which is negligible), so ±3% represents the maximum range of the error arising from line fluctuations.

The integrator is linear to ±3%, while the vacuum tube voltmeter and recorder are linear to 1% and 0.5%, respectively. Tests have shown that the intensity is measured to ±6% at the recorder for these +5 to –15% line fluctuations. The random error in the results due to the random arrival of the quanta may be specified in terms of the probable error. The relative probable error for a scaler is $\Delta\varepsilon = 0.67/\sqrt{N} = 0.67/\sqrt{\bar{n}t}$, while for a ratemeter it is $\Delta\varepsilon = 0.67/\sqrt{2\bar{n}RC}$; in which N is the number of quanta arriving in time t, $\bar{n}$ is the mean rate of arrival (per second), and C and R are the capacitance and resistance of the integrating circuit. A Gaussian distribution fits the probability of a deviation of given ratio to the probable error:

Multiple of $\Delta\varepsilon$:	1	2	3	4	5
Probability of error exceeding above multiple, %:	50	17.7	4.3	0.7	0.07

The required accuracy is specified; then $\bar{n}$ indicates the measurement time t needed. The timer provides periods of 16, 32, 64, and 128 sec, which covers the range needed to give rapid (but not very exact) readings, and also very precise readings

Fig. 2. General view of the URS-50I.

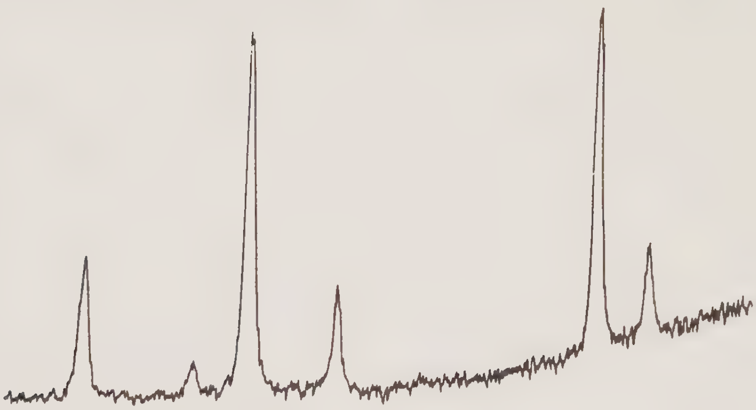

Fig. 3. Part of a chart recording for CaF_2 powder, with 1° in $2\vartheta \approx$ 10 mm; Cu K_α, counter speed 4 deg/min, RC = 1 sec in integrator.

over fairly long periods. The RC provided for the same purpose are 1,2,4, and 8 sec, which are selected by a switch. The ratemeter has two ranges, with full-scale deflection for $\bar{n}$ of 1000 and 200 sec^{-1}. The RC are switched independently of these ranges.

The RC needed is also governed by the recording rate (angular speed of counter); it may be shown that the loss in peak height on account of lag in the integrator can be kept below 5% if $\omega_c < \Delta l / 3RC$, in which Δl is the width (in terms of 2ϑ) of the leading edge of the line. Typical lines from polycrystalline materials indicate that the best speeds in 2ϑ are 4, 2,1, and 0.5 deg/min. The URS-50I thus provides the maximum accuracy compatible with a given working time.

The practical accuracy of the URS-25I over periods of a few minutes is ±10%. The integration times are half those for the URS-50I.

The URS-50I (Fig. 2) consists of two major units: the control rack and the measuring rack. The first contains the x-ray tube (in its shield) and the goniometer, while the second contains the voltage stabilizers and all the measuring equipment apart from the counter and pulse amplifier. This enables one to use the x-ray equipment or measuring equip-

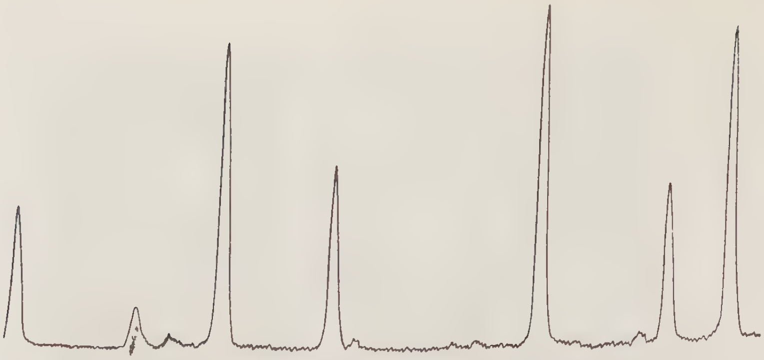

Fig. 4. Part of a chart recording for Al_2O_3 powder, with 1° in $2\vartheta \approx 12$ mm; Cu $K\alpha$, counter speed 0.5 deg/min, RC = 8 sec.

ment separately in other experiments with ionizing radiations (e.g., radioactive tracers).

The URS-25I consists of the x-ray unit and two panels bearing the ratemeter. The x-ray unit also houses the two goniometers, together with the voltage stabilizer.

Prototype URS-50I and URS-25I units were put on test for two years; they were found to be reliable and to provide the accuracy stated above. The resolution is fully adequate for many structure problems (the Cu K_α doublet reflected from a quartz crystal with slits of 0.1 mm is resolved almost at half height). The URS-50I provides a time saving by a factor of 5-10 (sometimes more) by comparison with photographic methods. Figures 3 and 4 show typical recordings. The URS-50I and URS-25I were designed at the Barevestnik plant under the direction of the chief designer, A.A. Porfir'ev.

Much assistance in the development was received from the following: G.V. Kurdyumov, I.B. Borovskii, Yu.A. Bagaryatskii, A.I. Zaslavskii, M.M. Umanskii, B.M. Levitskii, V.A. Il'ina, and A.I. Froiman.

THE KRON-1 X-RAY CAMERA FOR EXAMINING EUHEDRAL AND IRREGULAR CRYSTALS

V. A. Frank-Kamenetskii, M. A. Rumsh, and A. I. Komkov

Zhdanov University, Leningrad

Translated from Kristallografiya, Vol. 1, No. 4, pp. 468-471, July-August, 1956
Original article submitted September 5, 1955

The usual way of starting the x-ray examination of a crystal without faces is to record a series of Laue patterns in order to determine the symmetry and orientation. Then rotation or oscillation photographs are recorded with the principal crystallographic directions along the axis of rotation. It is often necessary to alter the orientation of the crystal by cementing it in a fresh position in the holder. This operation, and the determination of the new orientation, can be a very laborious task, especially if the crystal is small, because a fresh series of photographs must be taken, for use in stereographic projection. This makes it desirable that the camera should allow one to make the necessary adjustment merely by rotating parts of the goniometer head.

The RKOP [1] and RKV [2] cameras are used with crystals, but they have several disadvantages in that respect. For example, the RKV allows one to place most crystallographic directions along the primary beam, but there is much less scope for doing this as regards the axis of the camera. Conversely, the RKOP allows all directions to be brought into coincidence with that axis but restricts the scope for adjustment to the primary beam.

The present camera contains a goniometer that allows one to go from Laue patterns to oscillation patterns in any direction without remounting. One special object here has been to keep the design simple and convenient while permitting one to use a crystal that has been mounted once only. The rotations are of two types [3]: multiples of 45° and up to 22°30'. These are provided by the fitting 10 (Fig.1) on the slide 9 in the upper small arc. This fitting has three recesses 11, the axis of one being at 45° to the adjacent axis. The crystal holder 13 may be set in eight distinct positions in each recess. The holder is transferred from one position to another by rotation through 45° about its own axis. Resetting in the upper main recess may be combined with rotation in the lower in the large arc 5 to rotate the crystal through any angle around a horizontal axis perpendicular to the primary beam. Transfer of the holder from the main recess to the middle or lower one causes the crystal to turn through 45 or 90°, respectively, about the primary beam. This change of setting may be combined with movement of the fitting in the upper small arc 7 to turn the crystal around the beam through any angle up to 112°30'. These combinations are sufficient to bring any direction in the crystal into coincidence with the primary beam or with the axis of rotation.

This separation of the motions has provided a reduction in the angular range needed in the head from ±60° (in the RKV) to ±22°30', which makes for a much simpler camera; but the detailed structure of the head becomes somewhat more complicated, because the recesses 11 in the fitting must be located very precisely, as must the locating holes in each. Each position must be completely positive in location, and the crystal holder must everywhere be firmly held.

We have devoted particular attention to maximal accuracy of indication in each position, because a correction can afterwards be applied for any error in the marks, Each specimen of the head need merely be examined on an optical goniometer (or other suitable instrument), the angles of rotation arising from resetting being determined to 0.1°. The errors in the marks can hardly ever exceed 1°, so there is rarely any need to use the corrections.

It is simple to decide the order of operations in order to bring direction [mnp] into coincidence with the beam or the rotation axis. Figure 2 shows

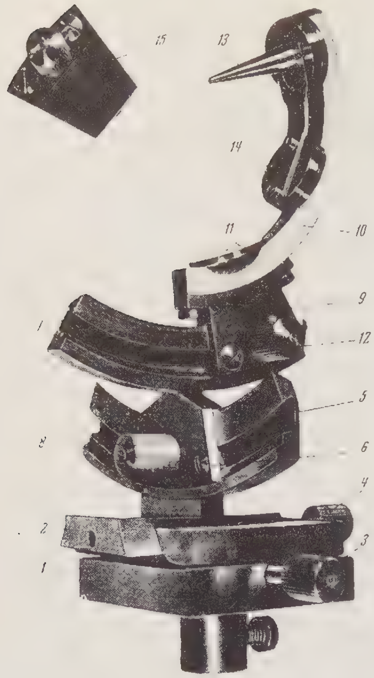

Fig. 1. General view of the goniometer head in the KRON-1: (1) and (2) centering slides; (3) and (4) drive screws for slides; (5) lower arc (fixed part); (6) moving part of the lower arc; (7) upper arc (fixed part); (8) and (12) limit screws on arcs; (9) moving part of upper arc; (10) holder for recesses; (11) recess; (13) crystal holder; (14) spring clamp for crystal holder; (15) ordinary moving part of upper arc.

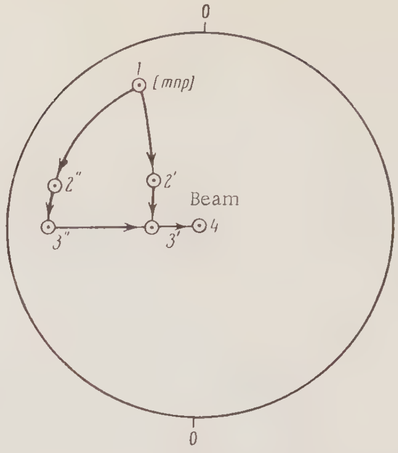

Fig. 2. The two methods of bringing direction [mnp] into coincidence with the beam in the KRON-1 (see text).

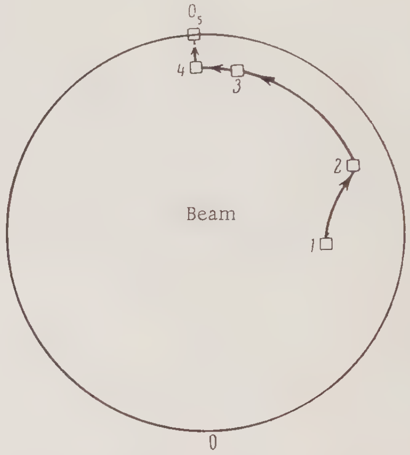

Fig. 3. Bringing direction [mnp] into coincidence with the axis of rotation in the KRON-1 (see text).

a stereographic projection of an [mnp] direction that cannot be brought into coincidence with the primary beam in the RKV. There are two ways of producing such coincidences in our camera.

Method 1. The crystal holder is moved in the main recess to transfer direction [mnp] from position 1 to position 2'; adjustment on arc 5 (Fig. 1) then transfers it from position 2' to position 3'. Rotation around the camera axis OO (Fig. 2) then brings it into coincidence with the primary beam (position 4).

Method 2. Direction [mnp] is transferred from position 1 to position 2" by transferring the crystal holder from the main recess to one of the others. Adjustment on arc 7 (Fig. 1) transfers it from 2" to 3"; then rotation of the head brings it into coincidence with the primary beam. The fitting in the lower arc (angular range 22°30') theoretically allows one to bring any direction into coincidence with the primary beam; but this camera still has a dead region (a range of directions that cannot be brought into coincidence with the beam), whose size is determined by that of the crystal holder. This is less than 2% of all directions in the present camera.

A direction [mnp] within the dead space of the KRON-1 is brought into coincidence with the rotation axis as follows (Fig. 3). The crystal holder is adjusted in the main recess to transfer [mnp] from position 1 to position 2, while transfer of the holder from the main recess to one of the others brings it to position 3. Adjustment on the upper arc then brings [mnp] to position 4, and adjustment on the lower arc brings it to position 5 (coincidence with the rotation axis).

This camera allows any direction to be brought into coincidence with the rotation axis, but the multiple-rotation fitting makes it somewhat more difficult to record rotation patterns. Patterns involv-

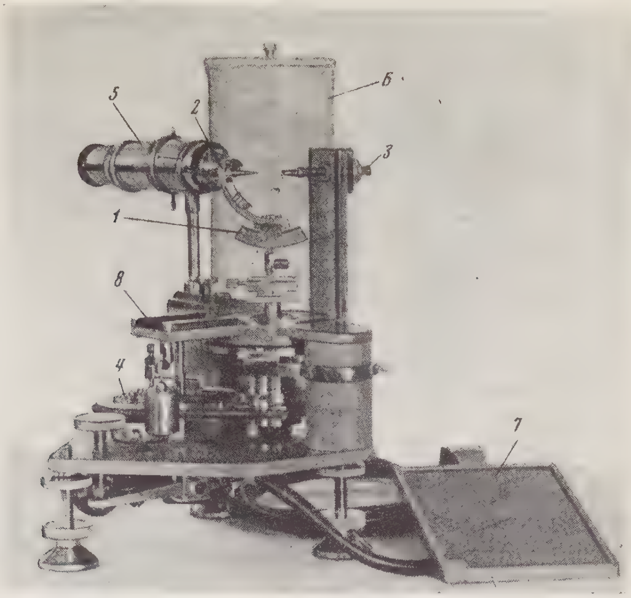

Fig. 4. General view of the KRON-1: (1) goniometer head; (2) multiple-rotation fitting; (3) collimator; (4) oscillation mechanism; (5) sighting tube for centering specimen; (6) cylindrical metal cassette; (7) flat cassette; (8) support for sighting tube and cassette.

ing complete rotation are used in order to establish the trends in the absences, which may also be deduced from oscillation photographs if the range of oscillation exceeds 180°. The oscillation mechanism in our camera provides ranges of 6, 12, and 18°; but this mechanism can be uncoupled from the goniometer head, so it can give a series of oscillation patterns covering a wide angular range.

Sometimes a rotation pattern must be recorded with the crystal holder in the lower recess; in that case, slide 9 may be replaced by the ordinary slide 15, which has a single vertical recess. The transfer of the holder to this slide does not alter the orientation of the crystal, while the use of the ordinary slide enables one to record ordinary rotation patterns.

Figure 4 gives a general view of this camera as it was made in the workshops of the Physics Faculty at Leningrad University.[1]

LITERATURE CITED

1. Yu.A. Bagaryatskii and M.M. Umanskii, "Cameras for x-ray structural analysis of single crystals," Zavod. lab., 14, 639 (1948).
2. M.M. Umanskii, "Cameras for x-ray structural analysis," Collection 3: Application of X Rays to the Investigation of Materials [in Russian] (1949), p. 401.
3. V.A. Frank-Kamenetskii and A.I. Komkov, "A fitting for a rotation camera for x-ray goniometric examination of crystals," Zavod. lab., 21, 738 (1955).

[1]We are indebted to E. A. Dobrinskii for assistance in the design of the camera.

BRIEF COMMUNICATIONS

DIFFERENTIATION OF DYNAMIC AND KINEMATIC TYPES OF SCATTERING IN ELECTRON DIFFRACTION

B. K. Vainshtein and A. N. Lobachev

Institute of Crystallography, Academy of Sciences of the USSR
Translated from Kristallografiya, Vol. 1, No. 4,
pp. 472-473, July-August, 1956
Original article submitted May 19, 1956

Either type of scattering may occur; the decisive features are the complexity of the structure, the atomic numbers of the constituents, and the thickness of the crystal. The scattering is certainly dynamic if Kikuchi lines appear. Kinematic scattering is usual for polycrystalline films and textures, and also on occasion for single crystals; this is confirmed by the relation of the theoretical (kinematic) intensities to the observed ones, as well as by other considerations [1,2]. Dynamic scattering it still possible, however.

Scattering of intermediate type may also occur [2] if the specimen contains a range of crystal sizes. The precise nature of the scattering must be established in order to convert the observed intensities to $|\Phi|$ or $|\Phi|^2$ for use in structure analysis.

The mean intensity may be examined as a function of $(\sin\theta/\lambda)$ in order to establish the type without resort to assumptions about the size or structure of the crystals; this is compared with f^2_{em} or f_{em}. Relationships deduced for x rays [3] apply here for $\overline{|\Phi|}$ and $\overline{|\Phi|^2}$:

$$\overline{|\Phi|^2} = \sum_i f^2_{e\,i} \sim f^2_{em} \quad \text{and} \quad \overline{|\Phi|} \sim f_{em}. \tag{1a,b}$$

For kinematic scattering, $I = k|\Phi|^2$ (the k are intensity factors), and the $\overline{I/k}$ should fall off as f^2_{em}, in accordance with (1a); dynamic scattering gives $I = k|\Phi|$, and here the f_{em} of (1b) should be followed. Only the type of fall is important, i.e., the relative values of the quantities in (1a,b), so we may assume that the f_e curves are similar, and we may replace the exact relation

$$f_{em} \sim \sqrt{\sum_i f^2_{e_i}}, \tag{2a}$$

with the sum taken over all atoms in the unit cell, by the simpler one

$$f_{em} \sim \sum_i f_{e\,i}, \tag{2b}$$

or even use the f_e curve for the atom of mean weight in the structure in place of the f_{em} curve.

There is also another approach. We use the experimental I_{hkl} to convert to $|\Phi|$ from the kinematic formulas, which give $|\Phi_{hkl}|_k = \sqrt{I_{hkl}/k}$, and from the dynamic ones, which give $|\Phi_{hkl}|_d = I_{hkl}/k$. We average and compare the f_{em} in accordance with (1b) to determine which is the correct formula, i.e., the type of scattering. The true $\overline{|\Phi|}$ should lie closer to f_{em}. The $|\Phi_{hkl}|_k$, $|\Phi_{hkl}|_d$ (or the $\overline{I_{hkl}/k}$ in the first method) must be averaged over relatively large spherical zones in the reciprocal lattice, e.g., from $(\sin\theta/\lambda)\cdot 10^{-8} = 0$ to 0.2; from 0.2 to 0.4, and so on. Let any of of these quantities be A_{hkl}; then

$$\bar{A} = \sum_{j=1}^{m} A_{hkl}/m, \tag{3}$$

in which m is the number of reflections in the given spherical zone. The points (here $\bar{A}_{0,1}$, $\bar{A}_{0,3}$, etc.) define the $\bar{A}$ curve. The relative values are found by equating these to f_{em} at the first point, the fall then being examined.

Many of the specimens previously examined have given kinematic scattering, but a test by the above method (second form) for area $CO(NH_2)_2$, which gives spot patterns, showed that the scattering was dynamic. The intensities in the h0l zone, as determined from multiple exposures [4], gave the $|\Phi_{hkl}|_k = \sqrt{I_{hkl}/d_{hkl}}$ and $|\Phi_{hkl}|_d = I_{hkl}/d_{hkl}$.

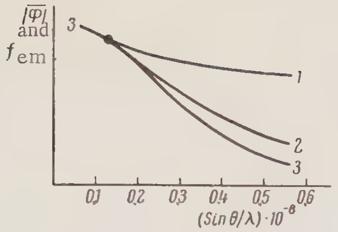

Fig. 1. Experimental curves for: (1) $|\overline{\Phi}|_k$ and (2) $|\overline{\Phi}|_d$ for urea; the latter is close to the theoretical curve (3), f_{em}, for urea.

(The factor analogous to the Lorentz factor for x rays is here d_{hkl} and is present in both cases in the same form, being $k = pd^2_{hkl}$ for a polycrystal, for example.) Averaging as in (3) gave the curves of Fig. 1, which show that the scattering is dynamic; the $|\overline{\Phi}|_d$ curve even runs a little above the f_{em} one. This is due to secondary scattering, which tends to equalize the intensities. This secondary scattering is also evident from the weak 100 and 300 reflections, which are forbidden.

LITERATURE CITED

1. Z.G. Pinsker, Electron Diffraction [in Russian] (1949).
2. B.K. Vainshtein, "The kinematic theory of reflection intensities for electron-diffraction patterns," Kristallografiya, 1, 1, 17-26 (1956).
3. A.I.G. Wilson, "The probability distribution of x-ray intensities," Acta Cryst., 2, 318-321 (1949).
4. B.K. Vainshtein and Z.G. Pinsker, "An electron-diffraction study of a paraffin," Tr. Inst. Kristallogr., 6. 161-172 (1951).

THE ONE-DIMENSIONAL INFINITE CRYSTALLOGRAPHIC GROUPS

N. V. Belov

Institute of Crystallography, Academy of Sciences of the USSR

Translated from Kristallografiya, Vol. 1, No. 4,
pp. 474-476, July-August, 1956
Original article submitted January 23, 1956

The international symbols for the crystallographic groups are extremely convenient for infinite three-dimensional one-color (space) and two-color (Shubnikov [1]) groups; they have also been used to advantage with the infinite two-dimensional groups (analogs: one-color = one-sided; two-color = two-sided [2]). In addition, they are of value in identifying and enumerating the various types of infinite one-dimensional groups: one-sided (borders [3]), two-sided (strips [3]), and rods [3,4]. We use three positions in the symbol, as usual; the first is related to the infinite translational x axis (a), the second to the y axis (in the plane), and the third with the z axis (perpendicular to that plane). We may then readily deduce the restrictive conditions imposed on the numbers and letters that may appear in positions 1, 2, and 3; all possibilities may be enumerated rapidly. The one-sided groups allow only m planes in the first position, only m and *a* planes in the second, and only the symbol for a 2 axis (perpendicular to the plane of the border) in the third. The elements of crystallography imply that this 2 axis in position 3 is obliged to be derived from the two symmetry elements in the first two positions if these are present together; it can occur independently only if they are absent. This gives us 7 groups: p111, pm11, p1m1, p1*a*1, pmm2, pm*a*2, p112.

The fixed p in front of the symbol denotes the infinite group of translations (Bravais lattice), which is essential and identical for all the one-dimensional infinite groups. Figure 1 shows these seven groups schematically in terms of triangles in four orientations. Shubnikov in his "Symmetry" gives some striking examples of these borders.

A second symmetry element is possible in each of the three positions in the case of two-sided strips, this being normal to the symmetry elements of the borders, e.g., a 2 or 2_1 axis is possible in the first position. This axis is placed in the numerator of the symbol if it is present together with an m plane normal to it, the plane being placed in the denominator. The second position also allows a 2 axis, while the third allows m and *a* planes. The presence (symbol) of a symmetry element in the numerator or denominator of any position generates a derived center of symmetry unrelated to any coordinate direction and, hence, acting on the symmetry elements in all three positions. The center of symmetry is not indicated if any position contains both numerator and denominator; but it must be indicated [1] if it remains the sole symmetry element, when we do not indicate three positions, of course.

This gives us the following 31 groups: (1) p111 = p1, (2) pi, (3) p211, (4) p$2_1$11, (5) p121, (6) p112, (7) p222, (8) p$2_1$22, (9) pm11, (10) p2/m11, (11) p2_1/m11, (12) p1m1, (13) p12/m1, (14) p1*a*1, (15) p12/*a*1, (16) p11m, (17) p11*a*, (18) p112/m, (19) p112/*a*, (20) pmm2, (21) pm*a*2, (22) pm2m, (23) pm2*a*, (24) p2mm, (25) p2_1*a*m, (26) p2_1m*a*, (27) p2*aa*, (28) pmmm, (29) pm*a*m, (30) pmm*a*, (31) pm*aa*.

Groups 1, 6, 9, 12, 14, 20, and 21 repeat the 7 listed above, while groups 16, 18, 22, 24, 25, 28, and 29 are the corresponding gray groups [1,2].

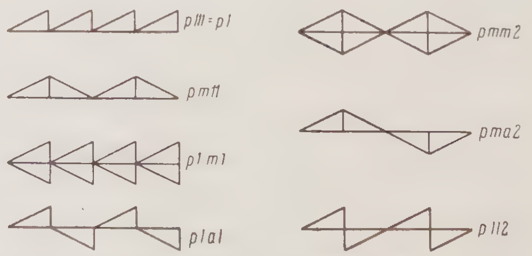

Fig. 1. The one-dimensional one-sided infinite groups (borders).

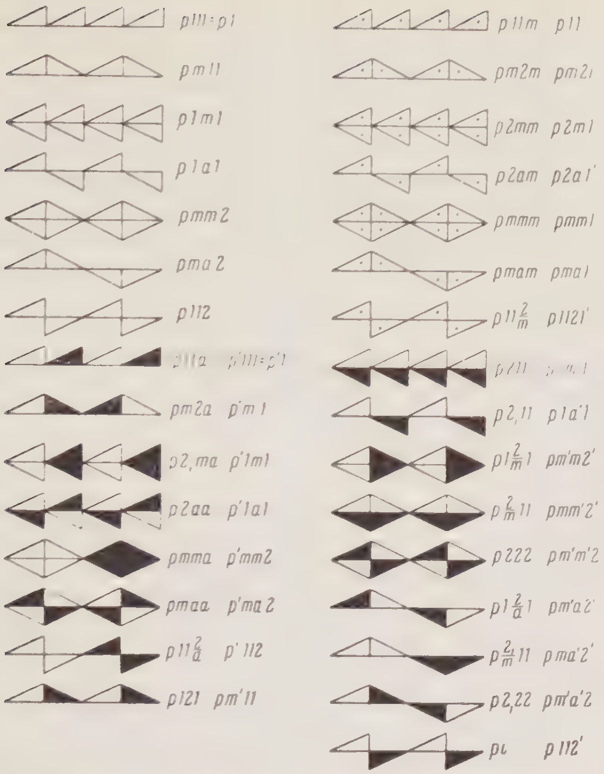

Fig. 2. The one-dimensional two-sided infinite groups (strips).

Figure 2 shows the one-sided and gray groups. Only the remaining 17 are the two-sided black-and-white groups in the narrowest sense. The 7 groups and the 31 may readily be deduced from the corresponding schemes for the 80 planar two-color (two-sided) groups [4].

The 31 groups are very much easier to derive if we consider them as one-sided, but the two-color ones as black and white [1,2]; and here we take account of the possible color translation, i.e., second Bravais lattice p'. Then, from [2], we start from the 7 one-color groups and first list the 7 gray groups. Then follow the two-color groups with the uncolored translation (p), which are obtained by replacing one or both of the basic elements by color ones in the symbols for the one-color groups; the latter symbols are denoted (as in [2]) by primes. Finally we list the 7 symbols of the one-color groups with the symbol of the one-color lattice replaced by the two-color one. Figure 1 gives these 7 + 7 + 10 + 7 groups in that order, the symbol being given as in the three-dimensional form. The color Bravais lattice has m planes perpendicular to the translation axis alternating with m' ones, whereas m planes parallel to that axis are simultaneously color glide planes, and, conversely: m ≡ a'; a ≡ m'; p'mm2 = p'm(m'), m(≡ a'), 2, etc., as in the two-color groups (two- and three-dimensional) and as can be seen from Fig. 2.

Rods allow a rotation or screw axis of any order along the first (infinite) axis; the second and third axes cease to be topologically distinct, and they may be chosen not from the requirement of mutual perpendicularity but in accordance with the rules of the crystallographic setting (crystallographic system).

We consider here only the rod groups that are subgroups of the 230, i.e., that are related in not allowing axes of orders 5, 7, 8, and higher; this gives us the following groups, which are subdivided in accordance with the order of the principal axis:

$n=3$				
$p\,311$	$p\,3/m\,11 = p\,\bar{6}11$	$p\,32\;p\,3\,m$	$p\,3/m\,m\,2 = p\,\bar{6}\,m\,2$	
			$p\,3/ma\,2 = p\,\bar{6}\,a\,2$	
$p\,3_1 11$	$p\,\bar{3}11 = p\,\mathring{6}11$	$p\,3_1 2\;p\,3\,a$	$p\,\bar{3}\,2/m = p\,\mathring{6}\,2/m$	
$p\,3_2 11$		$p\,3_2 2$	$p\,\bar{3}\,2/a = p\,\mathring{6}\,2/a$	
$n=4$				
$p\,411$	$p\,4/m\,11\;p\,\bar{4}11$	$p\,422$	$p\,4\,mm\;p\,\bar{4}2\,m$	$p\,4/m\,mm$
$p\,4_1 11$	$p\,4_2/m\,11$	$p\,4_1 22$		
$p\,4_2 11$		$p\,4_2 22$	$p\,4_2 ma\;p\,\bar{4}2\,a$	$p\,4_2/mma$
$p\,4_3 11$		$p\,4_3 22$	$p\,4\,aa$	$p\,4/maa$
$n=6$				
$p\,611$	$p\,6/m\,11$	$p\,622$	$p\,6\,mm$	$p\,6/mmm$
$p\,6_1 11$	$p\,6_3/m\,11$	$p\,6_1 22$	$p\,6_3\,ma$	$p\,6_3/mma$
$n\,6_2 11$		$p\,6_2 22$	$p\,6aa$	$p\,6/maa$
$p\,6_3 11$		$p\,6_3 22$		
$p\,6_4 11$		$p\,6_4 22$		
$p\,6_5 11$		$p\,6_5 22$		

Noncrystallographic n cause changes in the number of groups mainly on account of the increasing number of possible screw axes. A difference between our symbols and the international ones is that we denote inversion axes ($\bar{3}$, $\bar{6}$) as well as mirror ones ($\mathring{3}$, $\mathring{6}$), with the equivalence $\bar{3} = \mathring{6}$ and $\bar{6} = \mathring{3}$. The rod groups with limiting (infinite) symmetry elements have been considered by Shubnikov in his "Symmetry."

LITERATURE CITED

1. N. V. Belov, N. N. Neronova, and T. S. Smirnova, "The 1651 Shubnikov groups," Tr. Inst. Kristallogr., 11, 33-67 (1955).
2. N. V. Belov and T. N. Tarkhova, "The color-symmetry groups," Kristallografiya, 1, 6-13 (1956).
3. A. V. Shubnikov, Symmetry [in Russian] (1940).
4. E. Alexander, "Systematik der eindimensionalen Raumgruppen," Z. Krist., 70, 367-382 (1920).

ATTRACTION BETWEEN CENTERS OF SPIRALS OF OPPOSITE SIGN DURING CRYSTAL GROWTH

G. G. Lemmlein and E. D. Dukova

Institute of Crystallography, Academy of Sciences of the USSR
Translated from Kristallografiya, Vol. 1, No. 4,
pp. 477-478, July-August, 1956
Original article submitted May 19, 1956

We have previously [1] described the formation of screw dislocations during crystal growth and have explained the production of screw dislocations of opposite signs within a single crystal.

Here we report observations on the displacement of the centers of spirals of opposite signs during the growth of a crystal of p-toluidine.

In 1950, Frank [2] gave a scheme for the formation of concentric layers generated by two dislocations differing in sign. The same were found on morphologic examination of the faces, which confirmed Frank's prediction, although this was based on a static picture and on the assumption that the points of emergence of dislocations remain fixed during crystal growth. We have examined some details of this for pairs differing in sign.

Prolonged observation of concentric circles (growth spirals differing in sign) showed that the centers slowly come together; the layers cease to grow when the two centers fuse.

This has been recorded on cine film (speed,one frame every two seconds).

Parts a-h of Fig. 1 show enlarged areas of frames that illustrate the migration of two centers during growth; the two come together in the process, and the interaction increases as the distance decreases, as is clear from the intervals quoted in a-h.

No more new spiral layers are formed when the two screw dislocations are directly adjacent; if they have the same pitch (Burgers vector), they mutually cancel, as in the above series. Parts f-h of Fig. 1 show the growth of the closed layer formed by the last turns, a smooth surface being left.

The layers generated by the dislocations might have been different in thickness, in which case dislocations of opposite signs could not cancel out exactly when they fused; the residue would be a single dislocation of Burgers vector equal to the difference between the two individual values.

This fusion occurs over a long period,the crystal meanwhile increasing appreciably in thickness by tangential growth. The layers in our case were about 20 unit cells (about 0.047 μ) thick, while the two dislocations fused when the crystal had increased in thickness by about 4 μ. The time taken was about an hour.

The recordings were made between crossed polarizers; the interference color increased in order during the process and so gave thickness estimates for the layers and for the crystal as a whole.

The two centers come together at a substantial rate when their separation on the surface is of the order of the distance between turns. The separation may be judged from the figure formed by the first turns of the spirals. A separation twice the distance between turns causes the spirals to fuse into an ellipse enclosing a figure resembling the letter E, which subsequently becomes an ellipse enclosing a fresh E (Fig. 2a,b). A smaller separation causes the layers to form at first semicircles, which grow together to form a figure closely resembling a circle.

A separation in excess of twice the distance between turns will lead to little interaction, and the centers remain unmoved during the growth.

A separation of about the distance between turns will cause the two centers to come together when the Burgers vector is not very large.

This process shows that screw dislocations of opposite sign can come together (and even fuse) during growth. Fusion of dislocations with equal vectors will cause the growth of both to cease; the sources of the spiral layers are destroyed. It is

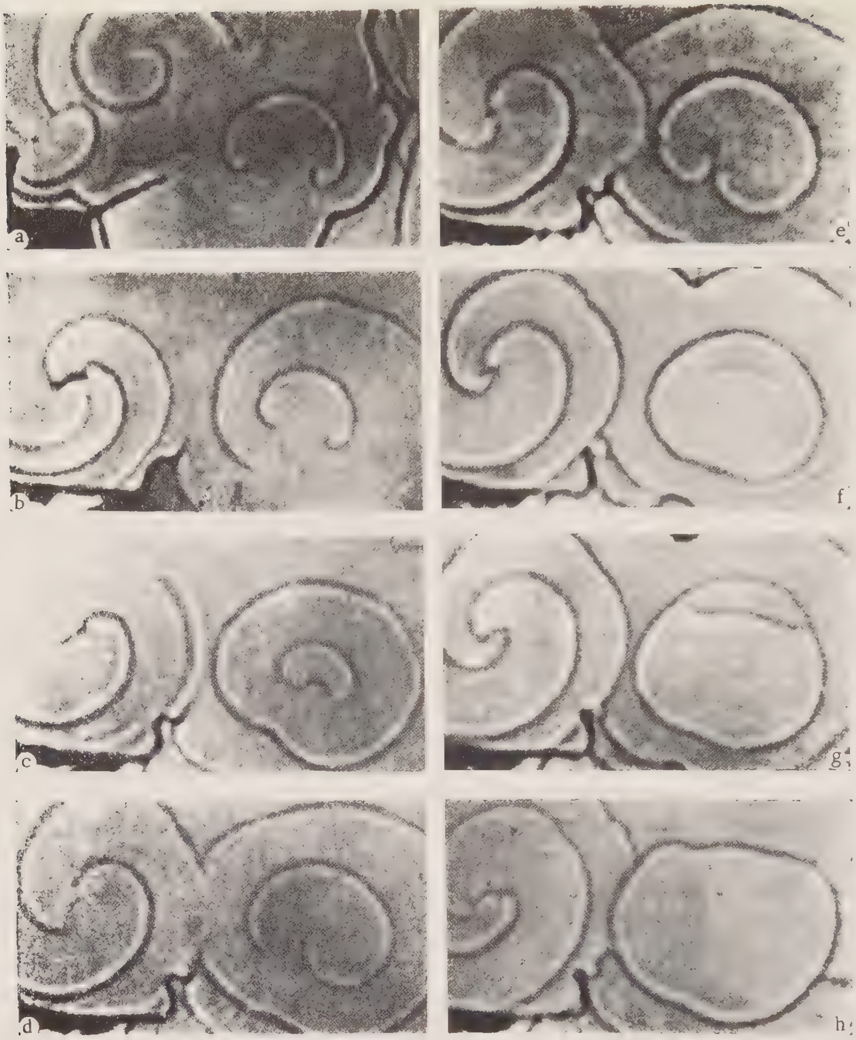

Fig. 1. Approach of two centers of spirals differing in sign during growth. The intervals are as follows: a to b, 24 min; b to c, 16 min; c to d, 6 sec; d to e, 6 sec; e to f, 40 sec; f to g, 26 sec; g to h, 1 min.

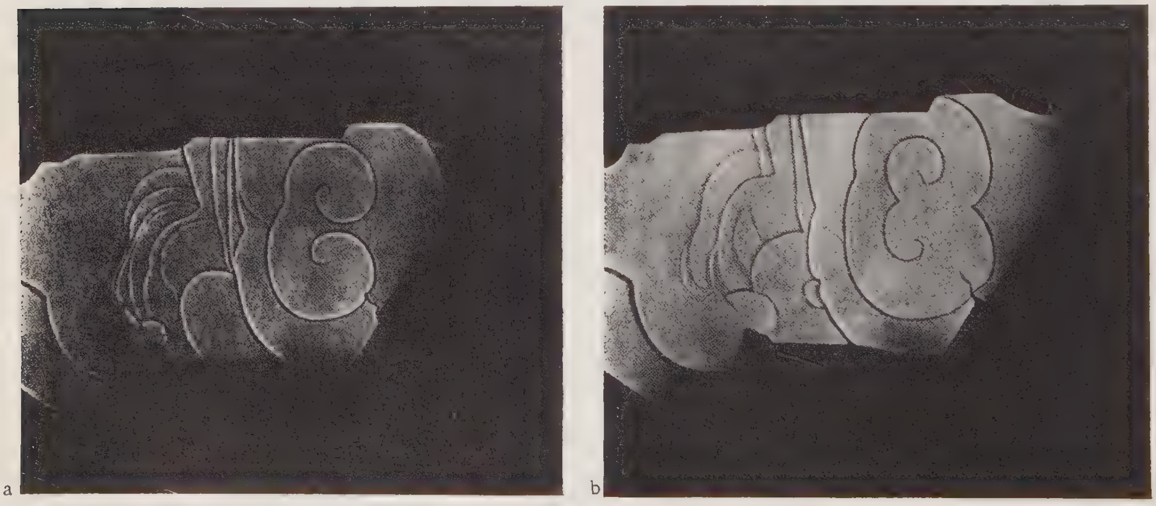

Fig. 2. Interaction of spirals differing in sign when the centers are separated by twice the distance between turns.

not yet clear whether the process represents migration of the screw dislocations themselves (lattice defects) or merely of the points of emergence on the surface.

LITERATURE CITED

1. G.G. Lemmlein and E.D. Dukova, "Formation of screw dislocations during growth of a crystal," Kristallografiya, 1, 3, 351-355 (1956).
2. F.C. Frank, "Note on the structure of a crystal surface," Phil. Mag., 41, 313, 200-205 (1950).

A STUDY OF THE CRYSTAL STRUCTURES OF ALUMINUM AND CHROMIUM ACETYLACETONATES

E. A. Shugam and L. M. Shkol'nikova

All-Union Research Institute for Chemical Reagents,
Ministry for the Chemical Industry of the USSR
Translated from Kristallografiya, Vol. 1, No. 4,
pp. 478-482, July-August, 1956
Original article submitted April 17, 1956

The present study is a continuation of work which has been carried out in the Institute for Chemical Reagents on the crystal structures of metal acetylacetonates [1,2].

Metal acetylacetonates belong to the general class of internal complex salts, which are of great importance in analytical chemistry. In recent times, the development of the chemistry of complexes and their use in analysis [3] has led to a continuous increase in the number of compounds known to form internal complex salts with metals.

It was shown in [1] that the Cu atom in copper acetylacetonate forms four covalent bonds directed toward the corners of a square, as in other internal copper complexes [4]. A knowledge of the structures of chromium and aluminum acetylacetonates[1] is important when comparing the structure of a molecule containing a metal atom which does not possess d-electrons, and, as a rule, is less frequently involved in complex formation (Al). This information will throw light on the question of the nature of the chemical bonding in complexes of different metals. The most detailed structural studies of internal complexes carried out to date have been those on copper and nickel salts [4-6]. There is no information available in the literature on the structure of aluminum internal complexes; as to chromium salts, there is only one report, on the structure of the trihydrate of potassium dioxalatodiaquo-chromiate [7].

We prepared crystals of Cr–AA in the form of plates and six-sided violet prisms, by crystallization from chloroform and acetone. Al–AA crystallized out of benzene in the same forms, but the crystals had a light yellow color.

Goniometer studies of crystals of the two compounds showed that they were similar; the interfacial angles for the plates were ~80 and ~100°, and for the prisms ~80, ~33, and ~67°. X-ray oscillation photographs showed that the crystals had primitive Bravais lattices and the following unit cell constants:

Al–AA: a 14.25 ± 0.05; b 7.68 ± 0.02;
c 16.17 ± 0.03 Å, β = 99°22'.
Cr–AA: a 13.80 ± 0.05; b 7.58 ± 0.02;
c 16.44 ± 0.03 Å, β = 99°30'.

The densities of Al–AA and Cr–AA crystals were found pycnometrically in an aqueous medium, these being 1.30 ± 0.03 and 1.39 ± 0.01 g/cm^3; the number of molecules in the unit cell was four. Hence, $\rho_{\text{x-ray}}$ = 1.27 and 1.37 g/cm^3, respectively. The systematic absences on x-ray goniometer photographs of zero- and first-layer lines about the b axis, and on zero-layer lines about the a axis, established that both compounds had the space group $C_{2h}^5 - P2_1/c$.

The similarity in external form of the crystals, the closeness of their unit cell constants, and the fact that both belong to the same space group, all undoubtedly show that Cr–AA and Al–AA are isomorphous. Isomorphism of complex chromium and aluminum compounds has also been established for Cr $(H_2O)_6Cl_3$ and Al $(H_2O)_6Cl_3$ [8], in which the metal atoms have six-fold coordination, as in both Cr–AA and Al–AA. However, these cases should not be taken as analogous, since the Cr and Al atoms in the acetylacetonates form valence bonds with oxygen atoms, while in the hydrates valence bonds are not formed.

The fact that crystals of Cr–AA and Al–AA are isomorphous is an indication that they have similar structures, belonging to the same structure type. Each contains three closed acetylacetone groups, arranged in three mutually perpendicu-

[1] These will be denoted by Cr–AA and Al–AA in the future.

TABLE 1. Coordinates of the Metal Atoms

Method	Al–AA		Cr–AA	
	x_{Al}	z_{Al}	x_{Cr}	z_{Cr}
"Difference" Patterson projection	x = 0.238		z = 0.232	
Fourier projection	–	–	0.232	0.220
Harker section	0.234	0.215	0.234	0.220
Fourier section for y = ¼	0.237	0.220	0.232	0.220

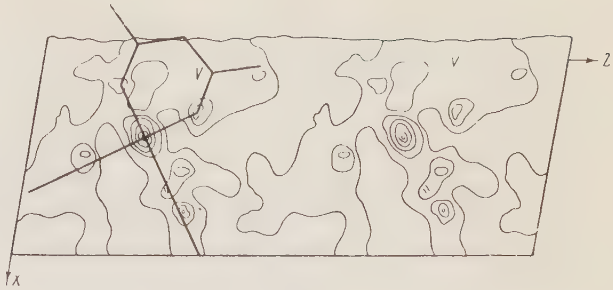

Fig. 1

lar planes, with the metal atom shared between them at the center. The O–Me–O angle is close to 90°. The oxygen atoms form a regular octahedron around the metal atom. Three of the edges of this octahedron are different from the rest, since they are formed by oxygen atoms from the same acetylacetone ring, while the other nine are made up of oxygen atoms belonging to different rings.

As a consequence of this, the symmetry of the octahedron is lowered to $L_3 3L_2$. Because the molecule has neither a center nor a plane of symmetry, molecular asymmetry arises, leading to formation of left- and right-handed octahedra. The compounds Cr–AA and Al–AA are not optically active because the crystals contain a center and a plane of symmetry, and there are equal numbers of the two enantiomorphic molecules in the unit cell. This picture of the structure of the molecule is confirmed by the positioning of the molecules in the space group, the n = 4 molecules are distributed in general four-fold positions.

To investigate the structures of the crystals in more detail, photographs of the zeroth, first, second, and third reciprocal lattice planes were obtained for rotation about [010], using a KFOR camera and CuK_α radiation. The reflection intensities were evaluated visually using a blackening chart. To bring all the intensities for a given crystal to the same scale, x-ray photographs were taken about [001] for Cr–AA and about [100] for Al–AA. The dead zone was partly filled by reflections obtained from the last x-ray photographs. This resulted in 488 reflections of type (hk$l$) for Cr–AA, and 379 reflections for Al–AA. Corrections were made for the kinematic and polarization factors.

The initial task was to determine the coordinates of the metal atoms. The Patterson projections constructed for Cr–AA and Al–AA did not correspond completely in their peak positions and heights, which made it impossible to fix definitely the metal atom coordinates. A "difference" projection showed up one peak, that with the greatest height. From this, the x and z coordinates of the metal atoms shown in the table were obtained. To find the y coordinates, linear Patterson–Harker sections P (0, y, ½) were calculated [9]; for both compounds, y had a value of approximately ¼.

The x and z coordinates of the metal atoms were refined by calculating the plane Patterson–Harker sections P(x, ½, z). These sections were, at the same time, a check on the value obtained for y, since, when y ≈ ¼, the difference in heights of the atoms Δy, is equal to ½, which must lead to the appearance of an extraneous peak on the section. This reasoning was fully confirmed; in the independent part of the section, two maxima appeared instead of one. One of these maxima corresponded to the difference Patterson maximum (see Table 1), while the other was shifted by ½c. However, if either of these, and also the two derived maxima, are given the coordinates 2x, 2z, then all the alternative cases are completely identical, and transform one into the other by choosing the origin of coordinates at one or another symmetry center of the space group.

After the coordinates of the metal atoms had been found, it was then possible to establish the structure amplitude signs, using the isomorphous replacement method [10]. We were able to find the signs for a considerable number of reflections. The only signs which were not known were those for reflections in which F(hk$l$) for Cr–AA and ≈F(hk$l$) for Al–AA, i.e., those in which the proportion of scattering due to the metal atom was close to zero. In the case of reflections of general types, because y_{Me} = ¼, there was a further limitation on the fixing of signs, since here the part of the structure amplitude due to the metal atom was reduced to zero when k = 1 or 3, and h + l = 2n, and when k = 2 and k + l = 2n + 1. For these cases, F(hk$l$) for Cr–AA should be equal to F(hk$l$) for Al–AA, but this was not always observed in practice. It appears that y_{Me} is not precisely equal to ¼, and also that the coordinates of the atoms in Cr–AA are not completely identical to those of the corresponding atoms in Al–AA.

To check the system of signs derived, and carry the structure determination a stage further,

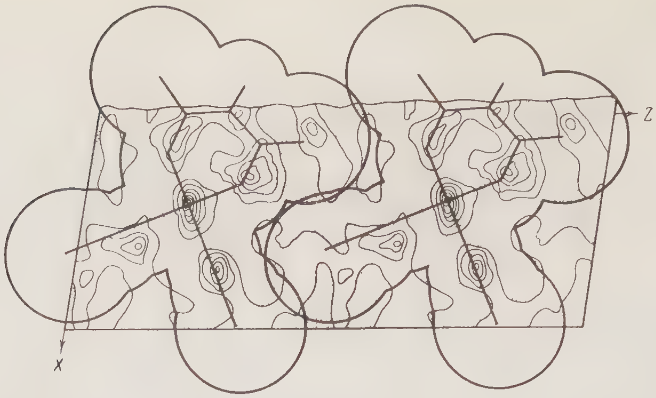

Fig. 2

an (h0l) Fourier projection was calculated (for Cr–AA). This projection clearly showed the peaks corresponding to the chromium atom; around this were four other maxima of lower height, at the corners of a square, these possibly being oxygen atoms, since they lay 1.9 A away from the Cr atom (Fig. 1). The square of O atoms present around the chromium atom can be interpreted using the molecular model, on the assumption that the "four-fold" pseudo-axis of the molecules (as we will call the direction which would be occupied by the four-fold axis in an octahedron of normal symmetry) is directed along the b axis of the crystal. Then the maxima which appear on the projection correspond to oxygen atoms lying in the same plane as the chromium atom. The region of higher density marked V apparently corresponds to the acetylacetone ring which also lies in the same plane. These results are further evidence that the signs we derived were correct.

It appeared that the atoms of this ring would be well resolved in a section parallel to the xz plane at $y = y_{Me}$. To calculate this section, it is necessary to know the signs of the structure amplitudes for hk$l$-type reflections. To determine those signs which were not found by the isomorphous replacement method, we tried the direct method [11]. For comparison we also included here reflections for which the signs were already known. These signs would need to be confirmed by the direct method. However, as well as the signs which agreed, there were also many which did not. Because of this, we did not consider that we could use signs obtained by the direct method in further calculations.

Using structure amplitudes for which signs had been found by the isomorphous replacement method (256 out of 488 for Cr–AA, 140 out of 379 for Al–AA), we calculated an electron density section for a plane lying parallel to xz and at a height of $y = \frac{1}{4}$. The distribution of electron density peaks on this section confirmed the results obtained from the projection, and allowed us to fix the orientation of the molecule more exactly. This orientation does not contradict the geometrical conditions for the arrangement of the molecules, as can be seen from Fig. 2.

It is possible that the results obtained are not particularly exact. It appears that the axis of the molecule is not precisely parallel to the b axis of the unit cell, and the shape of the molecule may differ somewhat from that of the regular octahedron which we assigned it as a first approximation. The structure can be refined after determining the signs of all the structure amplitudes through construction of three-dimensional syntheses.

Our investigations have shown that the molecules of chromium acetylacetonate and aluminum acetylacetonate have closely related structures, even though the electronic configurations of chromium and aluminum atoms are different.

The authors are deeply indebted to Professor G.S. Zhdanov for a number of valuable observations.

LITERATURE CITED

1. E.A. Shugam, "The structure of internal complex compounds," Dokl. Akad. Nauk SSSR, 81, 5, 853 (1951).
2. E.A. Shugam, "The crystal structure of copper acetylacetoetherate," Zh. Fiz. Khim., 28, 4, 643 (1954).
3. R. Prishibil, Complexes in Analytical Chemistry [Russian translation] (IL, 1955).
4. E.A. Shugam, "The crystal chemistry of some internal complex salts," Usp. Khim., 22, 5, 622 (1954).
5. R. Kruh and C.W. Dwiggins, "Coordination of copper (II) in copper 8-hydroxyquinolinate dihydrate," J. Am. Chem. Soc., 77, 806 (1955).

6. M. Stackelberg, "Röntgenographische Untersuchungen an inneren Kupfercomplexsalzen," Z. Anorg. Chem., 253, 136 (1947).
7. J.N. Niekerk and F.R. Schoening, "The crystal structure of trans-potassium dioxalatodiaquochromiate $K/Cr(C_2O_{4/2} \cdot H_2O)_2 \cdot 3H_2O$,"
8. K.R. Andress and C. Carpenter, "Die Struktur von Chromchlorid- und Aluminium chloridhexahydrat," Z. Kristallogr., A87, 446-463 (1934).
9. D. Harker, "The application of three-dimensional Patterson Method and the crystal structures of proustite Ag_3AsS_3 and pyrargirite Ag_3SbS_3," J. Chem. Phys., 4, 381 (1936).
10. J.M. Robertson and L. Todd, "X-ray studies in the caryophyllene series. The chloride and bromide from β-caryophyllene alcohol," J. Chem. Soc., April, 1254-1263 (1955).
11. G.S. Zhdanov and Z.V. Zvonkova, "The direct method of determining structure amplitude signs," Dokl. Akad. Nauk SSSR, 86, 3,529-532 (1952).

PHASE TRANSITIONS AND DOMAIN STRUCTURE IN BARIUM TITANATE AT 120 AND 5°C

I. S. Zheludev and V. F. Parvov

Institute of Crystallography, Academy of Sciences of the USSR
Translated from Kristallografiya, Vol. 1, No. 4,
pp. 482-483, July-August, 1956
Original article submitted May 19, 1956

Barium titanate, which has cubic symmetry at temperatures above 120°C (class 6/4), is known to undergo three phase transitions at lower temperatures [1]. Within the temperature range 120-5°C, $BaTiO_3$ has tetragonal symmetry (class 4 · m), between +5 and –70°C it has orthorhombic symmetry (class 2 · m), and, finally, below –70°C it belongs to the trigonal class 3 · m. In three of its modifications (not the cubic), $BaTiO_3$ has ferroelectric properties. As a rule, crystals of $BaTiO_3$ are synthesized in the cubic modification, and at the temperatures indicated they split up into separate spontaneous polarization regions or domains, in which the direction of spontaneous polarization coincides with the tetrad, diad, or triad axes, in the tetragonal, orthorhombic, or trigonal modifications, respectively.

Optical studies of the domain structure of $BaTiO_3$ were of obvious interest, to determine both the properties and the relative orientation of the domains. For this, we made 16-mm movie films of the transitions at 120 and 5°C, at a rate of 24 frames per second. The observations were made in polarized light with crossed Nicols. In the present article, we will describe the course of these transitions, without discussing them in detail.

Figure 1 shows individual frames of the transition from the cubic modification to the tetragonal

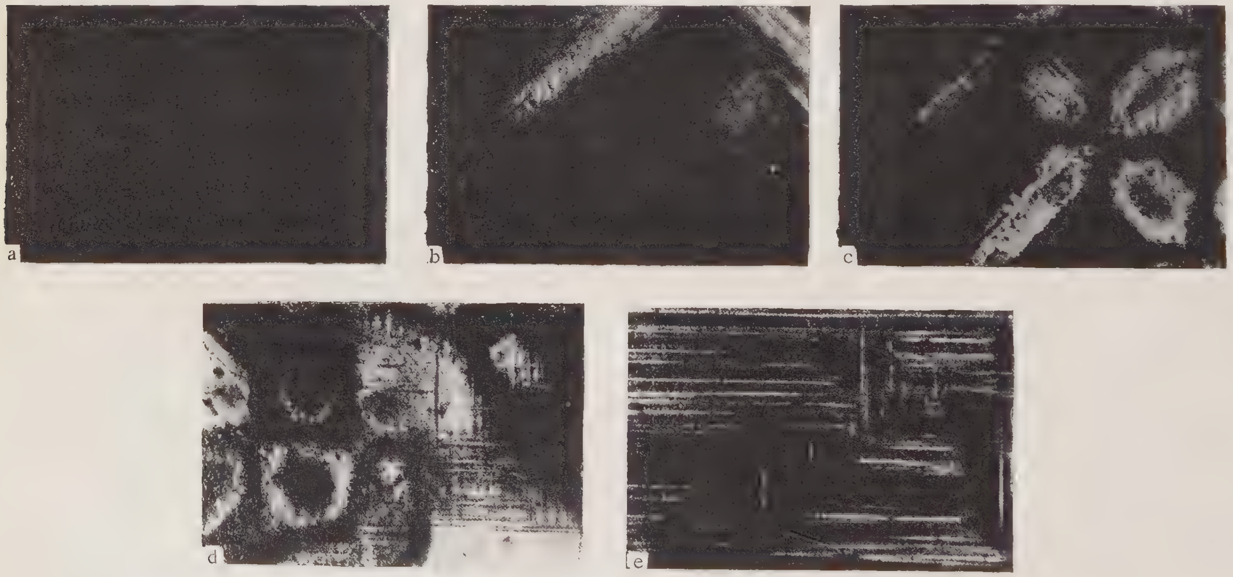

Fig. 1. Movie frames showing the transition of a $BaTiO_3$ single crystal from the cubic to the tetragonal modification at 120°C. x 60.

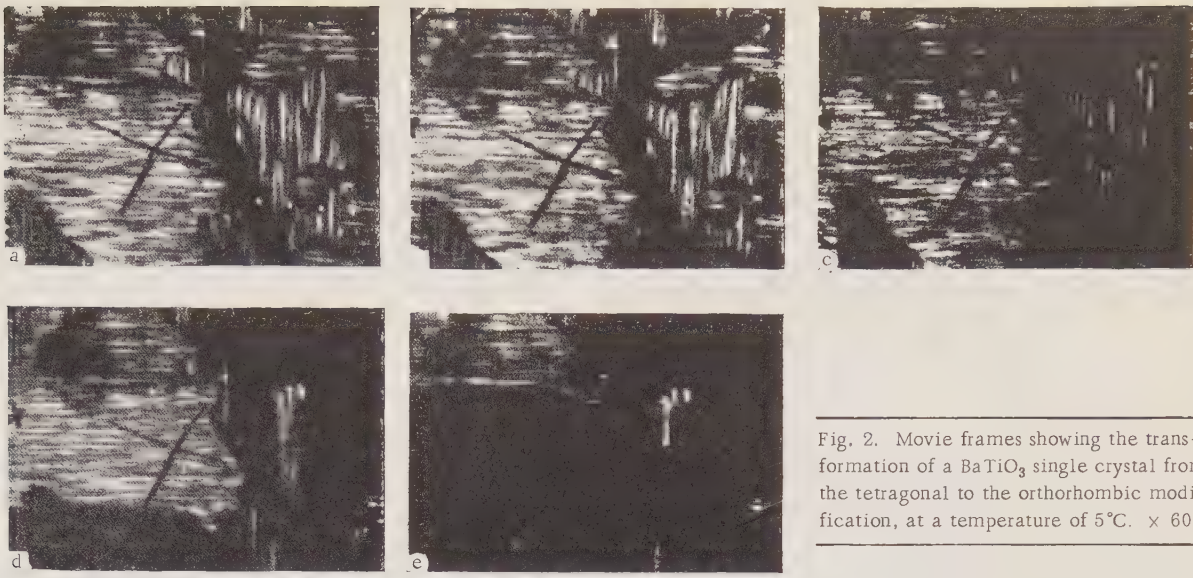

Fig. 2. Movie frames showing the transformation of a $BaTiO_3$ single crystal from the tetragonal to the orthorhombic modification, at a temperature of 5°C. × 60.

modification. (In the frames shown in Fig. 1 and Fig. 2, the planes of polarization of the Nicols were horizontal and vertical.) The complete transition occupied about 6-8 sec. Figure 1a shows the start of the change. The greater part of the crystal is cubic, and it is only in the upper right-hand part of the frame that the transition to the tetragonal modification has begun. The plane of the picture is the same as the (100) face of the cubic crystal, so that a line toward the upper right-hand part of the figure corresponds to the [011] direction in the crystal, and thus from Fig. 1a it can be seen that the optic axis of the tetragonal modification lies in the (100) plane, and the four-fold axis coincides in direction with the normal to the (001) or (010) face of the cubic crystal. In accord with the fact that the cubic crystal has two such equivalent directions in the (100) plane, Figs. 1b, 1c, and 1d show the formation of new tetragonal regions as the transition proceeds, with their four-fold axes lying along the directions (001) and (010). When two tetragonal domains with mutually perpendicular directions of spontaneous polarization meet, they form a boundary lying at 45° to these directions, i.e., along the [011] direction of the cubic crystal. The appearance of these boundaries between domains is particularly noticeable in Figs. 1b, 1c, and 1d. In the later stages of the transition, the whole crystal is broken up into domains, with the boundaries between these lying along the <011> directions (see Fig. 1e).

The movie films of the transition from the tetragonal to the orthorhombic form of the crystal are shown in Fig. 2 (in Fig. 2 the orientation of the crystal is the same as in Fig. 1). Figure 2a shows the domain structure of the tetragonal crystal in its original state, at a temperature above +5°C. At about +5°C, the phase transition begins. It is interesting to note that the transition is not completed simultaneously over the whole crystal, but in separate parts, which each undergo transition as a complete unit.

Figures 2b, 2c, 2d, and 2e show the gradual transformation of the crystal to the orthorhombic modification. From the figure, it can be seen that the boundaries of the individual orthorhombic regions (the dark spots in Fig. 2) lie along the <011> directions of the cubic crystal. If a crystal which has passed over into the orthorhombic modification is rotated between crossed Nicols, it is illuminated in positions where the <100> directions of the cubic crystal coincide with the direction of vibration in one of the Nicols, and the dark regions of the crystal are seen to split up into smaller regions, the domains, the boundaries between which coincide with the above directions. From this it follows that the directions of spontaneous polarization in the orthorhombic modification coincide with <110> directions in the cubic crystal.

The authors are grateful to Academician A.V. Shubnikov for discussing the results of the present investigation.

LITERATURE CITED

1. P. W. Forsbergh, "Domain structures and phase transitions in barium titanate," Phys. Rev., 76, 1187-1201 (1949).

NATURE OF THE COLOR CENTERS IN SMOKY QUARTZ

L. G. Chentsova

Institute of Crystallography, Academy of Sciences of the USSR
Translated from Kristallografiya, Vol. 1, No. 4,
pp. 484-485, July-August, 1956
Original article submitted April 10, 1956

The smoky color of quartz produced by hard radiation is associated with impurities [1,2]. In 1949, it was shown [3,4] at the Institute of Crystallography, that a layer resistant to radiation-induced coloration is produced at the anode when a current is passed through a plate cut perpendicular to the c axis at a high temperature. Some ions (Li, Na, K, Cu) can migrate along the structural channels in quartz [3-6], which indicated that the ions responsible for the color may lie in those channels and may be removed by the passage of the current. However, this fails to explain some of the observed effects, especially why the uncolored layer is not displaced in the reverse sense when the potential is reversed. It is also unclear why the injection of Li or Na ions into these channels does not alter the tendency to acquire the smoky color, while the injection of Fe, Mn, or Cu[1] will suppress that tendency.

Recent EPR studies on smoky quartz [7,8] have indicated the structure of these color centers, which has led to a reconsideration of views on ionic migration. The above effects can now be given a satisfactory explanation.

It has been shown [7] that aluminum may be the element responsible for the smoky color, and this was confirmed [8] by the synthesis of quartz in the presence of aluminum compounds. The Al^{3+} ions replace Si^{4+} in the silicon–oxygen tetrahedra [8], and the resulting charge defect is assumed to be compensated by alkali–metal or hydrogen ions. These centers are responsible for the localized levels that give color centers in response to radiation.

From this we may deduce that the channels contain the ions that balance the charge defect, not the aluminum ions. Electrolysis then displaces the compensating ions toward the cathode and the resultant excess of oxygen ions toward the anode. The purified layer then has an altered oxygen lattice, which is why the quartz is no longer colored by irradiation.

An alkali–metal salt as anode gradually causes the compensating ions to be replaced by alkali–metal ones; the lattice is not altered thereby; and the crystal may still become colored. Alkali ions injected into structurally altered quartz do not restore the sensitivity to radiation; the injected ions cannot be bound in the altered lattice and thereby produce defects that would give rise to color centers. This explains why the boundary of the anode layer does not shift when the current is reversed.

The ions of Mn, Fe, and Cu are less mobile than those of the alkali metals, which explains the formation of a radiation-resistant layer at the anode. The lattice has time to alter in the layer between the advancing ions and the compensating ions already present, so this layer remains resistant.

Evidence for the lattice alteration comes also from the change in plasticity; the quartz is incapable of twinning after electrolysis [10].

LITERATURE CITED

1. G.G. Lemmlein, Dissertation: Morphologic and Genetic Studies of Quartz [in Russian] (1952).
2. G.G. Lemmlein, "Coloration by irradiation in crystal quartz and glass made from it," Dokl. Akad. Nauk SSSR, 43, 247-249 (1944).
3. L.G. Chentsova and N.E. Vedeneeva, "The states of impurities injected into the lattice of smoky quartz," Dokl. Akad. Nauk SSSR, 48, 305-308 (1949).
4. L.G. Chentsova and N.E. Vedeneeva, "Relation of ionic conduction to coloration in smoky quartz," Tr. Inst. Kristallogr., 7, 191-202 (1952).

[1] Tests have been done on the injection of ions of Fe, Mn, and Cu by using Fe_2O_3, MnO_2, and CuO as anodes. Ionic migration can be detected from the passage of currents considerably in excess of those produced by a platinum anode with the same quartz specimen. In addition, metallic copper is deposited at the cathode when cupric oxide is used.

5. P. M. Harris and C. Waring, "Diffusion of lithium ions through quartz in an electric field," J. Phys. Chem., 41, 8, 1077-85 (1937).
6. J. Verhoogen, "Ionic diffusion and electrical conduction in quartz," Am. Mineral., 37, 637-655 (1952).
7. J. H. E. Griffiths, J. Owen, and I. M. Ward, "Paramagnetic resonance in neutron-irradiated diamond and smoky quartz," Nature, 6, 4401, 439-440 (1954).
8. M. C. M. O'Brien, "The structure of the color centers in smoky quartz," Proc. Roy. Soc., A 231, 404-414 (1955).
9. C. S. Brown, R. C. Kell, P. Middleton, and L. A. Thomas, "Influence of impurities on the growth of quartz crystals from flint and quartzite," Nature, 175, 4457, 602-603 (1955).
10. E. V. Tsinzerling, "Artificial stabilization of the lattice of quartz," Dokl. Akad. Nauk SSSR, 95, 529-530 (1954).

A FLAT-CRYSTAL MONOCHROMATOR FOR THE BSV-4 TUBE

S. S. Kvitka

M.V. Lomonosov State University, Moscow

Translated from Kristallografiya, Vol. 1, No. 4, pp. 485-487, July-August, 1956

Original article submitted September 5, 1955

A monochromator usually incorporates most of the possible ways of adjusting the crystal relative to the primary beam, which makes for complex construction; in addition, the gain in intensity resulting from exact adjustment does not balance the loss from the inevitable increase in the distances.

A bent-crystal monochromator usually gives a high intensity at the line focus, but it is quite unsuitable for use with the type of x-ray camera that is collimated to produce a narrow beam.

A flat-crystal monochromator has been developed in the Department of Solid State Physics for use with x-ray tubes of the BSV-4 type. This monochromator is simple and has no more adjustments than are really essential; it has a very much reduced distance between tube and crystal, and also between crystal and camera. Pentaerythritol has given the best results.

The exposure has been evaluated by using an RKD camera with a tube having a copper anode operated at 50 kV, 12 mA. A copper wire 0.3 mm in diameter was examined with the unfiltered radiation, with a 0.02-mm nickel filter inserted, and with the monochromator inserted. Patterns comparable in sharpness and density were obtained with exposure times of 12, 30, and 210 min; but the contrast obtained with the monochromator was far higher than that in the other two cases. The patterns with the filter and with the monochromator were also compared for quality by the use of a large number of minerals. The monochromator here required twice the exposure time of the filter, and the lines were even then somewhat weaker, but the number of lines observable was considerably greater than with the filter.

The base of the monochromator (Fig.1) is an iron ring A attached to the shield of the BSV-4. This ring can be used to define the beams emerging from the tube, since it has four holes to match those in the shield. Rectangular slides C tensioned by springs D work in horizontal slots in the ring and vertical slots in shield B. These slides are simply cut from standard printer's leads 0.75 mm, which are made from an alloy of lead with 14% antimony and a little tin. These are of adequate mechanical strength and good x-ray absorption. These slides provide any setting from completely open to completely closed, and hence a rectangular slot of any size within these limits. This provides substantial collimation of the primary beam and suppresses

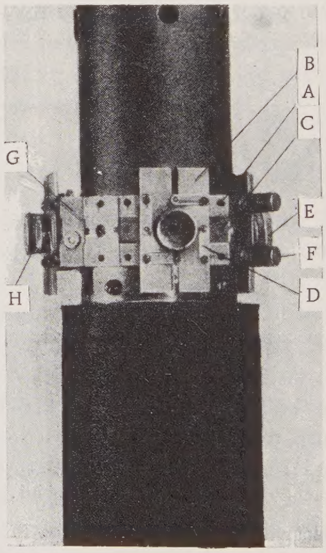

Fig. 1. The monochromator set up on a BSV-4 tube. The monochromator G is close to the left-hand window; the middle window is open. Slides C, tensioned by springs D, form a small rectangular slit. A) Iron ring; B) shield; E) cover; F) screw; H) rod.

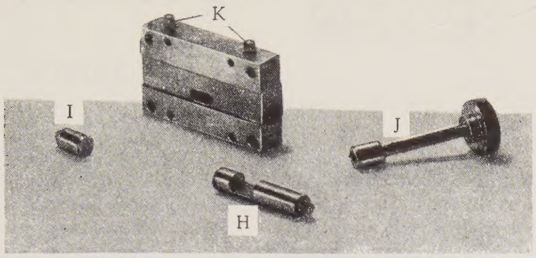

Fig. 2. The monochromator (exploded view) with the key J used to turn and clamp rod H and stop I. The rod has a slot, the crystal being cemented into this; K are screws holding rod and stop.

scattering at the outer parts of the camera. The window may also be closed by cover E containing a lead disc. Cameras working from adjacent windows are mutually screened by shields held by screws F.

The monochromator G can be set up on any of the four windows between ring A and one of the shields B; it consists of a rectangular block (Fig. 2) drilled with a horizontal hole and having a transverse oval window to pass the x rays. The hole carries rod H and stop I. The crystal is cemented into the slot in the rod by the use of celluloid dissolved in acetone; a thin film of the solution is also applied to the crystal to protect it from attack by atmospheric water vapor.

The rod and stop are inserted, which leaves two adjustments to be made: the crystal (rod) may be moved along, and the rod may be turned around its axis. One of the screws K clamps the rod, while the other clamps the stop, key J being used to rotate and clamp the rod. The reflecting plane is parallel to the face of the crystal, so these adjustments are sufficient to give a strong reflected beam, which is readily seen on the usual fluorescent screen in a slightly darkened room. The primary beam is defined by adjusting the slides when the crystal has been set up in this way; the exit slit for the reflected beam is also closed down as far as possible.